METALATION AND DEMETALATION OF HUMAN METALLOTHIONEIN STUDIED BY ION MOBILITY MASS SPECTROMETRY

A Dissertation

by

SHU-HUA CHEN

Submitted to the Office of Graduate and Professional Studies of
Texas A&M University
in partial fulfillment of the requirements for the degree of

DOCTOR OF PHILOSOPHY

Chair of Committee,	David H. Russell
Committee Members,	Tadhg P. Begley
	James C. Hu
	Emile A. Schweikert
Head of Department,	Francois P. Gabbai

May 2015

Major Subject: Chemistry

ABSTRACT

The mechanism of cadmium binding to intact human metallothionein-2A (MT) is investigated. We describe two complementary mass spectrometry (MS) strategies to study the metalation/demetalation mechanism: (i) chemical labeling combined with proteomics-based top-down or bottom-up approaches (ii) ion mobility-mass spectrometry (IM-MS). We presented here for the first time for direct identification of metal-binding sites on a partially-metalated intermediates by combing chemical modifications (N-ethylmaleimide (NEM)) and 2D MS-CID-IM-MS. These results provide conclusive evidence of specific binding of Cd^{2+} to the α-domain and demetalation is the reverse order of metalation. Molecular-specific profiles for metal affinity and kinetic stability for each metalated intermediate provided by MS reveal that the reactivity of various Cd_iMT species is dependent on their metalation state and reaction is cooperative for both domains. These data suggest that the α-domain has greater thermodynamic/kinetic stability than does the β-domain. In addition, the alkylation on kinetically labile cysteins reveals that the α domain contains a weakly coordinated site at Cys33, which is located at the extreme N terminus of the α domain and might be related to the intra-domain cooperativity.

Further, IM-MS and molecular dynamics (MD) simulations are used to follow metal-induced conformational changes, which reveal new insights into the mechanism for metalation of MT. IM data for the Cd_iMT ($i = 0 - 7$) ions reveal a diverse population of ion conformations. Upon metal-ion binding, the conformational diversity for apoMT

and partially-metalated ions converges toward ordered, compact conformations as the number of bound Cd^{2+} ions increase. We interpret this data as evidence of metal-dependent folding and increasing numbers of metal ions yield more compact ion structures. MD simulations provide additional information on conformation candidates of Cd_iMT ($i = 0 - 7$) that supports the convergence of distinct conformational populations upon metal binding. Integrating the IM-MS and MD data provides a global view that shows stepwise conformational transition of an ensemble as a function of metal ion bound. Furthermore, collisional activation was used to increase effective ion temperature (T_{eff}) prior to entering and within the ion mobility analyzer, providing new insights about protein folding energy landscape.

ACKNOWLEDGEMENTS

Fist I would like to thank my advisor Dr. David H. Russell for his consistent support and guidance throughout the course of my Ph.D. His in-depth knowledge and critical thinking has been extremely beneficial for me. His scientific attitude and enthusiasm has also made a great impact on me. I especially appreciate the training in independent thinking and problem solving which helped me develop my research capabilities.

I would also like to thank my committee members, Dr. Tadhg P. Begley, Dr. Emile A. Schweikert, and Dr. James C. Hu, for their valuable input throughout the course of this research. I am also very grateful of the assistance provided by Dr. Lisa M. Pérez in molecular modeling works.

I would like to thank all members of the Russell research group for their help. A special thanks to Dr. William K. Russell for his assistance and guidance for my research projects. I am also very grateful to Dr. Liuxi Chen for being a good friend and colleague who provided encouragement, ideas and help on my research and PhD life.

I would like to thank my master's thesis advisor, Dr. Yu-Ju Chen, for getting my graduate career started on the right foot and encouraging me to pursue an advanced education. I am also very grateful to my former research supervisor Dr. David R. Goodlett for his support and the opportunity to gain a wider breadth of experience.

I would like to thank my family for all their love, understanding and encouragement. I thank my mon for her encourage and faith in me. Thanks to my sister

and brother for taking care of our family in Taiwan. Thanks to my friends, especially Pei-Shan Chen, Shannon Tsai, Payluen Lee and Payshan Lee, for listening, well-wishes/prayers and advice which has been a great support for me in the past years. I would like to thank Amau and Kissme for always being by my side. Lastly and most importantly, I thank my husband and best friend Hsueh-Ying Chen for his infinite love, consistent encouragement and tolerance of my changing moods (you are the best!).

NOMENCLATURE

DTT	Dithiothreitol
EDTA	Ethylenediaminetetraacetic acid
ESI	Electrospray ionization
FRET	Fluorescence resonance energy transfer
HDX	Hydrogen-deuterium exchange
IM	Ion mobility
MD	Molecular dynamics
MS	Mass spectrometry
MT	Metallothionein
NEM	N-ethylmaleimide
SAXS	Small-angle X-ray scattering
TCEP	Tris(2-carboxyethyl)phosphine
T_{eff}	Effective ion temperature
TW	Traveling wave

TABLE OF CONTENTS

LIST OF FIGURES

Page

Page

LIST OF TABLES

CHAPTER I

INTRODUCTION

Metal ions play important roles in many chemical and biochemical processes, such as oxidation, oxygen transport, and electron transfer; almost half of the known enzymes require a specific metal to function. Metallothioneins (MTs) represent a family of cysteine-rich, small (~ 6 – 7 kDa) proteins.[1] MTs have been isolated from a wide range of living systems, including bacteria to human, suggesting that they play essential roles in biological systems. Homo sapiens contains at least 17 different MT isoforms.[2-3] Based on their sequence similarities and phylogenetic relationships, they are divided into 4 classes. MT-1 and MT-2 isoforms widely expressed in most organs. MT-3 is found predominately in brain and MT-4 is only detected in differentiating stratified squamous epithelia and the maternal deciduum.[2,4] One of the most studied isoform, human MT-2A is a monomeric protein composed of 61 amino acid residues of which twenty are cysteines (**Figure 1.1**). The cysteines coordinate to a wide variety of metal ions, including essential metal ions such as Cu^{+} and Zn^{2+} and nonessential metal ions such as Cd^{2+} and Hg^{2+}. Seven divalent or twelve monovalent metal ions are bound by the thiolates of MT with metal affinity in this order: $Hg^{2+} > Cu^{+} > Cd^{2+} > Zn^{2+}$, consistent with their Hard and Soft Acids and Bases (HSAB) properties. Although MT-metal ions complexes are thermodynamically stable, the metal-thiolate bonds are kinetically very labile, undergoing both bond breaking and reforming very rapidly.

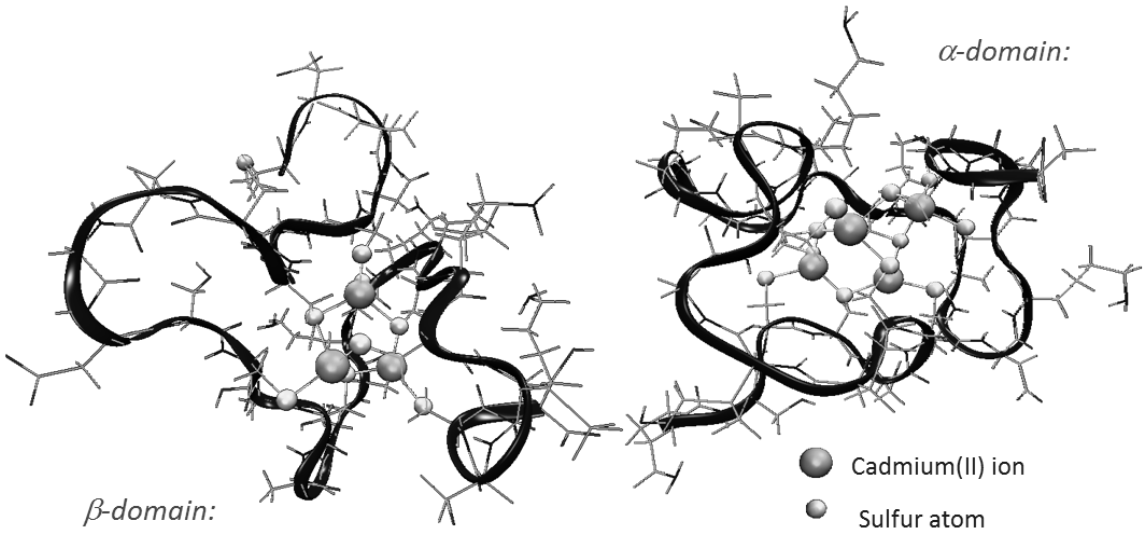

Figure 1.1. NMR structure of cadmium human metallothionein-2A. Human metallothionein is constitute of 61 amino acids: MDPNCSCAAG DSCTCAGSCK CKECKCTSCK KSCCSCCPVG CAKCAQGCIC KGASDKCSCC A. The NMR studies revealed a two-domain structure with no preferential orientation between the two domains.

Since their discovery in 1957,[1] their biological roles/functions have been a perplexing topic. The prevailing view is that MT is involved in detoxification of non-essential metal ions, regulation of essential metal ions, protection from oxidative stress and apoptosis, and control of cellular redox status, processing considerable impact on human health.[1,5-9] A number of studies have related deficiencies in MT to metabolic disorders such as Wilson's disease and Menkes disease.[10] MTs are also biologically linked to oxidative stress, apoptosis, and control of cellular redox status,[4,11-13] including formation of reactive oxygen species (ROS), which are implicated in the aggregation of amyloids,[14-16] and Vasak *et al*. suggested that exchange of metal ions between MT and aggregated amyloid-β reduces ROS production and Aβ toxicity.[14-15,17] A growing body

of evidence implicates metal ions and MTs in neurodegenerative diseases, including Alzheimer's, Parkinson's, amyotrophic lateral sclerosis (ALS).[12,18-20] MT level has been shown to increase in many tumors, thus it has been suggested that MT levels may serve as useful diagnostics for cancer.[21-22] In fact, MTs have been found substantially unsaturated with metal ions in many tumors.[23] More recently evidence has been presented that shows the existence of metal-unsaturated MTs under physiological cellular conditions. These studies suggest that metal-unsaturated MTs are biologically significant which actively participate both in cellular metal metabolism and redox balance; however, it is unclear whether this is truly apoMT or partially-metalated species.[24-27] Although the underlying mechanism(s) for biochemical processes involving MTs are not fully resolved, new insights are beginning to emerge. For example, Petering *et al.* and Andrews have shown that MTs are reactive toward various oxidants, electrophiles and alkylating agents, which potentially diminish deleterious effects of these toxic species.[12,28] Kelly *et al.* suggested that MTs confer resistance toward anticancer therapeutics by alkylation of cysteine residues[29] and Naganuma *et al.* showed that overexpression of MTs in cancer cells attenuates toxicity of antitumor therapeutics and provides intracellular drug sequestration, protecting host tissues from the toxic side effects.[30]

A variety of approaches have been employed to elucidate the metal-binding behavior of MT including optical absorption, emission, circular dichroism (CD), and nuclear magnetic resonance (NMR) spectroscopies and molecular modeling. Changes in the UV-VIS and CD spectra can be related to the identity of the bound metal and the

amount of metal loading.[5,31-33] However, the signals from such experiments represent the population-averaged response for all species present in the solution and do not distinguish signals from individual species. NMR and X-ray diffraction studies on mammalian MTs revealed a conserved dumbbell-shaped molecule with two distinct metal-centered clusters: a β-domain $(Metal)_3(Cys)_9$ in the N-terminus and a α-domain $(Metal)_4(Cys)_{11}$ in the C-terminus (see **Figure 1.1**).[34-37] Despite the essential atomic level structural information for fully metalated MTs provided by such techniques, the metalation/demetalation mechanisms remain largely unknown and the structures and binding sites for the partially-metalated intermediates are still unclear.

Recent advances in MS have greatly expanded our capabilities for characterization of intact proteins, protein-metal ion complexes and even protein complexes.[38-45] Particularly noteworthy is that ESI is a soft ionization method that preserves the non-covalent interactions thereby providing a direct measure of molecular distribution of various species present in the solution.[46-51] These MS approaches that afford capabilities to reflect "native" or "native-like" structures has now coined a new field termed "native mass spectrometry".[52] In addition to the high resolution and accurate mass measurement of analyte(s) by MS, tandem mass spectrometry (MS/MS) can be used to elucidate the number and sites of modifications. By combining proteomic strategies such as hydrogen/deuterium exchange (HDX),[53] chemical cross-linking, and chemical derivatization now MS has evolved as a powerful technology in structural biology that provides information about protein structure, dynamics, composition, and

subunit topology and stoichiometry and is complementary to established methods such as nuclear magnetic resonance and X-ray crystallography.

Ion mobility (IM) spectrometry, a gas phase separation of molecules based on their differential mobility through a buffer gas, has long been utilized for many analytical applications, such as detecting volatile compounds and chemical warfare agents.[54] When coupled with MS, this integrated technique is used to ascertain complementary information about the analytes. Furthermore, IM adds an additional dimension of separation to MS that provides enhanced analytical peak capacity, which is particularly useful for MS-based "-omics" approaches. In fact, IM separates ions in milliseconds time scale, which is much faster than most separation techniques.

More recently, the combination of "native-ESI" with IM-MS has rapidly evolved as a stand-alone technique for structural studies that interrogate conformation population for individual analyte,[55] such as elucidation of protein conformations,[56] construction of structural models of protein complexes,[57] and even characterization of IDPs.[58-65] Particularly, ion-neutral collision cross section (CCS) provided by IM-MS reflects physical shape and size of the ion.[55] With further combination with molecular dynamics (MD) simulation, this integrated methodology provides candidate structures for the ions sampled by IM-MS; for example, the CCS of these analytes can be correlated to 3-D shapes and conformations generated by molecular dynamics simulations.[45,66-67] IM-MS has now evolved as a de novo approach to obtain structural information, which is extremely valuable for systems that are not assessable by any other traditional methods.

Herein we utilized native IM-MS to characterize the metal-binding properties of MTs. The major focus of our study deals with fundamental chemistry, i.e., how does metal binding affect the chemistry of proteins, specifically we developed the mechanism from the stabilities/reactivities and conformations of the reaction intermediates (partially metalated species) in metalation/demetalation reactions. Although MTs have been widely studied, especially regarding their roles in metal homeostasis, protection against cadmium toxicity and neurodegenerative diseases; however, underlying mechanisms regarding details of metal-binding intermediates, mechanism of metal accumulation, and the role of metal ion in promoting protein conformational changes remain poorly understood and a method to directly probe the detailed mechanism was not developed. Our studies aim to develop a better understanding of structure-function relationships of this biologically important protein.

In Chapter II, we first demonstrated the utility of native MS in studying metal binding properties of MT. Several studies describing metalation/demetalation have been reported; however, the chemistry of intermediate species and site-specific metalation/demetalation are still not fully understood, specifically questions regarding (i) cooperativity of metal ion binding, (ii) metal ion-depend binding properties, and (iii) whether there are preferential binding sites remain hot topics of debate. The major complicating factors for studies on metalation/demetalation mechanisms of MT are the large number of metal binding intermediates (partially-metalated forms) and the rapid rates associated with these processes. Thus, it has not been possible to isolate individual components from this complex mixture for structural and mechanistic characterization.

MS provides molecular-specific information thus allowing a direct monitor of all species without the need of separation, which is ideal for MT systems. In this chapter, we showed how MS is used to measure the molecular distribution of starting state, intermediates and end-products in metalation/demetalation reactions and to derive the metal binding mechanism based on the reactivities of these intermediates. The model protein and metal ion chosen for our method development are human MT-2A and cadmium ion as the Cd-MT is one of the very few complexes that have been structurally resolved by NMR or X-ray crystallography.[37] In addition, Cd^{2+} is associated with cancer in many human organs, especially lung, kidney, and breast cancers.[68-69] In fact, recent evidence suggests that cadmium causes DNA damage and inactivates DNA repair system, potentially leading to cancers or neurodegenerative diseases.[69-71] It has also been proposed that cadmium causes the inactivation of a large number of metalloenzymes.[72] MTs play a major protective role through the uptake of free Cd^{2+} and thereby decreasing its adverse effects. The understanding of how MT is involved in cadmium detoxification function is of fundamental importance and have the potential for providing a more complete picture of cadmium carcinogenesis as well as developing new therapeutic strategies.

We developed a methodology that combines chemical labeling and top-down MS/MS approach (named MS-CID-IM-MS) to identify whether there are preferential metal-ion binding sites. That is, the metal-ion binding intermediate (partially-metalated forms) are chemically derived, m/z-selected and fragmented by a MS spectrometer. We studied the reaction intermediates that are derived from either metalation or demetalation

reactions. The schematic representation of the analysis procedure is illustrated in **Figure 1.2**. This direct analysis approach identifies the metal binding sites without the need of sample purification, which avoids any ambiguity that may arise from long sample handling procedures from bottom-up approaches. Specifically, this study shows a new strategy to study metal-ion binding sites of a partially-metalated intermediate and provides new insights related to metal binding mechanism of MT.

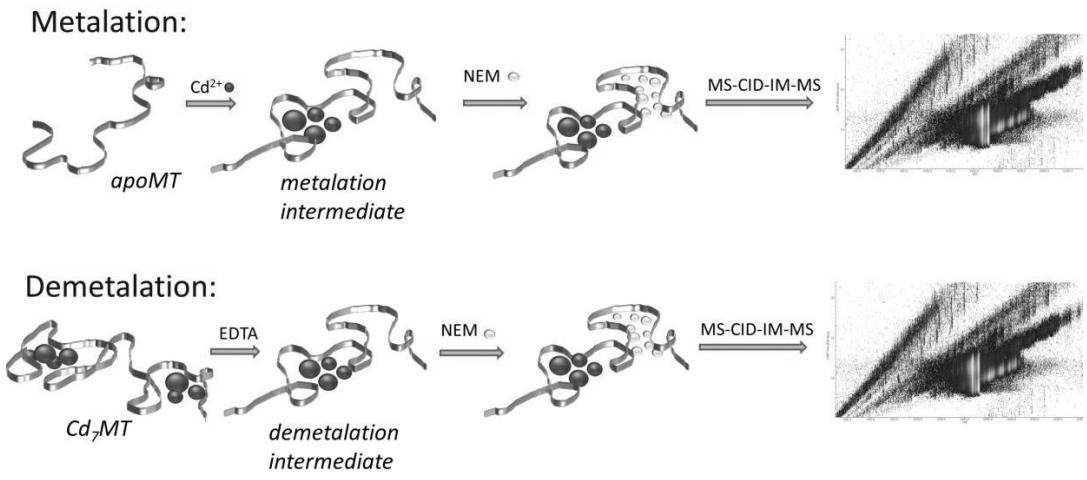

Figure 1.2 Schematic flow diagram of MS-CID-IM-MS approach for studying metal-ion binding sites in partially-metalated MT.

In Chapter III, ESI-MS is used to monitor metal displacement reaction of MT by N-ethylmaleimide (NEM). This competition between NEM and Cd^{2+} provides information on the relative stability among the 20 metalation sites; that is, NEM is expected to efficiently displace weakly bound Cd^{2+} ions, but more strongly bound or protected metal ions would be displaced more slowly, if at all. This study provides

insights into the kinetic stability of the metal ion binding sites. In addition, IM-CID-IM-MS is employed on a stable partially-alkylated metal-retaining intermediate, revealing a weakly binding site in the α domain. Finally, IM-MS is used to monitor the conformation of MT through the metal displacement reaction, providing insights into the effects of covalent labeling of free cysteines on its protein conformation.

In Chapter IV, we employed IM-MS to interrogate conformer population for each metalated form of human MT-2A. Specifically, this study provides new insights related to the metalation mechanism and conformational changes that occur upon metal binding. Since the structure for human fully-metalated Cd_7MT-2A was resolved by NMR in 1990, further structural studies for apo- and partially-metalated MTs have encountered a bottleneck as these metal-unsaturated species are not amenable to structure elucidation using NMR spectroscopy, X-ray crystallography, and optical methods such as UV/Vis, fluorescence, and circular dichroism. IM-MS provides an unparalleled approach to tackle this problem owing to its capabilities of monitoring all distinct metalated states by their characteristic m/z ratios by mass spectrometry and interrogating conformer conformation for individual metalation state by ion mobility spectrometry. In addition, molecular dynamic (MD) simulations were performed to explore candidate conformations that correspond to experimental CCS obtained by IM-MS. By integrating IM-MS and MD data we are able to construct a metalation pathway that shows conformational transition as a function of metal ion bound.

In Chapter V, we provided a comprehensive investigation of the ion's effective temperature (T_{eff}) that is manipulated by an IM-MS spectrometer. This study focuses on

the effects of changes in ion temperature for two structurally diverse proteins, an intrinsically disordered protein (apoMT) and a well-structured model protein (ubiquitin). Comparisons of experimental CCSs acquired at low T_{eff} and theoretical CCSs generated by MD simulation for solution-phase structures provide new insights about conformational preferences and retention of solution conformations. In addition, IM-MS data for ions that are collisionally activated provides information about folding and unfolding landscape (**see Figure 1.3**). To date, very little is known about the effects of metalation on folding/unfolding landscape of metalloproteins. By combining the MD simulations as a function of temperature, the change of CCS provides insights into the unfolding pathways.

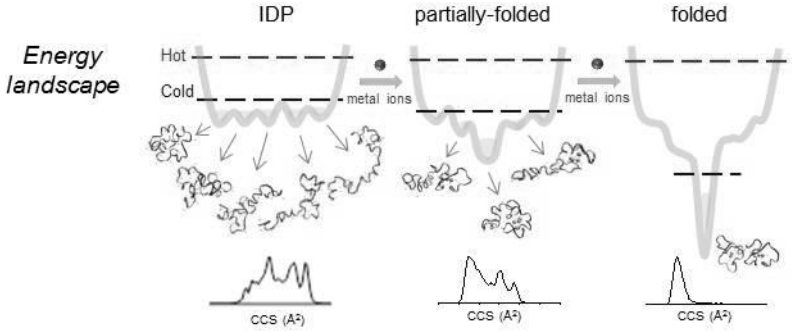

Figure 1.3 Probing protein folding landscape of an IDP (MT) by IM-MS.

CHAPTER II

COMBINING CHEMICAL LABELING, BOTTOM-UP AND TOP-DOWN ION-MOBILITY MASS SPECTROMETRY TO IDENTIFY METAL-BINDING SITES OF PARTIALLY METALATED METALLOTHIONEIN*

Introduction

Metallothioneins (MTs) represent a family of cysteine-rich, small (~ 6 – 7 kDa) proteins that have been linked to metal homeostasis, including detoxification of non-essential metal ions and regulation of essential metal ions.[1,5-7,9] MTs have been isolated from a wide range of living systems, including bacteria to human, suggesting that they play essential roles in biological systems. Despite intense research since the discovery of MT in 1957,[1] their precise physiological functions have not been fully identified and the metalation/demetalation mechanisms remain unclear.

Metal ion binding by MT has been extensively investigated using a large number of techniques.[6,73-78] UV-VIS and CD spectroscopies have been used to determine the identity of the bound metal and the amount of metal loading,[5,33,73,79] and the kinetics of demetalation of Cd_7MT has been studied using metal chelators such as EDTA[80-81] or electrophiles such as N-ethylmalimide (NEM).[82] X-ray diffraction and NMR provide atomic level structural information about fully metalated MTs, and these data

---

*Reprinted with permission from Chen, S.-H.; Russell, W. K.; and Russell, D. H. Combining Chemical Labeling, Bottom-Up and Top-Down Ion-Mobility Mass Spectrometry To Identify Metal-Binding Sites of Partially Metalated Metallothionein *Anal. Chem.* **2013**, *85*, 3229 – 3237. Copyright (2013) by American Chemical Society

provide evidence for a conserved dumbbell-shaped molecule that has two distinct metal-centered clusters, *i.e.*, a $Cd_3(Cys)_9$ cluster involving the N-terminus (denoted as the β-domain), and a $Cd_4(Cys)_{11}$ cluster (α-domain) involving the C-terminus.[34-37] It is important to note, however, that UV-VIS, CD, and NMR spectroscopies report the population-averaged response for all species present in the solution as opposed to responses that can be attributed to individual species, thus it is not possible to distinguish information related to the intermediate species from that of the final products of the reaction. Likewise, it is not always possible to accurately resolve structural features of partially metalated species from XRD data. Consequently, mechanistic details of metalation/demetalation remain largely unknown, as do the structures and binding sites for the partially-metalated or supermetalated forms.[83]

Studies of metal ion-MT interactions are further complicated by the large metal ion-binding affinities of the thiolate ligands and the rapid rates of metal accumulation. Although a number of partially-metalated MTs have been observed,[47,84] it has not been possible to isolate partially-metalated and metal saturated MTs from a complex mixture of MTs. Apparent binding constants of Cd^{2+} and Zn^{2+} to MT have been reported,[85-87] however, comparable information for the partially-metalated intermediates and mechanism(s) of metal accumulation have not been resolved owing to a paucity of characterization techniques. On the other hand, MS-based detection can unambiguously differentiate signals based on the characteristic *m/z* for individual metalated species, and mass analysis provides direct analysis of individual partially-metalated intermediates and

end-products of reactions, including metal uptake, metal exchange, or metal release and transfer reactions.[9,88-90]

Fenselau *et al*. first demonstrated the application of MS for studies of MTs, specifically identification of drug-reactive sites of MTs, metal ion complexation by MT, and metal ion transfer from Zn_7MT to EDTA and metalloproteins.[46-47,91-95] Recent advances in MS have greatly expanded the capabilities for characterization of intact proteins and protein-metal ion complexes.[40,96] For example, Lobinski *et al.* combined a variety of MS approaches to characterize the MT isoforms from a biological cytosol/tissue.[97-98] Particularly noteworthy is that ESI is a soft ionization method that preserves the non-covalent interactions thereby providing a direct measure of molecular distribution of various species present in the solution.[46-51] Consequently, such measurements allow for real-time analysis of reaction products without the need for isolation/purification of intermediates. Blindauer *et al.* have used ESI-MS to characterize a kinetically inert metal binding site in bacterial MT SmtA,[99] and Stillman *et al*. have used similar methodologies to study the binding kinetics of As^{3+} to intact MT-1 as well as individual MT-1 domains.[48-49] More recently, Stillman *et al*. examined MT-1 folding/unfolding accompanying metalation/demetalation processes based on changes in the charge-state distribution.[100-101]

The perception of similar metal ion-MT binding for metals of the same family has resulted in Cd-MT being used as a model for Zn-MT; however, differences in ionic radii, HSAB (hard-soft acid-base) properties,[102] and preferred coordination geometries between Cd^{2+} and Zn^{2+} may strongly influence the metal binding affinity and metal-

induced folding of the protein.[9,103-104] Although both fully-metalated human Cd_7MT-2A and Zn_7MT-2A adopt dumbbell-shaped structures,[105] it should be noted that Zn-MT and Cd-MT show distinct metal binding affinities (K_{app} (Cd-MT) ~ 10^{16} M^{-1} and K_{app} (Zn-MT) ~ 10^{12} M^{-1}) and the detailed metal binding pathways remain unclear. Here, ESI-IM-MS is used to monitor metalation reactions and to measure the abundance of the apo-protein, partially-metalated intermediates and end products, which provides information on the relative reactivities of the intermediates as well as the mechanism of metalation. We report the first use of ESI-MS for resolving the relative metal affinities of individual partially-metalated MT intermediates. The distinct binding features between Zn-MT and Cd-MT and the appearance of preferentially-formed intermediates have motivated us to develop a methodology to directly probe metal-binding sites in the partially-metalated intermediate. Our results show how combining chemical labeling with both top-down and bottom-up proteomic strategies provides direct, site-specific information of metalation of the partially metalated intermediates.

Experimental

Materials

Recombinant human metal-free MT-2A (apoMT) and cadmium-saturated MT-2A (Cd_7MT) were obtained from Bestenbalt LLC (Tallinn, Estonia). Cadmium acetate, ethylenediaminetetraacetic acid (EDTA) disodium salt dihydrate**,** N-ethylmaleimide (NEM), dithiothreitol (DTT), and ammonium acetate were purchased from Sigma-Aldrich (St. Louis, MO). Sequencing grade modified trypsin was from Promega

(Madison, WI). Deionized water (18.2 MΩ) was obtained from a Milli-Q water apparatus (Millipore, Billerica, MA).

Sample preparation

All apoMT and Cd_7MT powder samples were reconstituted in 50 mM ammonium acetate (pH 7.4) in a glove box, aliquoted into 10-μL portions, frozen in liquid nitrogen and lyophilized. The small portion powder samples were then saturated with nitrogen gas and sealed in a glove box so that the proteins were stored within an inert environment. The MT samples were stored under nitrogen in -80°C until use. The impurities and salts in each aliquot were removed by 6K MWCO spin column (Bio-Rad, Hercules, CA), and the sample was then reconstituted by 50 mM ammonium acetate (pH 7.4) containing 10% methanol and 5 mM DTT before the ESI experiments. The addition of 10% methanol in ESI enhances signal-to-noise ratio without affecting complexation of metal ion-MTs.[106-107] Representative mass spectra for apoMT and Cd_7MT are shown in **Figure 2.1**. The concentration of apoMT was estimated by Cd^{2+} titration experiments. Owing to the large Cd^{2+} affinity of MT (10^{16} M^{-1}), we can assume that the free Cd^{2+} is negligible compared to the concentration of Cd^{2+} associated with MT. Addition of 50 μM Cd^{2+} to the apoMT solution yields Cd_7MT, with respect to a concentration of ~ 7 μM for the apoMT solution.

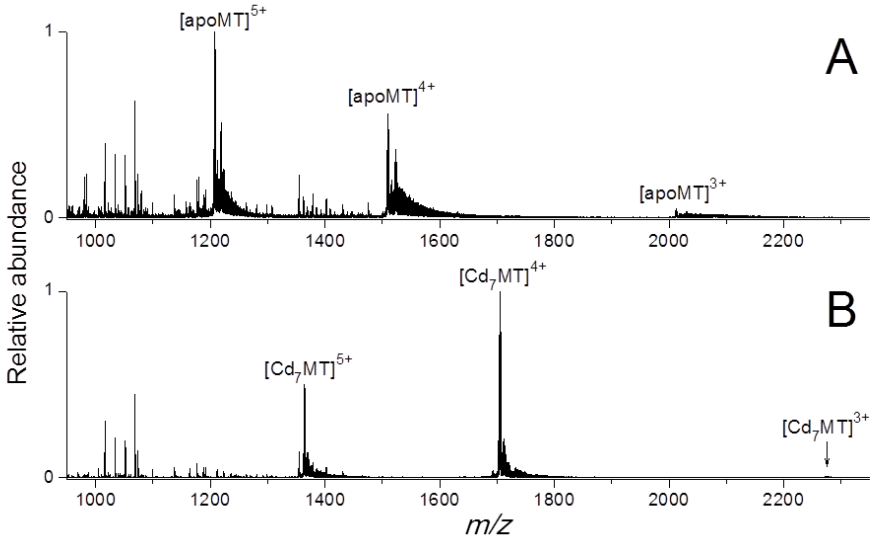

Figure 2.1. ESI-MS spectra of 7 μM solutions of (A) apoMT and (B) Cd_7MT. Significant amount of signals from impurities and/or degradation products were observed in low mass range (*m/z* < 1200) from the commercial MT samples. A typical titration experiment was performed after removing the low molecular weight species by a 6K MWCO spin column.

Oxidation of apoMT

Cysteine thiols are very prone to oxidation under aerobic conditions,[33] including formation of disulfide bonds and sulfenic, sulfinic and sulfonic acids. These modifications could potentially alter protein 3D structure as well as metal-binding affinity. Under our experimental conditions, only disulfide bond modification was observed. Therefore, a thiol reductant DTT was added to all solutions of apoMT to maintain the cysteinyl thiols in the active reduced states. **Figure 2.2** illustrates the effect of DTT in preventing apoMT from oxidation. Protein oxidation can also take place during ESI,[108-109] and to minimize this ESI was performed using the lowest possible

capillary voltages (see **Figure 2.2**). The mass accuracy (< 20 ppm) and resolution (FWHM: 18000) of these measurements were sufficient to identify the oxidation state of apoMT without ambiguity (see **Figure 2.2**).

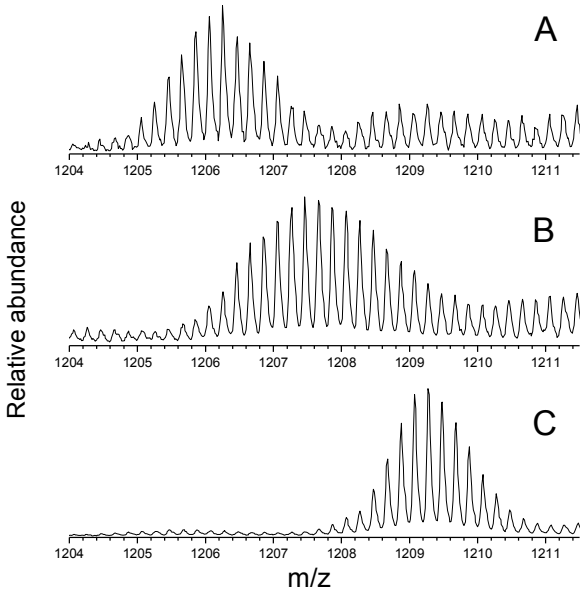

Figure 2.2. ESI-MS spectra of a 7 µM apoMT solution in 50 mM ammonium acetate with 10% MeOH (pH 7.4) acquired (A) in the absence of DTT at a 1.40 kV capillary voltage. The signal for $apoMT^{5+}$ were centered at m/z 1206.2 indicating a shift of 16 Da from the theoretical molecular weight (6042.2 Da) and formation of disulfide bonds; (B) In the presence of 5 mM DTT at capillary voltage 1.60 kV. The data shows a broader isotopic pattern centered around 1207.4 Da, suggesting loss of ~ 10 hydrogens and yielding a mixture of apoMT forms with different extent of oxidation. (C) In the presence of 5 mM DTT at capillary voltage of 1.40 kV. The data showed m/z for $apoMT^{5+}$ is 1209.2, consistent to the theoretical mass of apoMT with twenty free cysteinyl thiols. The data showed operating a gentle ESI condition by lowering capillary voltage to the onset of electrospray (1.40 kV in this case); ESI-induced oxidation was significantly eliminated. The results showed the oxidation can be detected by MS and reduced by the presence of DTT and using a lowest capillary voltage.

Metalation of apoMT and demetalation of Cd_7MT

The metalation experiment was performed by sequential addition of 1, 2, 3 4, 5, 6, and 7 μL of 1 mM of Cd^{2+} (or Zn^{2+}) to 100 μL of a 7 μM apoMT solution. Following each addition of Cd^{2+}, the protein was allowed to react with the metal ion for 1 hr under ambient conditions before MS measurement. Demetalation reactions were performed by adding 7 μL of 1 mM EDTA or by adding 1.4, 5, 10, 20 μL of 10 mM EDTA to 100 μL of a 7 μM Cd_7MT solution. The solution was incubated for 1 hr at room temperature and then analyzed by ESI-MS.

Identification of metal-binding sites in Cd_4MT partially-metalated intermediates

The Cd_4MT intermediates were obtained by metalation of apoMT (adding 25 μM of Cd^{2+} to a 7 μM apoMT solution) and by demetalation of Cd_7MT (adding 700 μM EDTA to a 7 μM Cd_7MT solution); and the Cd_4MT intermediates were then incubated in 10 mM NEM in order to react free cysteinyl groups in the partially-metalated species and DTT in the solution (1 hr, room temperature). The alkylated metalated products were then subjected to direct sequencing by tandem mass spectrometry (top-down approach) or in-solution digestion by trypsin at a weight ratio of 1:40 (trypsin to protein) for 6 hr (bottom-up approach).

Mass spectrometry

All the ESI IM-MS experiments were performed on a Waters Synapt G2 HDMS instrument (Manchester, UK), a hybrid quadrupole/ion mobility (IM)/orthogonal time-of-flight mass spectrometer. MT solution (7 μM) was directly infused into the mass spectrometer at a 0.5 μL/min flow rate. A typical ESI spectrum was collected in positive

ion mode with a capillary voltage of 1.0 – 1.6 kV, sample cone voltage of 40 – 60 V, and extraction cone voltage of 4V. The traveling wave ion mobility cell was operated at a pressure of 2.98 mbar of nitrogen, with a wave velocity of 300 m/s and a wave height of 20 V. All mass spectra were calibrated externally using a solution of sodium iodide.

Top-down sequence experiments were carried out using "MS-CID-IM-MS" as described previously.[110] Briefly, ion of interest is mass-selected by a quadrupole mass spectrometer, and then dissociated using conventional CID conditions. The CID product ions are then separated on the basis of size-to-charge ratio by the 'traveling-wave' ion mobility separator and by *m/z* by the TOF mass analyzer. The CID experiments were performed in trap collision cell with an accelerating voltage of 50 – 70 V. Descriptions of peptide fragment ions are based on the nomenclature system of Roepstorff and Biemann.[111-112] Plotting in a 2-D data display (size-to-charge vs. m/z) yields charge-specific trendlines.[113] Trendlines corresponding to species containing metal ions are shifted relative to the non-metal containing species. Thus, incorporation of IM adds an information-rich dimension to MS-MS, which increases peak capacity and facilitates assignment of fragment ions.

Analysis of apparent binding constant

The apparent binding constant for individual Cd_iMT species is defined by equation 2.1. Seven sequential metalation reactions are proposed for the binding of Cd^{2+} to MT:

$$Cd_{i-1}MT + Cd^{2+} \rightleftarrows Cd_iMT \qquad K_i = \frac{[Cd_iMT]}{[Cd^{2+}][Cd_{i-1}MT]} \qquad (i = 1 - 7) \qquad (2.1)$$

where K_i represents the apparent stepwise binding constant of the $Cd_{i-1}MT$ complex, and $[Cd^{2+}]$ and $[Cd_iMT]$ refer to the equilibrium concentrations of free Cd^{2+} and Cd_iMT species. As shown in equation 2.2, the relative abundances of Cd^{2+}-binding MT intermediate species can be used to estimate the relative apparent binding constants, which are independent of the initial concentration of apoMT, added Cd^{2+} and $[Cd^{2+}]_{free}$ in equilibrium condition.[40,96,114]

$$\frac{K_{i+1}}{K_i} = \frac{[Cd_{i+1}MT]/[Cd_{i-1}MT]}{[Cd_iMT]^2} \qquad (2.2)$$

The titration experiments yielding appreciable amounts of at least three metalated species were selected for K ratio analysis. The abundances of different charge states (4+ and 5+) were summed to provide a total abundance of Cd_iMT species. Using equation 2.2, the K_i ratio can be obtained by the relative abundances of any three adjacent Cd_iMT species. For example, the relative abundances of apoMT, Cd_1MT, and Cd_2MT can be used to calculate K_2/K_1. A baseline correction was performed before calculating the abundances. Twenty-eight separate titration experiments were analyzed to obtain averaged relative apparent binding constants and standard deviations (25 experiments for Zn^{2+}-MT).

Results and Discussion

Monitoring partially-metalated intermediates in metalation/demetalation reactions by ESI MS

Metalation of apoMT was studied by using ESI-MS to monitor the abundances of the metalated product ions following addition of Cd^{2+} to a solution containing apoMT.

Figure 2.3 contains the mass spectra for the region around the 4^+ charge state as the concentration of Cd^{2+} is increased from 0 – 70 μM. Metalation of apoMT (4+; *m/z* 1511.6) yields signals at *m/z* 1538.5 (Cd_1MT^{4+}), 1566.3 (Cd_2MT^{4+}), 1594.4 (Cd_3MT^{4+}), 1622.0 (Cd_4MT^{4+}), 1649.6 (Cd_5MT^{4+}), 1677.2 (Cd_6MT^{4+}), to 1704.8 Da (Cd_7MT^{4+}). The ESI-MS data suggest that Cd^{2+} involves sequential addition of Cd^{2+} to Cd_iMT (i = 0 – 6); however, the ion abundances suggest that the reactivities of the various species differ significantly. For example, the relative abundance of Cd_3MT in the ESI mass spectra is quite low suggesting that this species is reactive toward addition of Cd^{2+}, whereas the high abundance of Cd_4MT suggests that this ion is less reactive in terms of addition of Cd^{2+}. The data suggest the metal-binding affinities of the partially metalated species are quite different.

It should be noted that supermetalated species were not detected in this study, even with an excess of Cd^{2+} (70 μM Cd^{2+}, 10-fold the concentration of MT, see **Figure 2.3**); non-specific association of the free Cd^{2+} to MT due to the ESI process[40,115] was not observed (see **Figure 2.4**). The absence of non-specific binding is attributed to the presence of DTT in the solution, which binds excess free Cd^{2+} thereby reducing non-specific Cd^{2+}-protein binding during the ESI process. These results are consistent with those reported by Konermann *et al.* which show that the use of solution-phase weak metal chelators sequester metal ions and suppress non-specific protein-metal ion binding during the ESI process.[116]

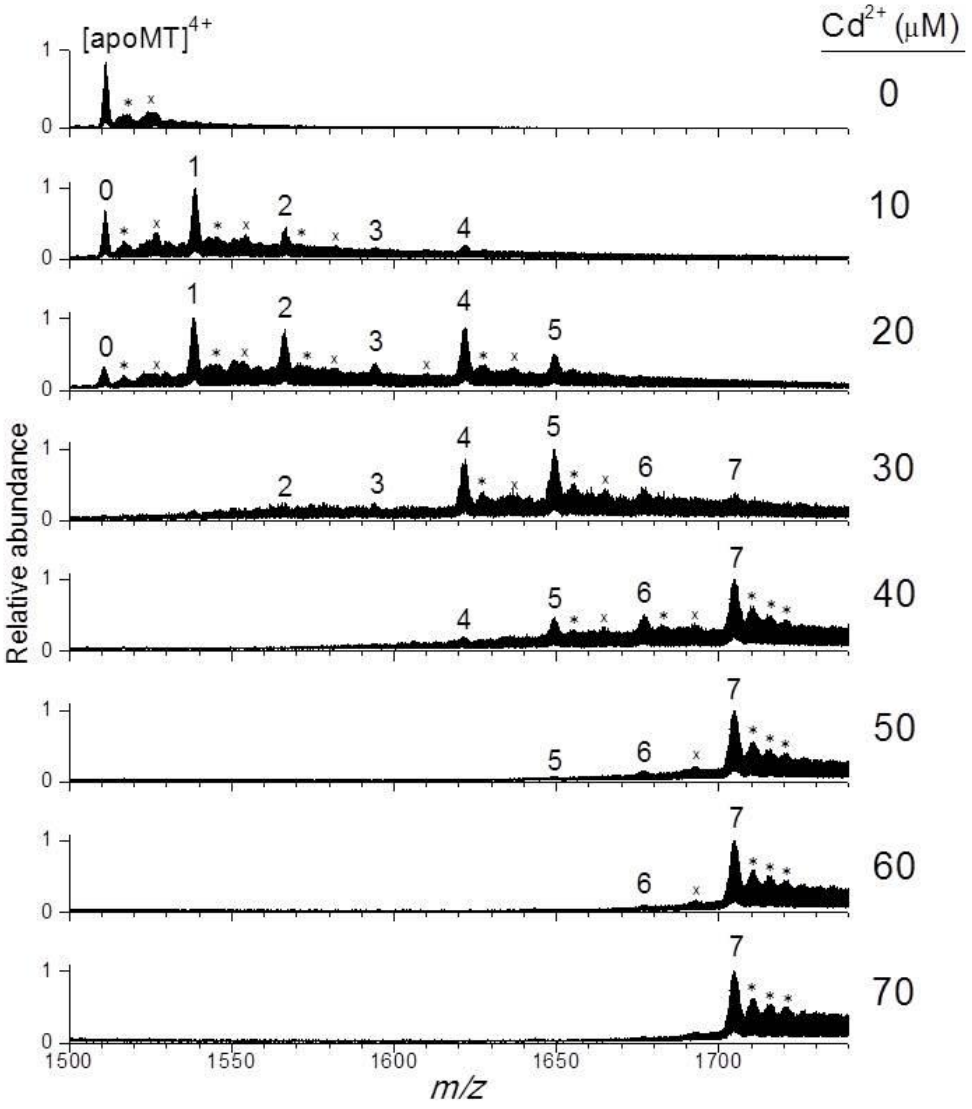

Figure 2.3. ESI-MS spectra of sequential addition of 0 – 70 μM Cd^{2+} to a 7 μM apoMT solution. The Cd^{2+}/MT mixture was incubated at ambient condition for 1 hr between each addition. Data shown are for the 4+ charge state. Numbers above peaks denote the metal stoichiometry of the Cd_iMT^{4+} species (i = 0 – 7). Additional peaks at +23 Da (*) and +60 Da (ˣ) correspond to sodium and acetate adducts.

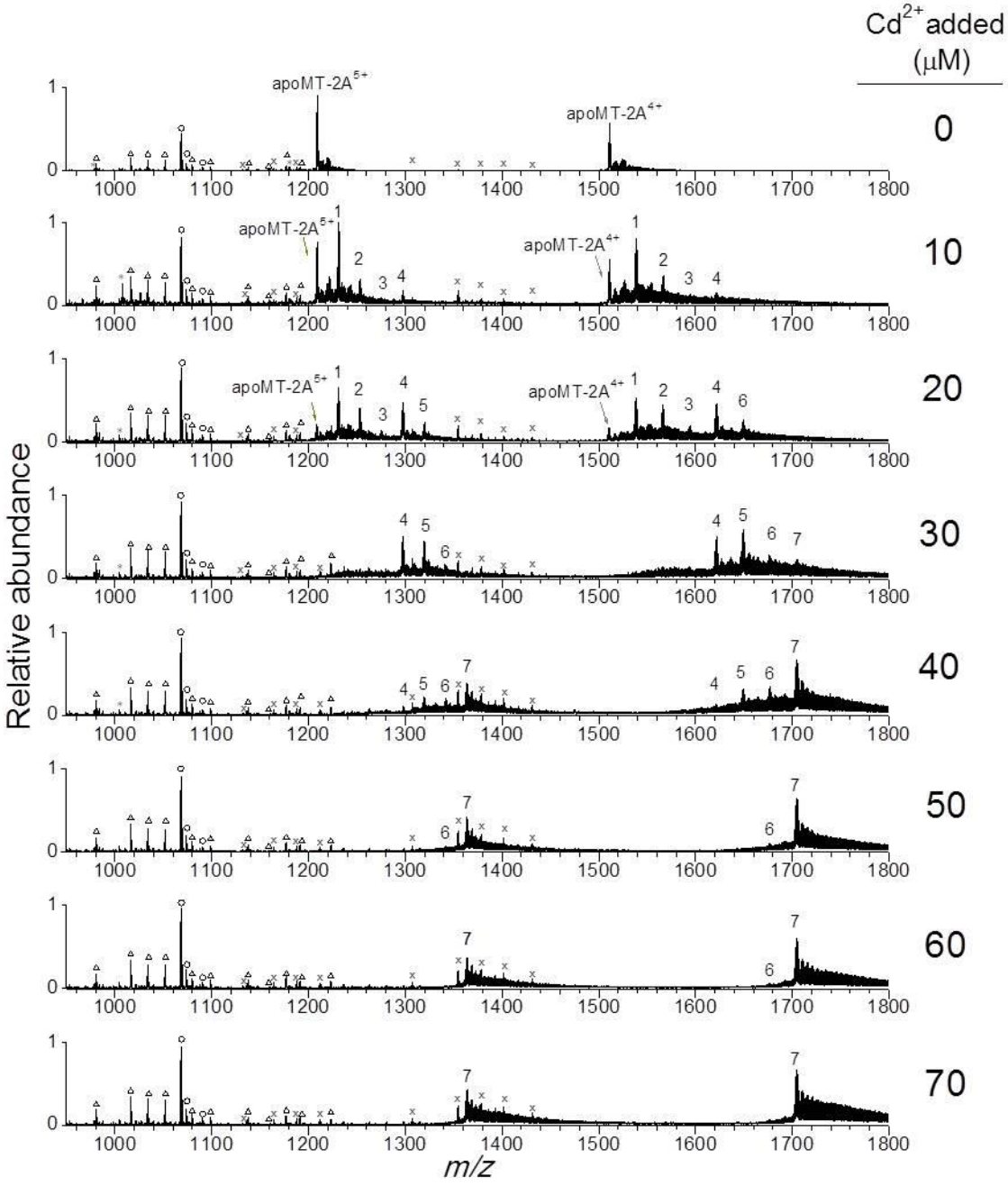

Figure 2.4. ESI spectra of addition of 0 – 7 μL of 1 mM Cd^{2+} solution to a 100 μL of 7 μM apoMT solution. The symbols denote unidentified impurities from the original sample (+2: o; +3: ×; +4: Δ; +5: *). These non-MT species serve as reference proteins for indicating non-specific Cd^{2+} association to proteins. The data showed Cd^{2+} only binds to MT species as the concentration of Cd^{2+} increases, suggesting that non-specific Cd^{2+} association is negligible and the Cd^{2+} binding to MT is specific.

The results for step-wise metalation raise an interesting question: Does demetalation occur by a similar mechanism? This question was addressed by using EDTA to remove the metal ions from Cd_7MT. EDTA is expected to efficiently remove weakly bound Cd^{2+} ions, but more strongly bound or protected metal ions should be removed more slowly, if at all. Addition of 70 μM EDTA to a 7 μM Cd_7MT solution yielded low abundance demetalation products, but as the concentration of EDTA is increased (140 – 500 μM), abundant signals for Cd_iMT (i = 4 – 7) are observed (**Figure 2.5**). At EDTA concentrations above 500 μM, product ions corresponding to Cd_iMT (i = 0 – 4) are observed. Again, Cd_4MT appears to be a relatively stable intermediate, and it appears that Cd_4MT is formed (from apoMT) by step-wise addition of Cd^{2+} to the α-domain and by step-wise depletion of Cd^{2+} from the β-domain (from Cd_7MT) to yield the more stable Cd_4MT. Although both metalation and demetalation appear to be step-wise, the abundances of the Cd_iMT (i = 1, 4, and 5) are much higher than that for i = 2, 3 and 6, suggesting that the reactivities of the individual metalated species differ significantly and depend on the degree of metalation.

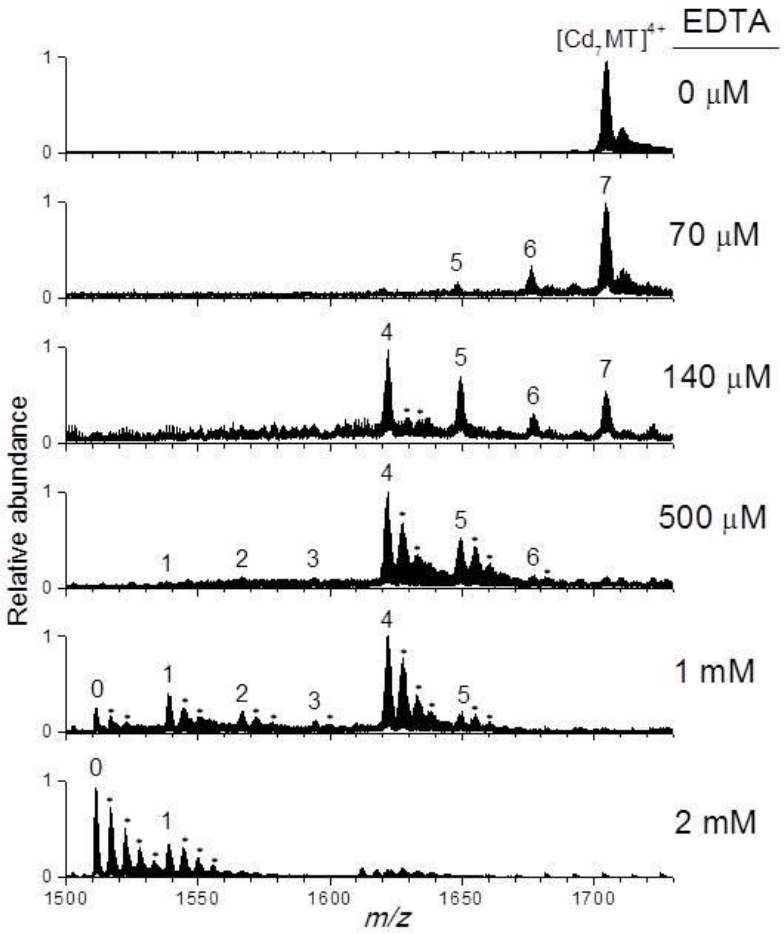

Figure 2.5. ESI-MS spectra of reactions of 0 – 2 mM EDTA to a 7 μM Cd_7MT solution. The spectra were taken after 1 hr incubation at ambient condition. Data shown are for the 4+ charge state. Numbers above peaks denote the metal stoichiometry of the Cd_iMT^{4+} species (i = 0 – 7). The sodium adducts are indicated by asterisks.

Analysis of relative apparent binding affinities between individual metal-binding intermediates

Kägi, Vašák and Valle reported an apparent association constant for Cd^{2+} to MT binding ranging from 10^{15} – 10^{20} M^{-1} using a pH dropping experiment and spectrophotometric analysis.[85-87] Rodriguez and Erk used voltammetry to obtain an

average affinity constant (ranging from $10^9 - 10^{15}$ M^{-1}).[117-118] These studies were based on the assumption that the seven metal ions interact with MT equally, and the difference between the metal-binding properties of individual species (intermediates and end-product) has been neglected and/or is not being detected. However, Maret recently reported three pK_{Zn} to MT and proposed that MT contains three distinct sites where each has different metal-binding affinity.[78]

Klassen previously showed that mass spectrometry data provide quantitative determination of protein-metal ion affinity.[40] Palacios concluded that ESI signals of metal-MT species that differ in their different metalation degree can be related to their relative abundances in solution.[119] Therefore, the various Cd_iMT species (i = 0 – 7) are assumed to share the same ionization efficiency in our study. The relative abundances of Cd_iMT species (i = 0 – 7) in the Cd^{2+} titration experiments can be used to estimate relative binding constants for the Cd_iMT intermediates (equation 2.2, see Experimental Section for more details). The ratios of Cd^{2+}-binding affinities (see **Figure 2.6**) for the first three metal ions are quite small ($K_2/K_1 = 0.21$, $K_3/K_2 = 0.33$), whereas the binding affinity for the fourth metal is much greater ($K_4/K_3 = 16.1$), suggesting that the product formed upon binding the fourth metal ion is more stable and/or less reactive toward further addition of Cd^{2+}. A similar trend is found for $K_5 - K_7$; the binding affinities $K_5/K_4 = 0.20$ and $K_6/K_5 = 0.31$ are much smaller than that for $K_7/K_6 = 3.94$. These ratios can be converted to K_1: K_2: K_3: K_4: K_5: K_6: K_7 = 15: 3.0: 1.0: 16: 3.2: 1.0: 3.9 by normalizing to K_6, suggesting that MT with one, four, and seven metal ions bound are more favorable. The K ratios provide additional data that: (1) Cd^{2+} addition to MT is a

two-step process that produces a stable intermediate Cd_4MT, and (2) there are two independent metalation processes for both steps: (i) $K_i/K_{i-1} < 1$, which means that initially the partially metalated species are highly reactive toward Cd^{2+} ions and the metal-binding event decreases the affinity of the remaining binding sites, and (ii) $K_i/K_{i-1} > 1$, which means that there is a sharp increase in the binding affinity for the last metal ion, for both steps. This indicates that formation of Cd_4MT and Cd_7MT are thermodynamically favored.

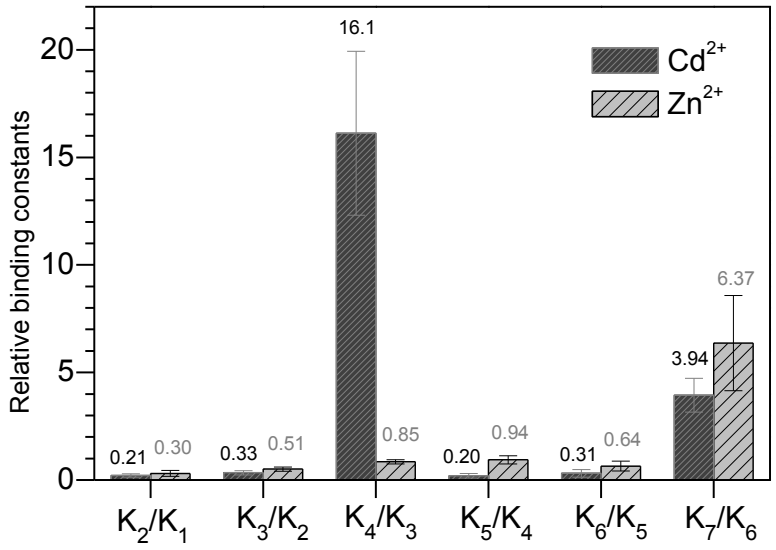

Figure 2.6. Histograms of relative apparent metal-binding constants for apo- and partially-metalated MTs (A) Cd_iMT and (B) Zn_iMT (i = 0 – 6). The K ratios were obtained by analysis of relative abundances of $(metal)_iMT$ complexes in the metal ion titration experiments. See experimental section for more details of data analysis. The difference in profiles for Cd_iMT and Zn_iMT suggests a metal-dependent binding property for human MT-2A.

Metal-dependent binding properties

It is instructive to compare Cd^{2+} and Zn^{2+} binding to MT-2A because the data for CdMT-2A differs markedly from that previously reported for other metals and MT-isoforms.[78,120-122] There is increasing awareness that the metal-binding properties of one isoform can not be directly applied to that of other isoforms;[9,103] therefore, the properties of different metal ions/isoforms must be independently examined. The metal dependence for metalation of human MT-2A was examined by titrating apoMT with Zn^{2+} and following the changes in reaction products by ESI-MS; the same set of conditions was employed for Zn^{2+} as was used for the apoMT and Cd^{2+} studies. Representative spectra are provided in **Figure 2.7**. The data clearly show that the products of metalation Zn_iMT (i = 0 – 7) increase as the Zn^{2+} concentration increases; however, unlike what was observed for CdMT, distinct Zn_iMT intermediates, *i.e.*, i = 4, were not observed. Analysis of the relative apparent metal binding constants for Zn_iMT reveal that all the ratios of K values are < 1 for the binding of the first six Zn^{2+} and greater than 1 for the formation of Zn_7MT (**Figure 2.6**). These data underscore the significant metal-dependent binding properties of human MT-2A. Although this comparison is limited to the metalation of human MT-2A by Zn^{2+} and Cd^{2+}, the results provide clear evidence for the need for additional studies for a broader range of metal ions and MT isoforms.

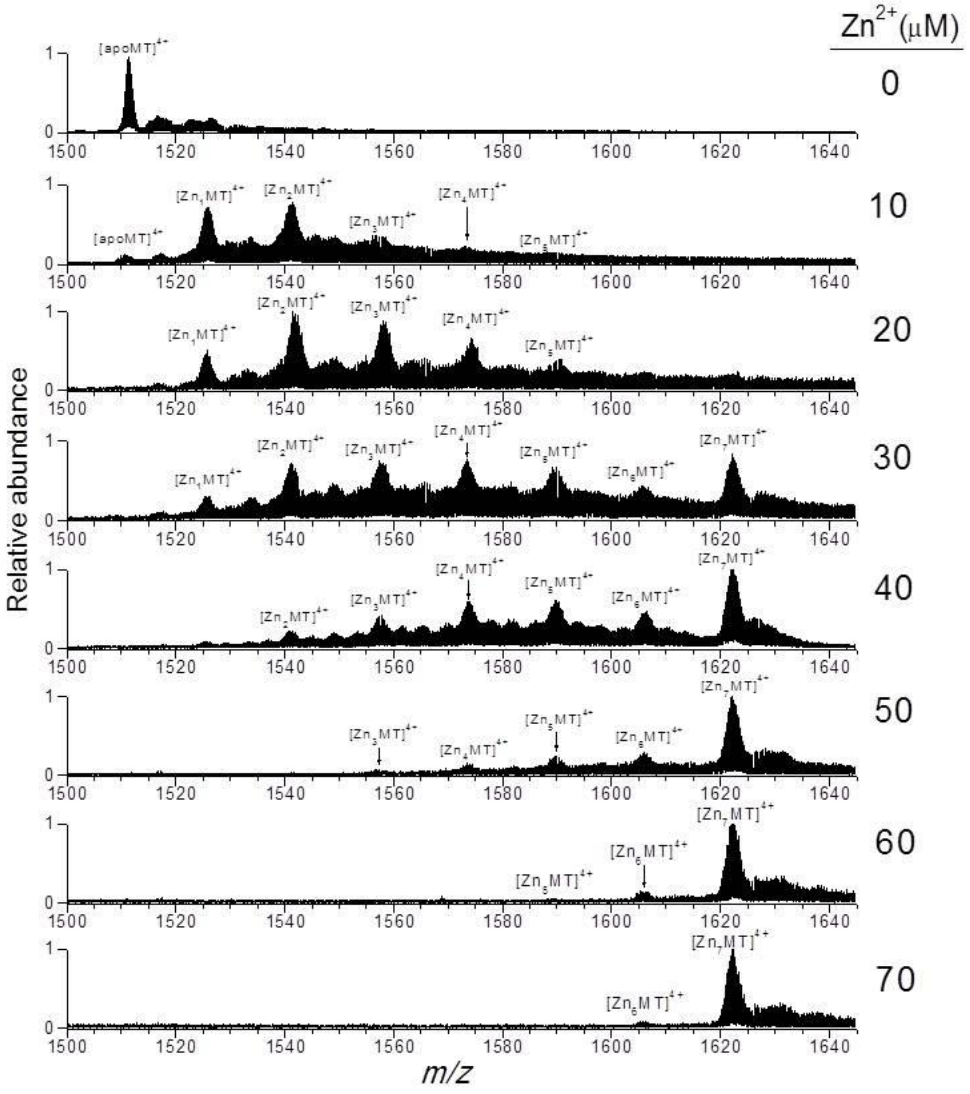

Figure 2.7. ESI spectra of a 7 μM apoMT solution (100 μL) acquired with addition of 0 – 7 μL Zn^{2+} solution (1 mM). The data showed that no distinct Zn_iMT ($i < 7$) intermediates were formed preferentially.

Combining chemical labeling and bottom-up proteomic strategy for identifying metal-binding sites in partially-metalated MT intermediates

Preferential formation of the Cd_4MT intermediates poses a question: Does addition of the four metal ions occur to a single domain (α or β) or are they randomly

distributed between both domains? This question is first addressed by using chemical labeling (NEM) of free cysteinyl thiols[82,123-125] followed by bottom-up proteomics analysis to determine the NEM labeled sites. **Figure 2.8A** contains the MS spectrum obtained from an apoMT solution prior to addition of Cd^{2+}; the signals at *m/z* 1209.4 and 1511.6 correspond to the 5^+ and 4^+ charge states of apoMT, respectively. Following addition of 25 μM of Cd^{2+}, these signals are shifted to *m/z* 1297.7 (5^+) and to 1621.9 (4^+), consistent with formation of Cd_4MT (**Figure 2.8B**). Addition of NEM yields signals at *m/z* 1523.0 (5^+) and 1903.0 (4^+), corresponding to Cd_4NEM_9MT (**Figure 2.8C**). An aliquot of this solution was then subjected to tryptic digestion for "bottom-up" characterization (**Figure 2.8D**). Peptides labeled P_1, P_2, P_3, P_4, P_5, and P_7 correspond to metal-free and NEM-labeled tryptic fragment ions; the peptides are assigned as C^{21}-K^{22}, E^{23}-K^{25}, C^{26}-K^{30}, C^{21}-K^{25}, C^{26}-K^{31}, M^1-K^{20}, respectively. Note that these peptide ions all correspond to the cleavage products from the β-domain. The signals labeled P_6 and P_8 are assigned as 3^+ and 2^+ ions of intact α-domain (K^{32}-A^{61}) with four Cd^{2+} ions bound; this assignment was confirmed by CID MS (see **Figure 2.9**). The entire sequences and detailed masses of identified fragment ions are listed in **Table 2.1A**. It is of interest to note that digestion of Cd_4NEM_9MT produced peptides from the metal-free β-domain in < 10 min, whereas the signal for P_6 remained unchanged for > 24 hr, indicating that the four Cd^{2+} ions are tightly bound and/or inaccessible to solvent. The data provide convincing evidence that Cd^{2+} ions are preferentially added to the α-domain in agreement with results reported by Winge and coworkers.[126]

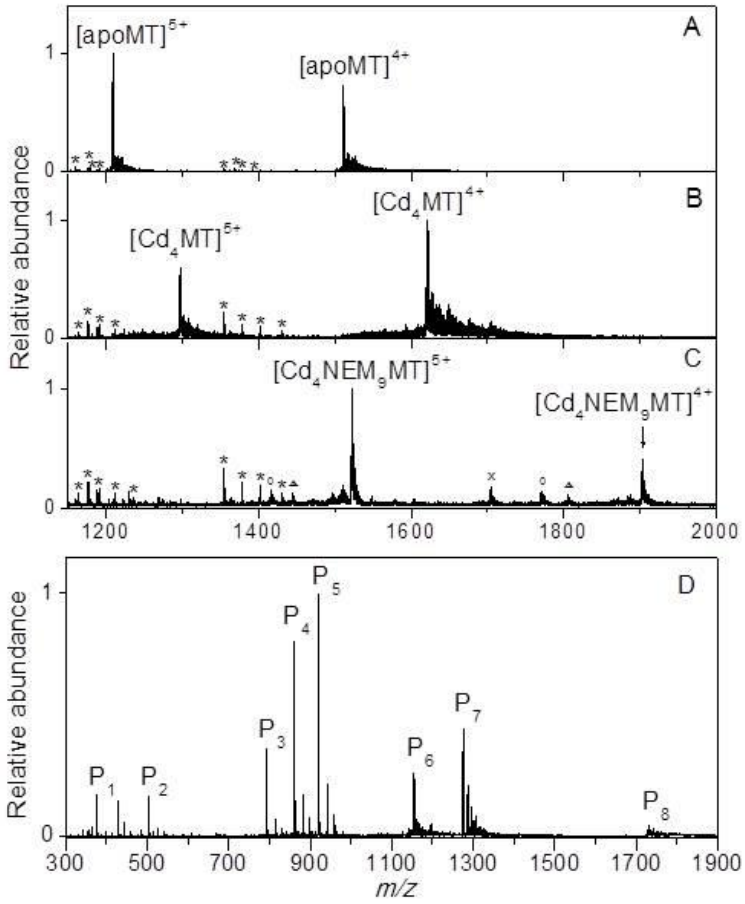

Figure 2.8. ESI mass spectra of (A) a 7 μM apoMT solution acquired before titration; (B) partially-metalated Cd_4MT species obtained by addition of 25 μM Cd^{2+} ions to above solution at ambient conditions for 1 hr; and (C) reaction product of Cd_4MT in 10 mM NEM. The labeling reaction was carried out at ambient conditions for 1 hr. The asterisks (*) denote the impurities present in the apoMT solution; the cross ($^{\times}$) indicates Cd_7MT; the circles (°) denote Cd_6NEM_3MT; the triangles ($^{\triangle}$) indicate Cd_5NEM_5MT. (D) ESI spectrum of tryptic digests of the reaction product Cd_4NEM_9MT obtained in (C). The digestion was performed at 37°C at an enzyme: protein ratio 1:40 for 1 hr. The identified fragment ions and corresponding sequence are listed in Table 2.1A. The sequence of P_6 was confirmed by CID MS.

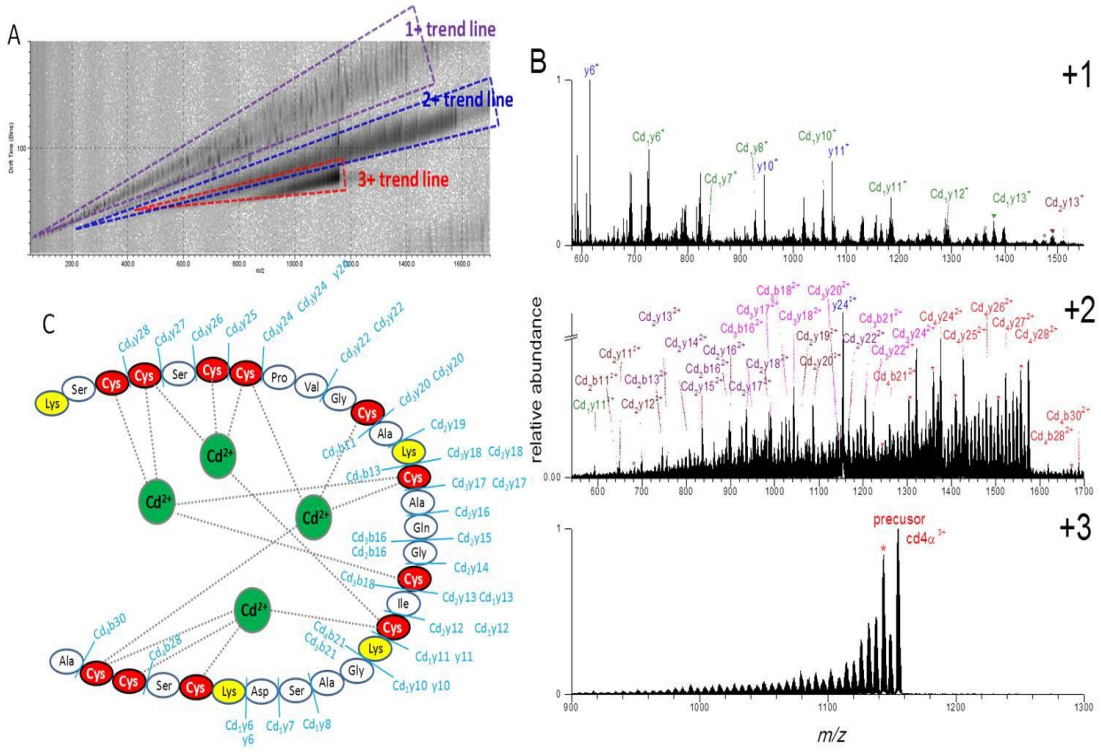

Figure 2.9. Top-down sequencing of fragment ion P_6. The mass of P_6 matches the triply-charged intact α fragment (residue 31-61) with 4 Cd^{2+} bound. To confirm the assignment, the intact $Cd_4\alpha$ fragment was subjected to directly sequencing using top-down MS-CID-IM-MS approach. The precursor ion P_6 was selected by quadrupole and then fragmented in trap collision cell. The fragment ions are separated on the basis of size-to-charge ratio by ion mobility separator and by *m/z* by the TOF mass analyzer. The 2D ion mobility-m/z separation is shown in (A), and the extracted trendlines from the 2D plot are shown in (B). The summary of fragment ions identified in shown in (C). The data confirmed the fragment ion P_6 is intact $Cd_4\alpha$ domain.

(A)

No.	Sequence	Assignment	#Cd(II)	#NEM	Theoretical mass (a/b)*	Charge	Observed m/z
P_1	CK	21-22	0	1	250.121 / 375.170	1+	375.232
P_2	ECK	23-25	0	1	379.165 / 504.212	1+	504.299
P_3	CTSCK	26-30	0	2	541.211 / 791.306	1+	791.436
P_4	CKECK	21-25	0	2	610.269 / 860.364	1+	860.508
P_5	CTSCKK	26-31	0	2	669.306 / 919.401	1+	919.549
P_6	KSCCSCCPVGCAKCAQGCIC KGASDKCSCCA	31-61	4	0	3022.658** / 3461.661**	3+	1154.741
P_7	MDPNCSCAAGDSCTCAGSCK	1-20	0	5	1923.647 / 2548.885	2+	1275.161
P_8	KSCCSCCPVGCAKCAQGCIC KGASDKCSCCA	31-61	4	0	3022.658** / 3461.661**	2+	1731.609

* theoretical $[M+H]^+$ of peptides (a) without and (b) with Cd^{2+}- and NEM- bound

** average mass

(B)

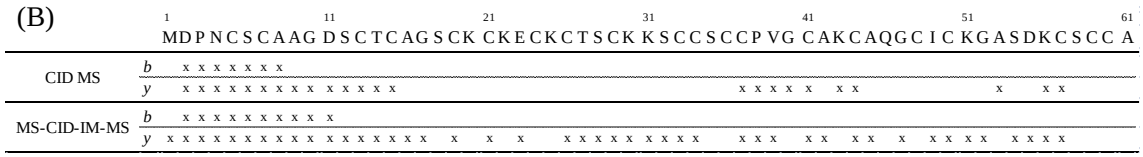

Table 2.1. Identified fragment ions and sequence coverage of bottom-up (A) and top-down (B) analysis of Cd_4NEM_9MT.

Direct identification of metal-binding sites of partially-metalated intermediates by top-down "MS-CID-IM-MS"

Top-down proteomics strategies, specifically MS-CID-IM-MS,[110] were also employed to sequence the Cd_4NEM_9MT ion. This approach minimizes potential ambiguity that might arise from metal transfer among binding sites during sample preparation and subsequent analysis by the "bottom up" approach. The MS-CID-IM-MS experiment involves m/z selection of the $[Cd_4NEM_9MT]^{5+}$ ion, followed by CID of the m/z selected ion and separation of CID product ions on the basis of ion mobility and *m/z*. **Figure 2.10A** contains the 2D IM-MS plot of the fragment ion spectra of the $[Cd_4NEM_9MT]^{5+}$ ion. Note that fragment ions that have different charge states fall along distinct trendlines, and trendlines for metal ion-containing fragment ions are separated

from the metal-free trendlines. Extracting mass spectra along each trendline reduces spectral congestion and simplifies assignment of product ions, thereby facilitating data interpretation (**Figure 2.10B**). A series of metal-free, β-domain fragment ions ranging from b_2 to NEM_7b_{25} and y_{31} to y_{60} contain 0 – 9 NEM labels, suggesting that the nine cysteines in β-domain are fully labeled by NEM. The series of metal containing y ions ranging from y_5 to y_{60} provides unequivocal evidence that the four Cd^{2+} ions are located in α-domain. **Figure 2.10C** summarizes the identified fragment ions and the model of the Cd_4NEM_9MT species. The results confirm the digestion experiments, *i.e.*, that the Cd_4 α-domain is preferentially formed upon Cd^{2+} coordination to MT.

These results illustrate the utility of combining chemical labeling and MS-CID-IM-MS for direct determination of metal binding sites. Chemical labeling by NEM avoids potential ambiguity introduced by metal transfer reactions between binding sites and the "top-down" experiments avoid any ambiguity that may arise from (1) low abundant tryptic peptides derived from impurities and species other than Cd_4NEM_9MT (see **Figure 2.8C**), and (2) the recombination of metal ions and digested fragment ions in the ("bottom-up") solution.

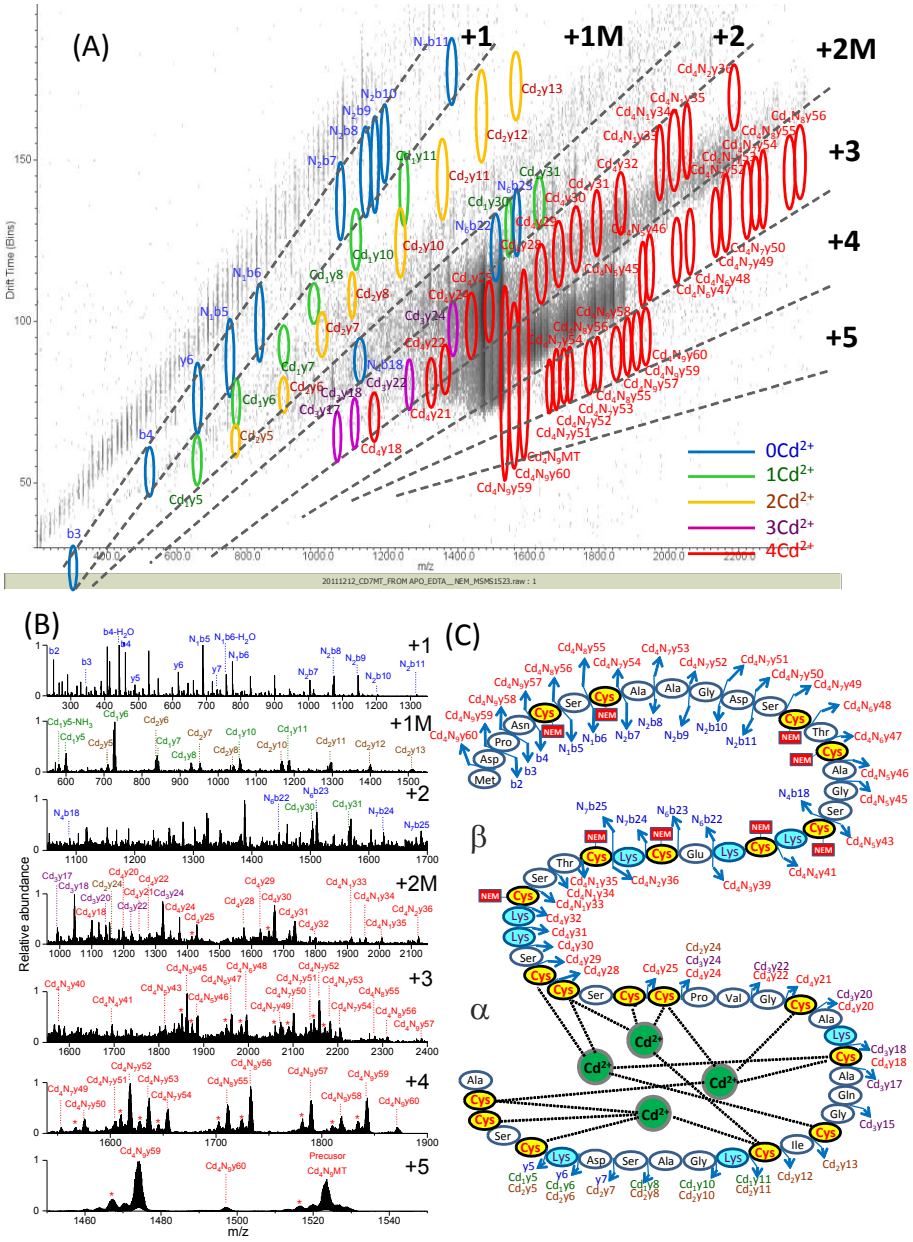

Figure 2.10. Top-down sequencing of metalation intermediates Cd_4NEM_9MT. (A) 2D MS-CID-IM-MS spectrum of $[Cd_4NEM_9MT]^{5+}$. The trendlines are shown for ions of different charge states as labeled (+1 to +5). The +1 and +2 fragment ions with metal ions bound are indicated as +1M and +2M, respectively. NEM is abbreviated as "N" for simplicity. (B) Extracted mass spectra for each trendline. Peaks with an asterisk are for ions that shifted by ~ 35 Da from the y fragment ions, corresponding to loss of ammonia and water. (C) Summary of identified fragment ions and corresponding model from (B). The dotted lines between metal ions and cysteines indicate the metal-thiol coordination resolved from NMR studies. α and β indicate the location of the domains.

The full characterization of metal-binding sites of the partially-metalated intermediates is attributed to the 2D IM-MS separation. Note that 109 fragment ions (see **Figure 2.10B**) are assignable on the basis of the 2D IM-MS data as opposed to 63 fragment ions from the 1-D CID MS spectrum (see **Figure 2.11**). In addition, identified fragment ions from 1-D CID MS spectrum are derived from the protein termini (**Table 2.1B**, **Figure 2.11**), signals derived from residues 15 – 35 are not assigned, and these are essential for identification of all metal ion and NEM-binding sites. The 2D IM-MS provides separation of the overlapping fragment ions, thereby facilitating detection of low abundant fragment ions and full characterization of metal-binding sites (**Table 2.1B**, **Figure 2.10**). Collectively, the data demonstrate that by combining chemical labeling and 2D MS-CID-IM-MS, the intact partially-metalated intermediates can be trapped directly and binding sites can be fully characterized without any further sample treatments.

Top-down sequencing was also employed to characterize the demetalation intermediate Cd_4MT. Briefly, the Cd_4MT intermediate was obtained by adding 100 equivalents of EDTA to a solution of Cd_7MT; after 1-hr, NEM was added to the solution to form Cd_4NEM_9MT (see **Figure 2.12**). The 2D IM-MS data for Cd_4NEM_9MT generated by demetalation clearly show that the four Cd^{2+} ions that reside in the α-domain are retained, whereas the Cd^{2+} ions in the β-domain are removed (by EDTA) and the free binding sites are all labeled by NEM (**Figure 2.13**). The experiment provides further evidence that the binding of Cd^{2+} to human MT involves a two-step domain-

specific mechanism, *i.e.* metal ions are first added to the α-domain followed by addition to the β-domain, metal ions are removed in the reverse order.

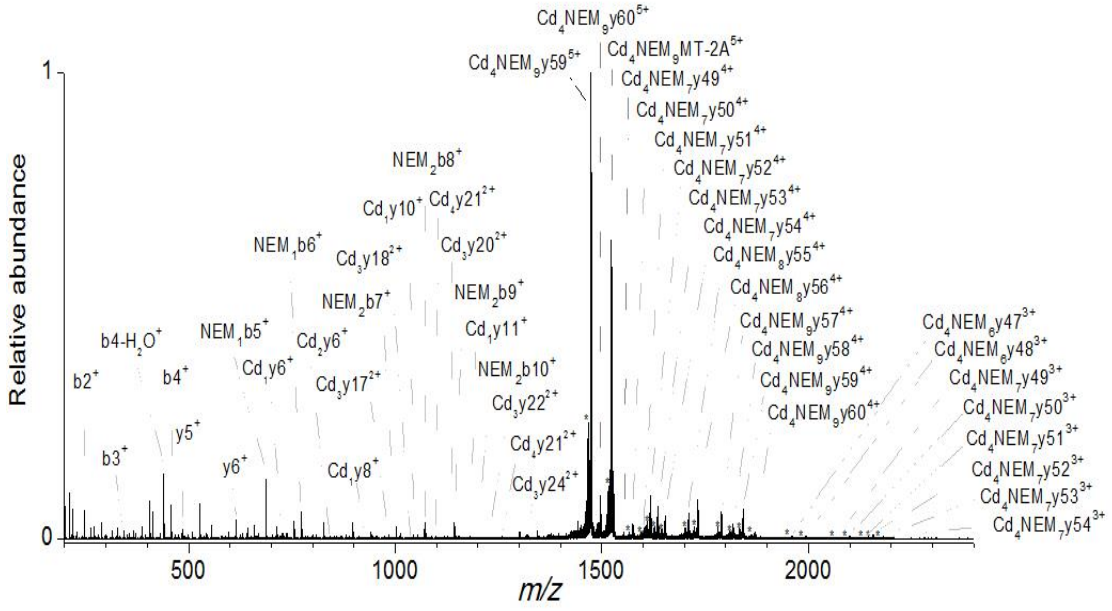

Figure 2.11. Regular CID MS spectra of $[Cd_4NEM_9MT]^{5+}$. A total of 63 fragment ions are identified. The sequence coverage is shown in Table 2.1.

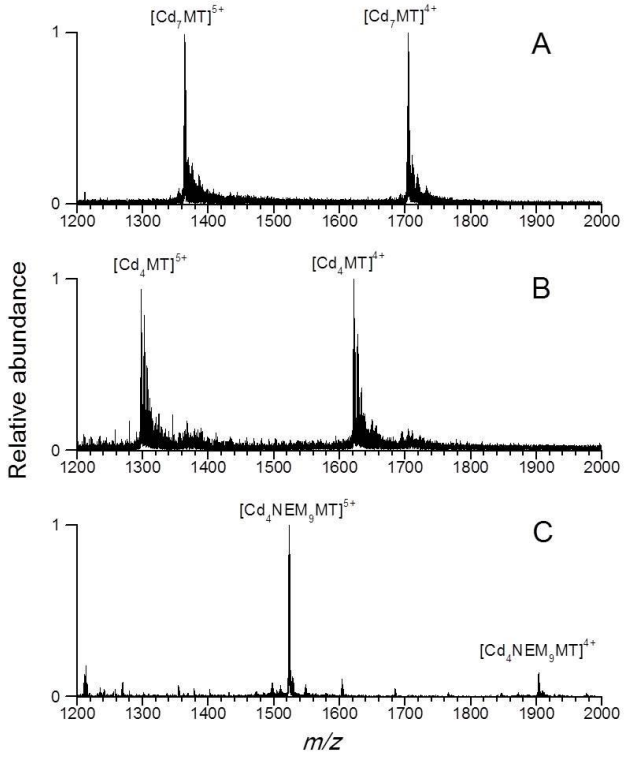

Figure 2.12. ESI spectra of a 7 μM solution of (A) Cd_7MT acquired before any treatments, and sequential addition of (B) 700 μM EDTA and (C) NEM (final concentration 10 mM). A stable partially-metalated Cd_4MT species was obtained after 1 h reaction of Cd_7MT and EDTA, and reaction of Cd_4MT and NEM yields Cd_4NEM_9MT. The reaction product Cd_4NEM_9MT was then subjected to directly sequencing by MS-CID-IM-MS approach.

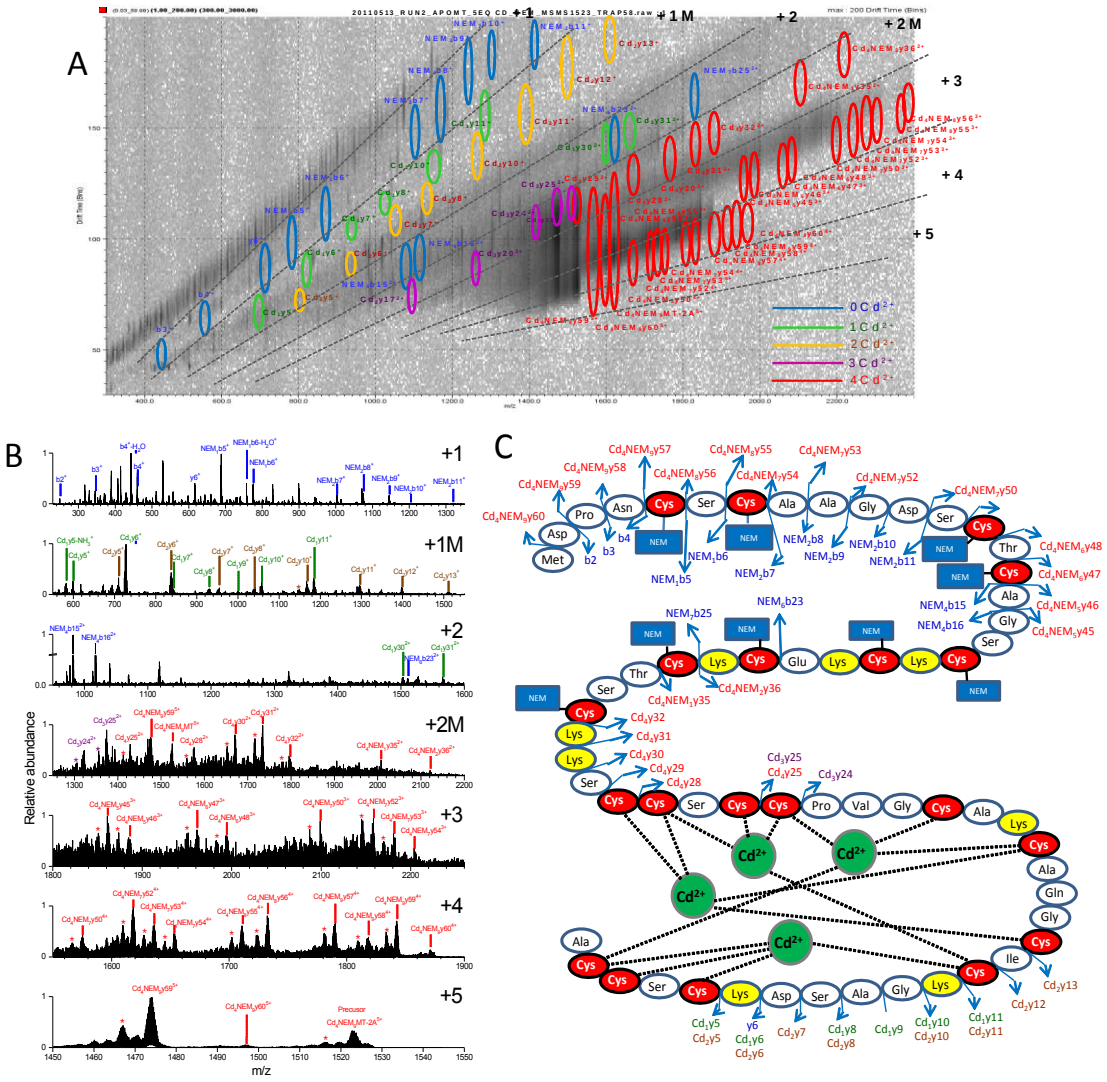

Figure 2.13. Analysis of metal-binding sites of partially-metalated Cd_4MT intermediate obtained from the metal ion removal of Cd_7MT by EDTA. The product Cd_4NEM_9MT was then subjected to MS-CID-IM-MS analysis. (A) 2D IM-MS plot of fragment ions, (B) extracted mass spectra for each trendlines, (C) summary of identified fragments and corresponding model. The data demonstrates the four Cd^{2+} located in α domain are strongly bound and retained in the demetalation process.

Conclusion

ESI-IM-MS is used to probe the relative metal-binding affinities between individual partially-metalated metallothioneins, and direct identification of metal-binding sites in partially-metalated intermediates is probed by combining chemical labeling (NEM) of cysteine side chains with bottom-up and top-down proteomics techniques. The relative apparent binding constants reveal distinct binding pathways for human Zn_iMT-2A and Cd_iMT-2A (i =0 – 7). The discovery of a stable intermediate, Cd_4MT, indicates that Cd^{2+} binds MT through a two-step process; conversely, Zn^{2+} reacting with apoMT does not yield similar Zn_iMT intermediates. The Cd_4MT intermediate was characterized by using chemical labeling and 2D IM-MS top-down approach, providing site-specific information for the metal-binding sites of intact partially-metalated MT. These results provide direct evidence that Cd^{2+} binding to human MT-2A occurs by a two-step mechanism that is domain specific: the $Cd_4\alpha$-domain is preferentially formed followed by filling of the β-domain, and demetalation (by EDTA) occurs by reversing this sequence. The data also indicate the $Cd_4\alpha$-domain is more thermodynamically and kinetically stable relative to the $Cd_3\beta$-domain. These results highlight the advantage of MS-based approaches for studies of binding mechanism of proteins involving multiple metal ions. The MS data for reaction intermediates and final products can be distinguished and specific metalated forms can be directly selected and characterized for the binding sites without the need of sample purification. This study provides essential guidance for future investigations employing IM-MS to gain insights into the correlation between reactivities and 3-D structures of the

various partially-metalated species and structural transitions between the Zn^{2+} and Cd^{2+}-induced folding.

CHAPTER III

PROBING KINETIC STABILITIES OF METAL ION-BINDING SITES IN HUMAN CD7METALLOTHIONEIN BYN-ETHYLMALEIMIDE: EVIDENCE FOR A WEAKLY COORDINATED SITE IN THE ALPHA DOMAIN

Introduction

Metallothioneins (MTs) constitute a family of low molecular weight proteins with a high cysteine content and are known for their ability to interact a wide variety of metal ions. Mammalian MTs are known to bind seven divalent (Cd^{2+} or Zn^{2+}) ions or twelve monovalent (Cu^{+}) ions in two metal-sulfur clusters. MTs are proposed to play a role in detoxification of heavy metal ions and regulation of essential metal ions. In addition to metal ions, MTs are also reactive toward oxidants, electrophiles and alkylating agents such as iodoacetamide and N-ethylmaleimide (NEM). It has been proposed that MTs confer resistance toward anticancer therapeutics by alkylation of cysteine residues and the overexpression of MTs in cancer cells attenuates toxicity of antitumor therapeutics and provides intracellular drug sequestration. These results indicate that MT might react with a variety of biologically active electrophiles and thereby alter their cellular effects.[82] Results from these studies suggest that the active form(s) of MT *in vivo* is probably not the well-known fully-metalated structure described by X-ray crystallography or NMR spectroscopy and that the thiol chemistry is the central of MT's mechanism of action.[75]

Fluorimetric methods have been developed to glean information on mechanistic insights into metalation/demetalation/metal-displacement reactions of MTs. Results from these studies suggest that the metal ions (Zn^{2+} and Cd^{2+}) are thermodynamically stable but kinetically unstable, and the metal ions in the β domain are more dynamic than those in the α domain. These real-time kinetic studies usually rely on external metal-ion reactive fluorescent reporters, thus the information obtained are limited to the amount of metal ions bound/released. Consequently, the information about distribution of reaction intermediates is largely unknown. On the other hand, using state-of-the-art MS-based techniques it is possible to resolve signals from individual conformers in the solution and to provide direct information on the reaction intermediates.

Here we report detailed kinetic profiles for each of the metal-displaced intermediates of MT in the reaction with a model alkylating agent N-ethylmaleimide (NEM). NEM has been long used to quantify the free cysteine residues in MTs through the formation of covalent thioether bonds.[85] In our study, NEM is used to probe the dynamic metal ions. The molecular-specific kinetics provides direct information on the mechanism of displacement reaction and evidence for the cooperative binding of the two domains. Furthermore, we have previously showed the utility of MS-CID-IM-MS has been previously shown for structural characterization of short-lived partially-metalated intermediates. Here, a stable partially-alkylated metal-retaining intermediate was isolated and directly sequenced by mass spectrometer, providing direct information on the metal ion- and NEM binding sites. Our data reveals a weakly coordinated site in the α domain.

Experimental

Sample preparation

Cadmium-saturated MT-2A (Cd_7MT) powder sample (Bestenbalt LLC, Tallinn, Estonia) was reconstituted to 10 μM in 50 mM ammonium acetate (pH 7.4) containing 10% methanol and 5 mM DTT (Sigma-Aldrich**,** St. Louis, MO). Metal displacement reaction was performed by adding 1, 20, 40, 80, 320, and 2000 molar equivalents of NEM to a 10 μM Cd_7MT solution. The solution was incubated for 1 h at room temperature and then analyzed by ESI-MS. The kinetic study of metal displacement was carried out by adding 200 equiv NEM to a 10 μM Cd_7MT solution. Aliquots were taken at various intervals from the time of mixing and the reaction was monitored continuously by ESI-MS for 24 h at room temperature.

To identify the metal-ion binding sites in a partially-metalated intermediate, the alkylated partially-metalated intermediate is m/z selected and then subjected to direct top-down sequencing *viz.* a stable reaction intermediate $Cd_4NEM_{10}MT$ yielded after 1 h-reaction of Cd_7MT and 200 equiv NEM is subjected to top-down tandem mass spectrometry (MS-CID-IM-MS-approach) as described previously.[127]

Ion mobility-mass spectrometry

All mass spectra and drift time were collected using a Waters Synapt G2 HDMS instrument (Manchester, UK). 10 μM sample solution was directly infused into the mass spectrometer at a 0.5 μL/min flow rate. ESI spectra was collected in positive ion mode with a capillary voltage of 1.0 – 1.5 kV using a sample cone voltage of 10 V and extraction cone voltage of 1 V. All mass spectra were calibrated externally using a

solution of sodium iodide. He and N_2 ratio in the traveling wave ion mobility cell was optimized toward a lower effective ion temperature. A TW wave velocity of 550 m/s and a wave height of 25 V were used. Cytochrome c, myoglobin and ubiquitin were used to calibrate collision cross section (CCS) as described previously.[128]

Kinetic analysis

Relative abundances were determined by performing a baseline correction and calculating the area under the peaks. The abundance of species with the same number of metal ions bound (i = 0 – 7) in different charge states were summed together to provide a total abundance of Cd_iMT species. The kinetic data were analyzed using Mathematica (Wolfram Research Inc., Champaign, IL). Seven consecutive, irreversible reactions were proposed to account for the reaction of Cd_7MT and 200 equiv NEM (equation 3.1, see below for the detailed rate low). The seven rate constants were empirically determined to obtain best fit of the experimental data.

$$Cd_7 \xrightarrow[NEM]{k_7} Cd_6 \xrightarrow[NEM]{k_6} Cd_5 \xrightarrow[NEM]{k_5} Cd_4 \xrightarrow[NEM]{k_4} Cd_3 \xrightarrow[NEM]{k_3} Cd_2 \xrightarrow[NEM]{k_2} Cd_1 \xrightarrow[NEM]{k_1} Cd_0 \quad (3.1)$$

define $[Cd_7]_0 = 1; [Cd_6]_0 = 0; [Cd_5]_0 = 0; [Cd_4]_0 = 0; [Cd_3]_0 = 0; [Cd_2]_0 = 0; [Cd_1]_0 = 0; [Cd_0]_0 = 0$

rate laws:

$$\frac{d[Cd_7]}{dt} = -k_7[Cd_7]$$

$$\frac{d[Cd_6]}{dt} = k_7[Cd_7] - k_6[Cd_6]$$

$$\frac{d[Cd_5]}{dt} = k_6[Cd_6] - k_5[Cd_5]$$

$$\frac{d[Cd_4]}{dt} = k_5[Cd_5] - k_4[Cd_4]$$

$$\frac{d[Cd_3]}{dt} = k_4[Cd_4] - k_3[Cd_3]$$

$$\frac{d[Cd_2]}{dt} = k_3[Cd_3] - k_2[Cd_2]$$

$$\frac{d[Cd_1]}{dt} = k_2[Cd_2] - k_1[Cd_1]$$

$$\frac{d[Cd_0]}{dt} = k_1[Cd_1]$$

MD simulations

MD simulations were performed using AMBER 9.0. FF99SB force field.[129] The NMR structures of separate domains (1MHU, 2MHU)[37] of human MT-2A was connected as starting structure for fully-metalated Cd_7MT. The simulation and parameters for Cd^{2+} ion follows the procedure described previously.[65] Topology and partial charge of NEM-labelled cysteine will be generated using RESP ESP charge Derive program (RED).[130] The structures of Cd_4NEM_{10}MT and NEM_{20}MT were energy-minimized, following by simulations at 300 K *in vacuo* or implicit solvent model to generate gas phase- and solution phase structures. Dehydrated structures were

obtained by *in vacuo* minimization of solution phase structures for 10,000 steps as described previously.[65] CCS calculations were carried out using trajectory method.[131]

Results and Discussion

Metal displacement of Cd_7MT by NEM

Displacement of Cd^{2+} ions from Cd_7MT was studied by sequentially adding an alkylation agent NEM in to a Cd_7MT solution (**Figure 3.1**). Addition of small amounts of NEM (< 40 equiv) does not lead to significant amounts of Cd^{2+} displacement. We note that the 7 Cd^{2+} ions can be still bound even the protein is labelled by a few number of NEM eg. Cd_7NEM_3MT at 20 equiv NEM (**Figure 3.1**). Increasing the concentration of NEM yielded more extensive NEM labeling and metal-release. After 40 equiv NEM, product ions corresponding to four Cd^{2+}-bound metalated intermediates (Cd_4 species) are observed. Above 80 equiv NEM, $Cd_4NEM_{10}MT$ intermediate is the most abundant product. In solutions having high molar excess of NEM (2000:1 to Cd_7MT), the $Cd_4NEM_{10}MT$ remains as the dominant species and the metal-stripped MT containing 20 NEMs are detected at lower abundance.

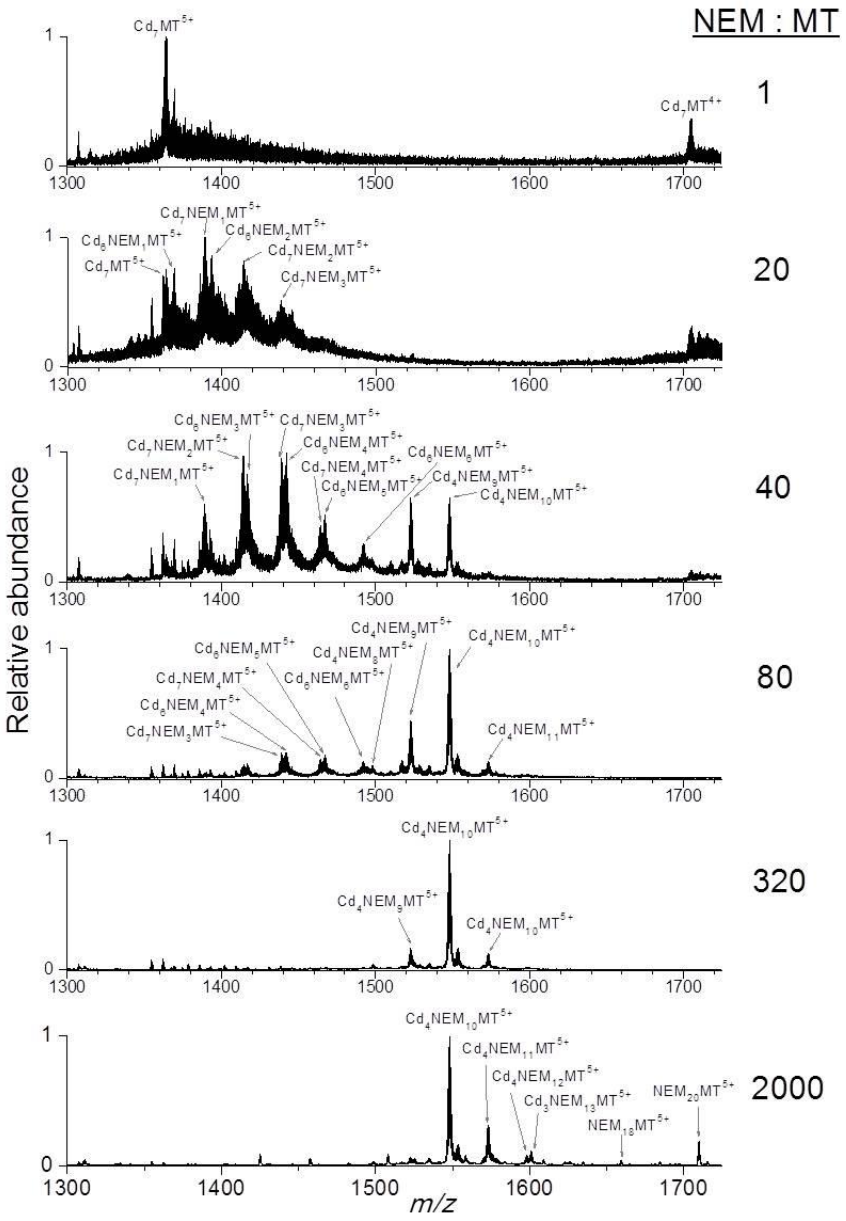

Figure 3.1. ESI-MS spectra of a solution of Cd_7MT to which 1 – 2000 equiv NEM were added. $Cd_4NEM_{10}MT$ was observed as the most stable intermediate during the entire titration. Data shown limited to 5+ region.

A weakly coordinated metal ion binding site in the α domain

The most stable intermediate, $[Cd_4NEM_{10}MT]^{5+}$, was analyzed by MS-CID-IMS-MS[127] to identify the locations of metal ions in the Cd_4 species (**Figure 3.2**). A series of β-domain fragments including b ions from b_2 to NEM_7b_{25} and y ions from y_{31} to y_{60} with 0–9 NEM bound suggest that the nine cysteines in β-domain are fully labeled by NEM. The presence of a series of Cd^{2+} ion containing y ions from y_5 to y_{60} also provides evidence that the four Cd^{2+} ions are located in α-domain. The data show that the four Cd^{2+} ions located in the α-domain are tightly bound, whereas the three Cd^{2+} ions bound to the β-domain are replaced upon addition of nine NEMs. In addition, the presence of fragment ions Cd_4y_{28} and $Cd_4NEM_1y_{29}$ are consistent with alkylation to cys[33] in the α-domain. This result suggests that the NEM reaction is consistent with the two-step domain-specific displacement mechanism, *i.e.* the four Cd^{2+} ions resided in the α-domain are strongly bound even in the presence of a large excess of chelator or electrophile.

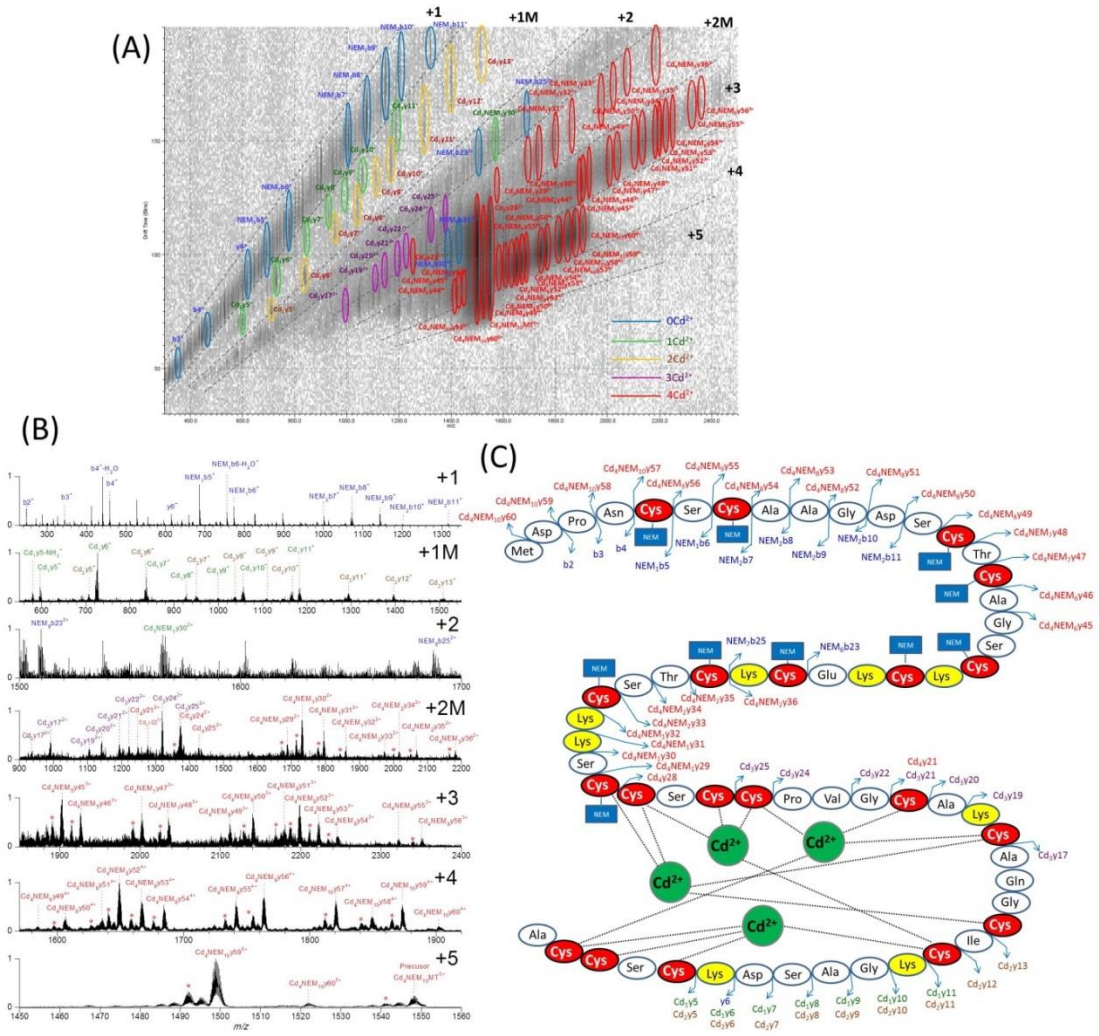

Figure 3.2. MS-CID-IM-MS analysis of the demetalation intermediate $[Cd_4NEM_{10}MT]^{5+}$. (A) 2D IM-MS plot of fragment ions, (B) extracted mass spectra for each trendlines, (C) summary of identified fragments and corresponding model. This result demonstrates the four Cd^{2+} located in α domain are strongly bound and retained in the displacement reaction by NEM.

Displacement kinetics

Kinetic stabilities of the individual partially-metalated intermediates were examined by monitoring individual signals as a function of time with NEM concentration held constant (200: 1 to Cd_7MT) (see MS spectra in **Figure 3.3**). The removal of Cd^{2+} from Cd_7MT over 24 h appears to be a two component reaction; rapid loss of three metal ions followed by slow loss of the remaining four metal ions. The Cd_4 species was observed as the least reactive intermediate during the entire displacement process. The reaction was assumed to occur through sequential displacement from Cd_7MT with seven individual displacement rates (see Experimental section).

Under the condition of large excess of NEM, the reaction is assumed to follow first-order kinetics. The reactions are also irreversible because the resulting thioether C-S bonds are covalent. **Figure 3.4** contains kinetic plots for individual intermediates and end-product. The kinetic data for Cd_7 species follows an exponential decay, whereas the Cd_6 – Cd_1 species show an initial rise followed by an exponential decay to the final Cd_0 products. The equivalents of Cd^{2+} ions retained by MT over time can be calculated from the abundance of Cd_iMT species present in the solution (see **Figure 3.4I**). A biexponential decay is observed with a cross point at 1.4 which corresponds to 4.3 equiv Cd^{2+}. The NEM labeling and subsequent release of three metal ions was initially fast ($k_{Cd^{2+},\,fast}$: 8.4×10^{-3} min^{-1}, < 50 min), and the latter reaction to remove the last four metal ions required > 24 h ($k_{Cd^{2+},\,slow}$: 4.8×10^{-4} min^{-1}).

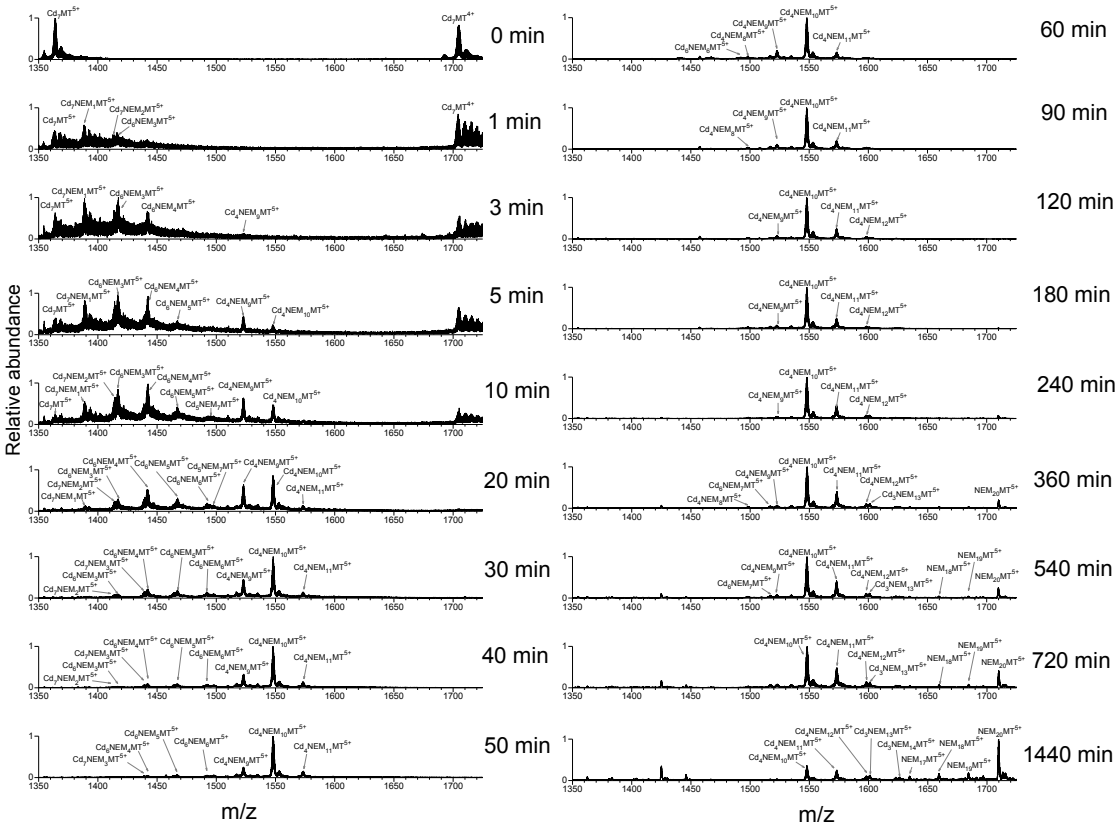

Figure 3.3. Reaction of Cd_7MT and 200 equivalents of NEM. The reaction was continuously monitored by ESI-MS over 24 hr. Signal of Cd_iMT with different number of NEM bound (x; 0-20) are combined to provide a total abundance of a Cd_i species. Kinetic curve and fitting of individual Cd_i species was shown in Figure 3.4.

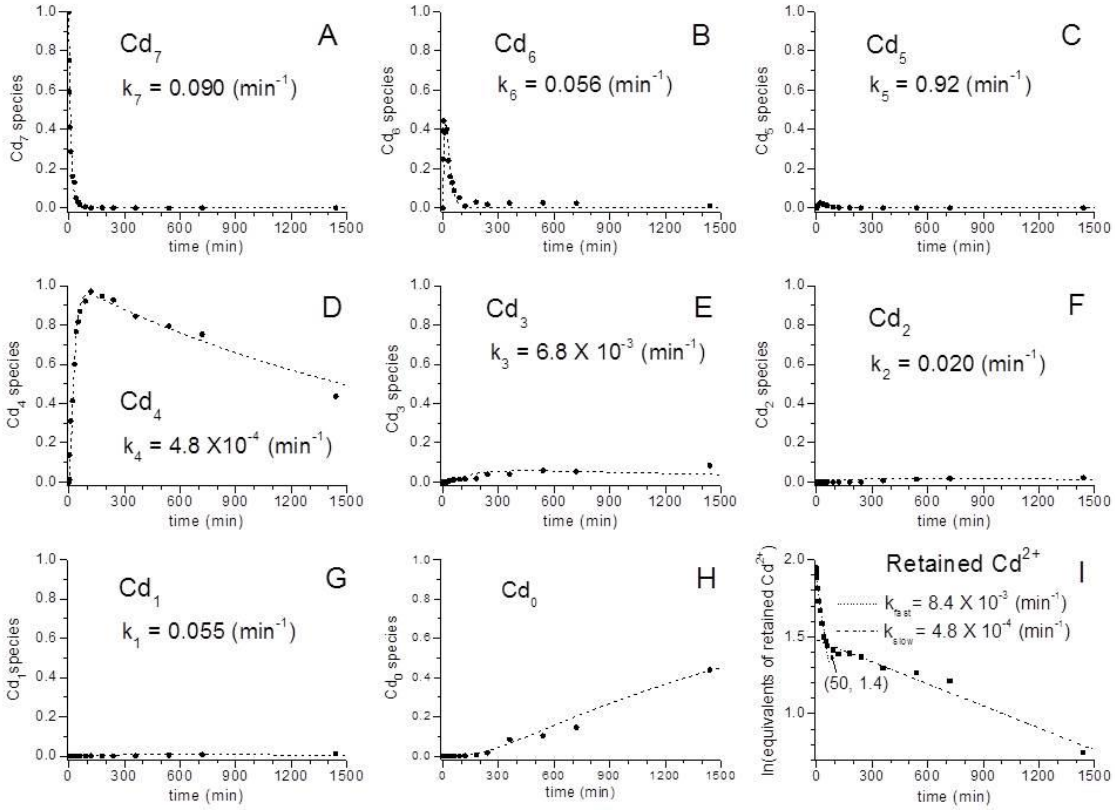

Figure 3.4. Kinetic plots for individual Cd_i species. 200 molar equiv of NEM was added to Cd_7MT and the reaction was continuously monitored by ESI-MS over 24 h. The ion signals for each Cd_i species containing different numbers of NEM (x), Cd_iNEM_x, are summed together to provide a total abundance of Cd_i species. The data points show the relative abundance for the Cd_i species and dashed lines are fitting curves. The rate constants are obtained by fitting equations of seven consecutive reactions.

The fitting of individual intermediates revealed a two-step displacement pattern and four classes of reaction rates that differ by greater than 3 orders of magnitude: (i) 10^{-4} min^{-1}: k_4; (ii) 10^{-3} min^{-1}: k_3; (iii) 10^{-2} min^{-1}: k_2 , k_1 , k_6 , k_7; (iv) 10^{-1} min^{-1}: k_5. For displacement of the metal ions in the β domain ($Cd_7 – Cd_4$), the rates of dissociation of the first and second metal ions (k_7 and k_6) are moderate (10^{-2} min^{-1}), while the third metal ion is lost much faster (16 times; k_5: 0.92 min^{-1}; **Figure 3.4C**). A similar kinetic pattern was observed for the displacement of metal ions in the α domain ($Cd_4 – Cd_0$). The metal displacement of Cd_4 species was very slow (k_4: 4.8×10^{-4} min^{-1}; **Figure 3.4D**), while the rates of loss of the remaining three Cd^{2+} were much faster (14 times for the fifth metal ion, k_3: 0.0068 min^{-1}, **Figure 3.4E**; 41 times for the sixth metal ion, k_2: 0.020 min^{-1}, **Figure 3.4F;** and 115 times for the seventh metal ion, k_1**:** 0.055 min^{-1}, **Figure 3.4G**).

The kinetic plots for the individual species reveal distinct stabilities of these intermediates that differ by > 3 orders of magnitude: stability order: $Cd_4 >> Cd_3 > Cd_2 > Cd_1 \sim Cd_6 > Cd_7 > Cd_5$. We concluded this data as follows: (i) the overall dissociation rate of metal ions from the α-domain (k_4–k_1) are much slower than that in the β-domain (k_7–k_5), indicating stronger metal-thiolate coordination and greater kinetic stability of the α-domain, consistent with previous results;[37] (ii) the well-known two-step kinetic profile of metal removal rate[81-82,132] of MT is attributed to the rate-determining steps for the α-domain (Cd_4 = 0.00048 min^{-1}) and β-domain (Cd_6 = 0.056 min^{-1}); however, the slight difference between k_7 (0.090 min^{-1}) and k_6 (0.056 min^{-1}) are difficult to probe by other methods; (iii) the release of first metal k_7 is faster than k_6, suggesting that there is a

weakly bound metal in the β-domain, which is consistent with a previous report;[133] (iv) the existence of a weak metal binding site in the α-domain was also indicated by the alkylation on Cys^{33} in the presence of a large excess of NEM (**Figure 3.2**). In addition, this NEM labeling on Cys^{33} suggests that the binding strength of the four cysteinyl ligands to a single Cd^{2+} is not equal. The relatively high stability of $Cd_4NEM_{10}MT$ implies that the alkylation on Cys^{33} does not lead to cooperative collapse of the α-domain, which suggests less contribution of the Cys^{33}–Cd^{2+} coordination in the overall stability of the α-domain.

Cooperativity

Vasak, Petering, Winge and Hunziker have suggested that Cd^{2+} binding to MT is cooperative.[81,107,126,134] The evidence is the observation of preferential formation of an intermediate associated with both metalation/demetalation processes, *viz.* Cd_4MT. More recently, however, Stillman and coworkers proposed non-cooperative binding based on the observation of a sequential, independent metal binding manner in the metalation process.[120] Thus, whether the metalation/demetalation process is cooperative or non-cooperative remains controversial. The kinetic plots contained in **Figure 3.4** suggest of Cd_i species in the metal-displacement experiment follow a cooperative loss of the metal ions for each of the domains: the rates of dissociation for the β-domain: $Cd_7 \sim Cd_6 < Cd_5$; α-domain: $Cd_4 < Cd_3 < Cd_2 < Cd_1$. These results suggest the binding mechanism for each of the domains is cooperative rather than independent. The preferential retention of metal ions in the α-domain also suggests a greater kinetic stability.

Effect of NEM labeling on conformation

The data contained in **Figure 3.2** suggests the Cys^{33} is a weak metal binding site in the α-domain. Fenselau *et al.* has shown that Cys^{33} is one of the solvent-exposed sites and is selectively targeted by anti-cancer reagents,[93-94] presumably the Cys^{33} is the terminal ligand in the α-domain.[93] Huang *et al.* have also demonstrated that the mutant of Cys^{33} of monkey MT1 does not disrupt the structure of Cd_4Cys_{11} α-domain; presumably the Cys^{33} is the terminal ligand in the α-domain.[135]

To probe the role of Cys^{33} and the effect of convent binding on conformation further, IM-MS is used to follow the metal-displacement reaction by NEM. The CCS profiles contained in **Figure 3.5** suggested Cd_4NEM_9MT exhibits similar conformation to $Cd_4NEM_{10}MT$, indicating that the additional NEM label on Cys^{33} does not disturb overall molecular shape, in line with the previous study.[135] However, it is somehow surprised that the compact conformation is retained through the metal displacement reaction *viz.* the NEM-labelled species including reaction intermediates (Cd_4NEM_9MT and $Cd_4NEM_{10}MT$) and final product ($NEM_{20}MT$) are composed of a single ordered ion population (right panel, **Figure 3.5**). In contrast, the demetalation of Cd_7MT by EDTA results in a significant conformational change that is from order-to-disorder and compact-to-extended; that is, the fully metalated Cd_7MT is composed of an ion population that is ordered and compact while the conformational diversity/flexibility is much greater when the metal ions are removed (left panel, **Figure 3.5**).

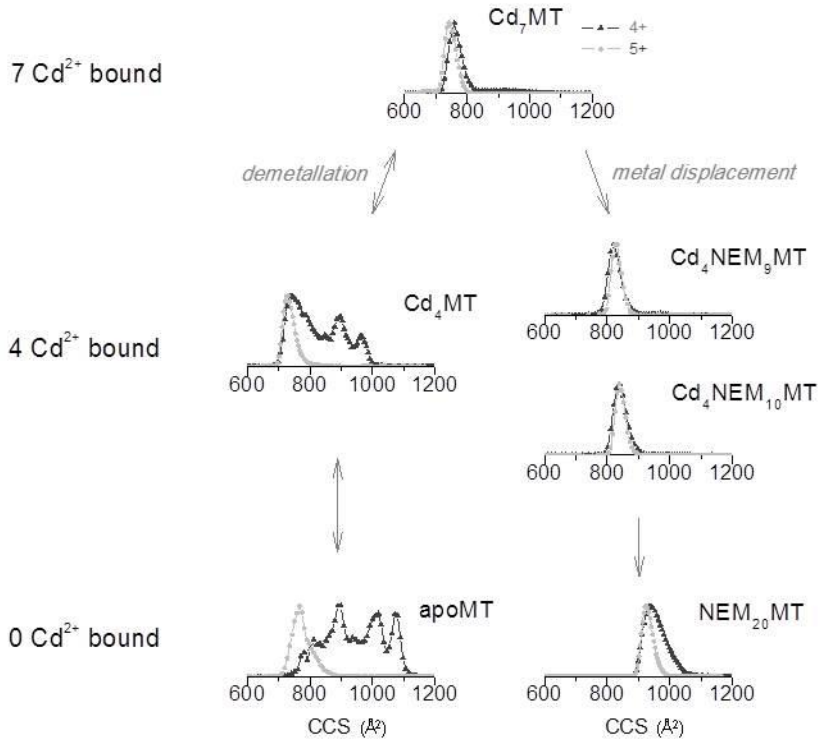

Figure 3.5. Ion mobility data for the fully-metalated Cd_7MT and the reaction intermediates and products in demetalation and metal displacement reactions. The data show distinct conformational transitions where metal displacement yields compact, order conformations while metal removal induces a disordered conformational population ranging from extended to compact conformers.

The data described above clearly show that the demetalation and metal displacement reactions yield products that are very different in terms of the structural populations, even when the number of metal ions bound is identical. The contrast between the two reactions raises an interesting question: *how does NEM maintain the compact conformation of MT?* That is, the removal of metal ions and metal-thiolate interaction can lead to protein unfolding but the intramolecular interaction between the protein segments appear to be retained by the addition of NEM. To understand the

conformation preference and intramolecular interaction of the reaction products, MD simulations were performed to generate gas phase-, solution-, and dehydrated structures.[65]

The MD data contained in **Figure 3.6** assume a stable conformation for Cd_7MT over the 20ns time window whereas that of the demetalated products Cd_4MT and apoMT fluctuate significantly between open and close states, suggesting that the removal of metal-thiolate interaction results in an ion population that is largely disordered, consistent to our ion mobility results (**Figure 3.5**) and solution studies.[9] On the other hand, the simulation data suggest a narrow conformational population for the metal displaced products $Cd_4NEM_{10}MT$ and $NEM_{20}MT$, suggesting that intramolecular interaction are retained after the replacement of metal ion by NEM. To identify the type of interaction that holds the structures of the NEM-labelled proteins compact, the MD trajectories were further analyzed. **Table 3.1** summarizes the results of hydrogen bond analysis of these four reaction products that shows the NEM-labelled Cd_iMTs contain a greater number of hydrogen bond compared to that of Cd_iMT. In addition, the frequency of hydrogen bond, which provides information for the bond stability, is also higher for the NEM-labelled Cd_iMTs. The data suggest the 3-D conformation of the NEM-displaced Cd_iMTs is partly locked into place by hydrogen bonds that are introduced by NEMs.

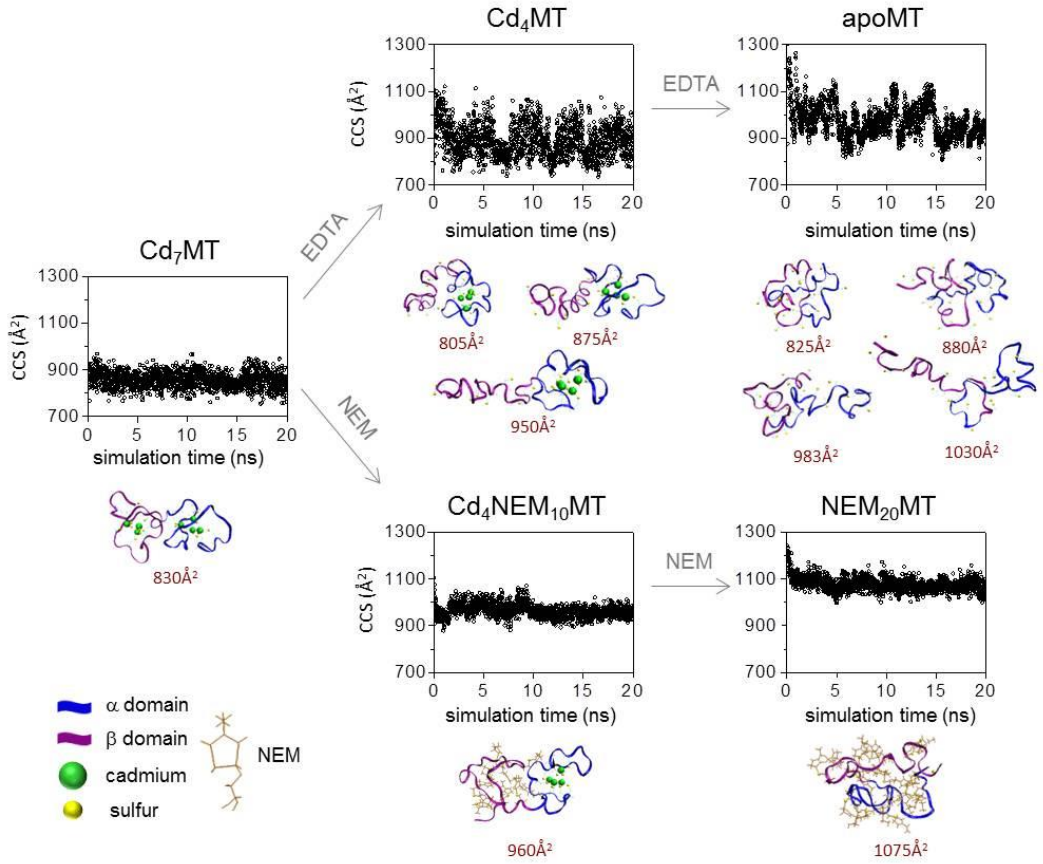

Figure 3.6. MD simulations and representative conformations of dehydrated Cd_7MT and the demtallation products Cd_4MT and apoMT (top panel) and metal displacement products $Cd_4NEM_{10}MT$ and $NEM_{20}MT$. The data suggest the conformations of apoMT and Cd_4MT vary significantly in time (disordered conformation) whereas the conformations of Cd_7MT, $Cd_4NEM_{10}MT$, and $NEM_{20}MT$ are relatively stable and adopt globular–like conformation (ordered conformation).

	DONOR	ACCEPTOR:H	ACCEPTOR	%occupied	distance (Å)
	atom# :res@atom	atom# :res@atom	atom# :res@atom		
apoMT	119 :10@O	165 :14@HG1	164 :14@OG1	18.97	2.969
	287 :23@O	354 :28@HG	353 :28@OG	11.77	3.179
Cd_4MT	770 :61@O	549 :43@HZ2	547 :43@NZ	18.79	3.017
	770 :61@O	550 :43@HZ3	547 :43@NZ	18.54	3.006
	770 :61@O	548 :43@HZ1	547 :43@NZ	18.04	3.013
	771 :61@OXT	549 :43@HZ2	547 :43@NZ	15.67	3.049
	771 :61@OXT	550 :43@HZ3	547 :43@NZ	14.97	3.074
	771 :61@OXT	548 :43@HZ1	547 :43@NZ	14.78	3.059
	285 :23@OE2	237 :20@HZ3	234 :20@NZ	12.18	2.964
	284 :23@OE1	237 :20@HZ3	234 :20@NZ	11.37	2.994
	285 :23@OE2	236 :20@HZ2	234 :20@NZ	10.67	2.97
	694 :55@OD1	717 :56@HZ3	714 :56@NZ	10.43	3.017
$NEM_{20}MT$	368 :22@O	471 :27@HG1	470 :27@OG1	42.35	3.316
	97 :6@O	213 :14@HG1	212 :14@OG1	39.85	3.369
	151 :10@O	213 :14@HG1	212 :14@OG1	30.8	3.503
	346 :21@O	471 :27@HG1	470 :27@OG1	30.45	3.165
	201 :13@O	213 :14@HG1	212 :14@OG1	28.25	3.321
	1101 :61@O	997 :56@HZ3	994 :56@NZ	21.2	3.009
	685 :37@O	564 :32@HG	563 :32@OG	20.25	3.296
	31 :2@O	57 :4@HD22	55 :4@ND2	18.9	3.043
	1102 :61@OXT	995 :56@HZ1	994 :56@NZ	18.55	3.018
	1102 :61@OXT	997 :56@HZ3	994 :56@NZ	18.4	3.057
	1101 :61@O	995 :56@HZ1	994 :56@NZ	17.9	3.06
	1101 :61@O	996 :56@HZ2	994 :56@NZ	17.3	2.995
	1102 :61@OXT	996 :56@HZ2	994 :56@NZ	14.25	3.03
	1101 :61@O	56 :4@HD21	55 :4@ND2	10.1	3.12
$Cd_4NEM_{10}MT$	368 :22@O	95 :6@HG	94 :6@OG	73.9	3.113
	634 :37@O	564 :32@HG	563 :32@OG	41.3	3.378
	29 :2@OD2	57 :4@HD22	55 :4@ND2	33	3
	380 :23@OE1	213 :14@HG1	212 :14@OG1	30.8	3.107
	648 :38@O	564 :32@HG	563 :32@OG	29.15	3.125
	381 :23@OE2	213 :14@HG1	212 :14@OG1	27.35	3.166
	28 :2@OD1	57 :4@HD22	55 :4@ND2	26.05	3.104
	932 :61@OXT	711 :43@HZ3	708 :43@NZ	21.1	3.003
	932 :61@OXT	710 :43@HZ2	708 :43@NZ	20.9	3.021
	932 :61@OXT	709 :43@HZ1	708 :43@NZ	20.85	2.981
	931 :61@O	710 :43@HZ2	708 :43@NZ	20.4	3.011
	931 :61@O	709 :43@HZ1	708 :43@NZ	19.65	3.02
	931 :61@O	711 :43@HZ3	708 :43@NZ	18.4	3.039
	45 :3@O	429 :25@HZ2	427 :25@NZ	16.55	3.096
	496 :29@OD	56 :4@HD21	55 :4@ND2	16.1	3.104
	45 :3@O	430 :25@HZ3	427 :25@NZ	16	3.11
	45 :3@O	428 :25@HZ1	427 :25@NZ	14.65	3.089
	259 :17@O	747 :46@HE21	746 :46@NE2	10.05	3.164

Table 3.1. Hydrogen bond analysis for simulated solution structures of the demetalation (Cd_4MT and apoMT) and metal-displaced ($Cd_4NEM_{10}MT$ and $NEM_{20}MT$) products over a 20-ns MD simulation time window. The data suggest metal-displaced products exhibit greater number of hydrogen bonds than that of demetalated products.

Conclusion

The mechanism of metal-displacement of cadmium binding human metallothionein-2A (Cd_7MT) is investigated by electrospray ionization ion mobility mass spectrometry and molecular dynamics simulations. Metal-displacement reveals distinct kinetic stabilities of the various intermediates that differ by > 3 orders of magnitude in kinetic rate constants. Directly sequencing of a kinetic intermediate $[Cd_4NEM_{10}MT]^{5+}$ by "MS-CID-IM-MS" suggest that the metal-displacement occurs in the β domain before the α domain, a reverse direction to the metalation,[127] suggesting a greater kinetic stability for the α-domain. The two-step metal-displacement kinetic profile suggests a cooperative binding of three Cd^{2+} ions in the β-domain followed by the remaining four Cd^{2+} ions in the α-domain. The MS-CID-IM-MS data also suggests that Cys^{33} is a weak binding site in the α domain, and labeling of Cys^{33} does not lead to collapse of the metal-thiolate cluster. On the other hand, IM-MS data show distinct conformational changes between metal removal and metal displacement reactions: metal removal by EDTA induces a disordered conformation population ranging from compact to extended conformation whereas the metal-displacement by NEM yields globular-like compact conformation. We interpreted this data as an evidence of lose of its disordered characteristics and formation of ordered and globular-like conformations. Independent MD simulations on the demetalated and metal-displaced products show distinct reaction pathways, consistent to our IM-MS results. A disordered conformational population was observed after metal ions are removed but metal displacement by NEM yields a compact conformation due to formation of hydrogen bonds.

CHAPTER IV

METAL-INDUCED CONFORMATIONAL CHANGES OF HUMAN METALLOTHIONEIN: A COMBINED THEORETICAL AND EXPERIMENTAL STUDY OF METAL-FREE AND PARTIALLY-METALATED INTERMEDIATES

Introduction

One-third of proteins naturally bind metal ions in order to provide activity and/or stability.[136] Aberrant metalation has been linked to protein misfolding and human disease, specifically pathogenic processes of amyloidosis, including Aβ-peptide aggregation in Alzeheimer's diseases (AD), α-synuclein in Parkinson's disease (PD), and prion protein in transmissible spongiform encephalopathies (TSE).[137] There is increasing evidence that Cu^{2+} ions disrupt Aβ-peptide from adapting a β-sheet conformation,[138-139] and Cu^{2+} and Fe^{3+} ions trigger structural transformation as well as increase in fibrillation rate of α-synuclein.[140] Similarly, Zn^{2+} and Cu^{2+} ions alter prion protein aggregation pathways and formation of amorphous aggregates instead of fibrils.[141] Not surprisingly, however, metal-protein interactions also have potential as

---

*Reprinted with permission from Chen, S.-H.; Chen, L.; and Russell, D. H. Metal-Induced Conformational Changes of Human Metallothionein-2A: A Combined Theoretical and Experimental Study of Metal-Free and Partially Metalated Intermediates *J. Am. Chem. Soc.* **2014**, *136*, 9499 – 9508. Copyright (2014) by American Chemical Society

therapeutic agents. For example, Mg^{2+} inhibits α-synuclein aggregation,[142] and binding of Zn^{2+} to Aβ-peptide reduces cytotoxicity.[143] Metallothioneins (MTs), a class of metalloproteins, are known as one of the most important *in vivo* metal reservoirs and transporters.[1,144] MTs are cysteine-rich and possess diverse metal binding preferences that serve to regulate essential metal ions and as protection against toxicity of non-essential metal ions.[8-9] It is becoming increasingly evident that MTs play protective roles in neurodegenerative diseases by buffering free zinc in amyotrophic lateral sclerosis (ALS)[145] and reducing copper toxicity and production of reactive oxygen species (ROS) in AD.[14-15] MTs are also free-radical scavengers and protect against nephrotoxicity from Cd^{2+} exposure.[8,146] In addition, MTs have been found substantially unsaturated with metal ions in many tumors,[23] and recent evidence suggests that the metal-unsaturated MTs are biologically active in terms of cellular metal metabolism and redox balance.[24-25] Despite the roles of MTs in various diseases, underlying mechanisms regarding the role of metal ions in promoting protein conformational changes as well as influencing subsequent chemical/biological pathways are poorly understood.

It is generally accepted that structures of MTs are determined by the number and type of metal ions they coordinate.[9] Structure determination of MTs has proved to be a real challenge owing to their dynamical conformations that makes crystallization difficult, impossible in most cases.[9] A major step forward in understanding the chemical/biological properties of MTs was determining the atomic-level structure of fully-metalated MTs by integrating structural information from an X-ray crystal structure (rat MT-2A) by Stout *et al.*[34] and NMR structures (rat, rabbit, and human MT-

2A) by Wüthrich *et al*.[35-37] They assigned a dumbbell-shaped three-dimensional structure to human Cd_7MT-2A protein comprising two distinct metal binding domains denoted as $Cd_3\beta$- and $Cd_4\alpha$-domains.[37,147] Despite the success in structure determination of fully-metalated MTs, there is increasing evidence that apo- and partially-metalated species are physiologically abundant and may also have important biological roles.[24-25] However, further structural characterization of these metal-unsaturated species has encountered a bottleneck. Blindauer noted that apo- and partially metalated MTs are likely to be unfolded to some degree, thus not amenable to traditional structural studies such as X-ray crystallography.[9] In addition, many biophysical techniques commonly used for characterization of protein conformation are limited to well-defined systems, *i.e.*, solutions of pure protein or high quality crystals. Unfortunately, dynamic equilibria between apo- and partially-metalated forms present a significant challenge in terms of isolation of individual metalated states from a complex protein pool. Previous mass spectrometry studies have shown that more than six metalation states of Cd_iMT (or Zn_iMT; i = 0 – 7) co-exist in solution,[47,107,122,127] and multiple structural conformers for each metalated state adds an additional layer of complexity. Because traditional biophysical techniques measure the average response for the entire system, it is difficult or even impossible to resolve signals derived from a single conformer in the presence of other closely related conformers from a single metalated state, let alone in the presence of multiple metalated states. In addition, attempts at elucidating structural transitions associated with metal binding by circular dichroism (CD) and optical methods such as UV/Vis and fluorescence are generally ineffective because mammalian MTs lack well-

defined secondary structure and they do not contain aromatic amino acids.[9] FRET analysis utilizing labeling at two-termini provides information for change of distance between the two sensors,[148-150] and dynamic light scattering[151] and small-angle X-ray scattering (SAXS) provide information about particle size distribution. However, such studies also measure the population-averaged response and do not provide molecule-specific information, which limits the information content to the comparisons between metal-free and fully-metalated states. Therefore for nearly six decades of MT research, the only 3-D molecular characterization technique for studies of apo- and partially-metalated species has been molecular modeling[9] and comparable experimental evidence has been lacking. Consequently, questions concerning the conformational micro-heterogeneity of the apo- and partially metalated species or how the distribution of conformations changes as a result of metal accumulation remain unanswered and the metalation mechanism remains unclear.

Fenselau and coworkers pioneered the application of electrospray mass spectrometry (ESI MS) on studies of MTs.[46-47,91,93-94] ESI MS is now increasingly used for studies of complex biological samples; especially, there is increasing evidence that under well-controlled conditions native-like conformations of proteins can be retained during the ESI process.[66,152-153] In our previous study, a combination of chemical labeling and top-down and bottom-up proteomic ESI-MS provided valuable new insights into the metalation/demetalation of the human metallothionein MT-2A.[127] The study revealed that: (1) metalation of MT by Cd^{2+} occurs by a stepwise mechanism as originally suggested by Winge;[126] (2) partially-metalated Cd_4MT is a relatively stable

intermediate as supported by a sharp increase in stepwise apparent association constant; and (3) all Cd^{2+} ions are located in the α domain for Cd_4MT.[127] Although the study provided a new level of understanding of the metalation mechanism and new experimental approaches for probing apparent association constant and location of metal ion bound, structures of the metalated species remain unclear.

Ion mobility mass spectrometry (IM-MS) has emerged as a promising approach for characterization of protein conformation, and Guo *et al*. have reported IM-MS results for apo- and fully-metalated Cd_7MT.[154] Here, IM-MS is employed to investigate stepwise conformational changes of human MT-2A as a function of the number of Cd^{2+} ions bound. IM-MS provides an unparalleled approach for monitoring all the distinct MT conformers owing to its unique capabilities of (1) separation of the multiple metalated states, *i.e.*, the initial apo-protein, intermediates inherent to the metalation reactions, and the final products, by their characteristic m/z ratios by mass spectrometry, and (2) interrogation of the conformer population for individual metalation state by ion mobility spectrometry. Molecular dynamics (MD) simulations are used to generate protein conformations whose collision cross section (CCS) can be correlated to the experimental IM-MS CCS. We show here the first experimental data for conformational population of each of the metalated forms. The integrated IM-MS and MD approach offers a global view of the conformational changes that occur upon metal binding and provide new insights into the metalation mechanism.

Experimental

Materials

Recombinant human metal-free MT-2A (apoMT) was obtained from Bestenbalt LLC (Tallinn, Estonia). Cadmium acetate and ammonium acetate were purchased from Sigma-Aldrich (St. Louis, MO). Tris(2-carboxyethyl)phosphine hydrochloride (TCEP-HCl) was obtained from Thermo Fisher Scientific (Rockford, IL). Deionized water (18.2 MΩ) was obtained from a Milli-Q water apparatus (Millipore, Billerica, MA).

Sample preparation

ApoMT powder samples were prepared and stored using previously described procedures.[127] The sample was then reconstituted to 7 μM by 50 mM ammonium acetate (pH 7.4) solution containing 1 mM TCEP. ApoMT is prone to oxidation at physiological pH under aerobic conditions, thus TCEP was added to maintain the cysteinyl thiols in the active reduced states. The metalation experiment was performed by sequential addition of 2, 4, and 6 μL of 1 mM cadmium acetate solution to 100 μL of a 7 μM apoMT solution. Following each addition of the Cd^{2+} solution, the protein was allowed to incubate for 1 h prior to MS measurements. Care was taken in all ESI-IM-MS experiments reported here to exclude ESI-induced protein oxidation and non-specific metal binding as previously described.[127]

Ion-mobility-mass spectrometry

ESI IM-MS measurements were performed on a Waters Synapt G2 HDMS instrument (Manchester, UK), a hybrid quadrupole/ion mobility (IM)/orthogonal time-of-flight mass spectrometer. The samples were analyzed as follows: 7 μM MT solutions

were directly infused into the mass spectrometer at a 0.5 μL/min flow rate. ESI spectra were collected in the positive ion mode with a capillary voltage of 1.0 – 1.5 kV, sample cone voltage of 10 V, and extraction cone voltage of 1 V. The helium cell and nitrogen traveling wave (TW) regions were operated at 180 and 60 mL/min flows, respectively. A TW velocity of 300 m/s and TW height of 20 V was used for all the experiments unless specified otherwise. All mass spectra were calibrated externally using a solution of sodium iodide. CCS data were calibrated using ubiquitin, cytochrome C, and myoglobin as previously described.[128] Abundances of Cd_iMT^{n+} were determined by performing a baseline correction and calculating the area under the peaks. We also evaluated the effect of salt adducts by including salt adducts into the total abundance of Cd_iMT^{n+}. Since the salt adducts are present in all charge states detected, no significant difference was observed in the charge state distributions.

Ion arrival time distribution (ATD) can be very sensitive to experimental parameters, especially experimental conditions that may alter the effective ion temperature (T_{eff}),[155-157] and this is especially apparent for apoMT and the partially metalated ions. To illustrate this point, ATD for $apoMT^{5+}$ and Cd_7MT^{5+} are shown in **Figure 4.1**. Note that the CCS profiles differ significantly using conditions that increase T_{eff}. Specifically, peaks corresponding to larger CCS peaks are observed in **Figure 4.1 A and C**, but these peaks are attenuated or absent in data taken under conditions that minimize ion heating. All the IM-MS data reported herein were obtained under conditions where nitrogen gas flow and the voltages applied to the sample cone,

extraction cone, and trap bias were adjusted to minimize ion heating, specifically instrument conditions that yield ATDs as shown in **Figure 4.1 B** and **D**.

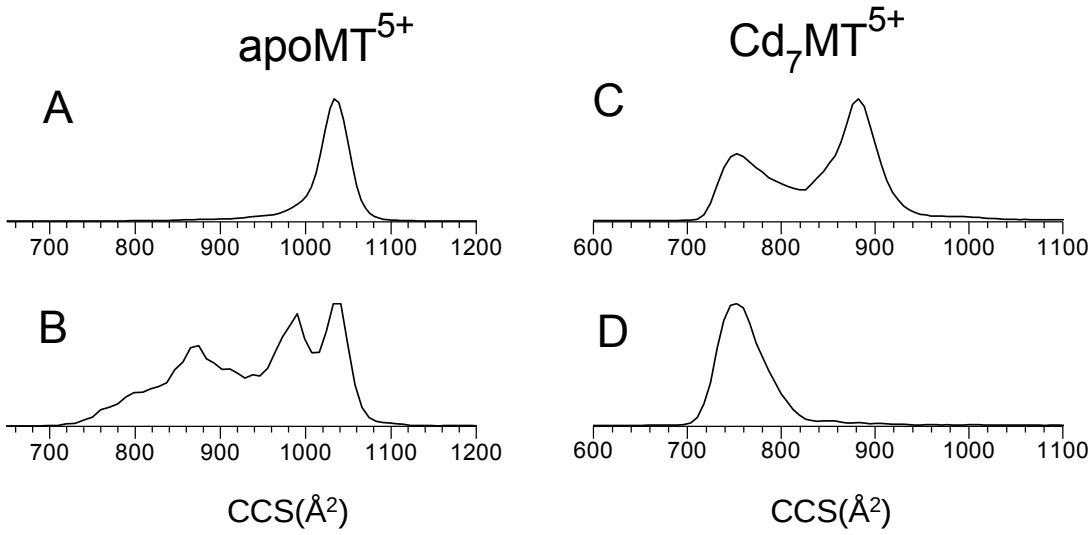

Figure 4.1. ATDs for apoMT^{5+} (A, B) and Cd_7MT^{5+} (C, D) acquired under different instrumental settings. Condition A and C are referred by manufacturer's suggestion: sampling cone 60 V and extraction cone 4 V, IMS gas flow: 90 mL/min and trap bias 45 V. Condition B and D are operated under a much gentler setting: sampling cone 10 V and extraction cone 1 V, IMS gas flow: 60 mL/min voltage and trap bias 35 V.

MD simulations

Due to unavailability of the structure(s) for intact human MT-2A, structures from NMR of the separate domains[37] were connected (PDB: 1MHU and 2MHU) using a trans configuration (backbone dihedral angle $\omega \sim 180°$) between the two connecting lysines (Lys30-Lys31) as the starting structure for MD simulations of fully metalated Cd_7MT. Structures for partially metalated Cd_iMTs ($i = 1 - 6$) were generated by placing the Cd^{2+}

ions in specific bonding sites as indicated in **Figure 4.2**, which contains the amino acid sequence of MT and the numbering scheme of Cd^{2+} assigned by NMR experiments.[37] Charges on the hydrophilic amino acid side chains, *viz.* the ε-amino groups of the lysines and the carboxylic acid side chain of aspartic acid and glutamic acid were assigned assuming a pH of 7. That is, cadmium ion is 2+, cadmium coordinated deprotonated cysteine is -1, lysine is +1, aspartic and glutamic acids are -1, and free cysteine and other amino acids are neutral. We note that there may be other possible Cd^{2+} configurations for the partially metalated forms. For example, Cd^{2+} may bind cysteines different from those designated in **Figure 4.2**. In addition, the coordination number may not be equal to 4 as preferred Cd^{2+} coordination can be either tetrahedral or octahedral.[104] For example, Cd^{2+} ions are octahedrally coordinated in carp parvalbumin, concanavalin A, thermolysin and troponin C.[104] However, it is not clear how these variables should be treated because the structure, coordination number and site occupancy for partially-metalated MTs have not been determined experimentally; therefore, the simulations are limited to previously reported Cd^{2+}-S bonding configurations in human Cd_7MT (**Figure 4.2**).

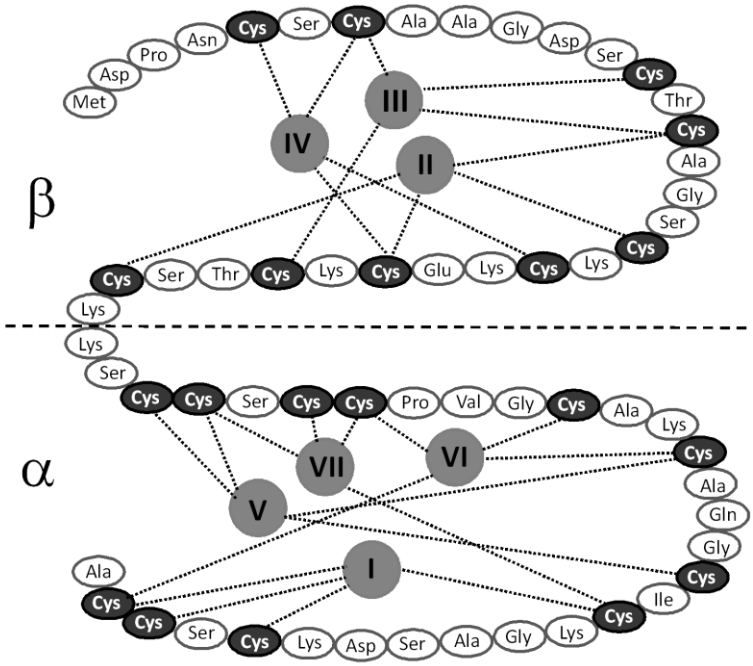

Figure 4.2. Sequence of human MT-2A and its metal-sulfur connectivities. The dotted lines denote the Cd^{2+}–Cys coordination. The Cd^{2+} ions are labeled I – VII using the cadmium-thiolate coordination derived from NMR studies.[37] The dashed line, α, and β denote the boundaries and locations of the two domains.

All-atom MD simulations were performed using AMBER 9.0 FF99SB force field, which is extended to include parameters for cadmium–thiolate clusters (parameter B2; **Table 4.1**).[158] Solution phase structures were simulated by using a modified generalized Born implicit solvent model (igb =5)[159] to represent an aqueous solution environment. The initial structures were energy-minimized, followed by simulations at 300 K *in vacuo* (solvent-free) or implicit solvent model for 25 or 50 ns. "Dehydrated structures" were generated from solution phase structures by using *in vacuo* energy minimization.[45,59,66,160] CCS calculations were carried out using a trajectory method implemented in MOBCAL,[131] in which the atomic energy and van der Waals radius of

Cu^{2+} were used for Cd^{2+}. A complete description for MD simulations and data analysis is provided in Appendix. Distribution of CCS for each simulation model is represented by a histogram with a 10 $Å^2$ interval. The simulated structures were clustered into families using a Cα root mean square deviations (RMSD)-based clustering algorithm in MMTSB tool set.[161] Representative structures, determined as those closer to the centroid of each cluster, were selected to represent the candidate experimental structures.

Model	Bonded			Nonbond			
Method	B1*		B2**	NB1***		NB2****	
BOND	k_b (kcal mol^{-1} Å^{-2})	r_0 (Å)					
Cd-St	127	2.532	same as B1				
Cd-Sb	254	2.596	same as B1				
ANGLE	k_θ (kcal mol^{-1} rad^{-2})	θ (degree)					
C-S-Cs	46	116.3	same as B1				
S-Cd-S	92	109.5	same as B1				
Cd-S-Cd	92	120.0	same as B1				
Lennard-Jones	σ (Å)	ε (kcal mol^{-1})		σ (Å)	ε (kcal mol^{-1})	σ (Å)	ε (kcal mol^{-1})
Cd	2.48	0.0125	same as B1	2.48	0.25	2.395	0.0395
S	3.92	0.47	same as B1	4.02	0.92	3.92	0.47
Charge							
Cd(α)	1.285		2.00	2.00		1.21	
Cd(β)	1.220		2.00	2.00		1.21	
St	-0.72		-0.8844	-0.8844		-0.6869	
Sb	-0.72		-0.8844	-0.8844		-0.4894	
C	-0.02		-0.2413	-0.2413		-0.2413	
H	0.00		0.1122	0.1122		0.1122	

*references: (1) PROTEINS: Structure, Function, and Bioinformatics 2007, 68, 255–266
(2) International Journal of Quantum Chemistry, 2001, 83, 230–244
** formal charge from Amber force field
*** reference: International Journal of Quantum Chemistry, 2001, 83, 230–244
**** reference: J Comput Chem 2009, 30, 191–202

Table 4.1. Four candidate force field parameters for Cd^{2+} ions of Cd_7MT. NB1 and NB2 refer to two nonbonded models and B1 and B2 are two bonded models. k_b, r_0, k_θ, θ, ε, and σ denote bond energy, bond distance, angle force constant**,** bond angle, atomic energy, and van der Waals distance, respectively.

Results

The mechanism of metalation of human MT-2A by Cd^{2+} was previously studied by ESI-MS.[127] The ESI mass spectrum of apoMT contains abundant $apoMT^{n+}$ ions that range from n = 3 – 6, but the most abundant ion signals correspond to n = 4 and 5. Addition of aliquots of cadmium acetate solution to a solution of apoMT results in stepwise addition of Cd^{2+} to form Cd_iMT, where i ranges from 0 – 7 (**Figure 4.3A**).[127] A general concern with ESI-MS-based metal-binding studies is the possible occurrence of nonspecific interactions. The data indicates that nonspecific Cd^{2+} association is negligible. Cd^{2+} was shown to bind only to MT as the concentration of Cd^{2+} increases, and not to the non-MT species (impurities present in the original sample) that served as reference proteins (see Chapter II, **Figure 2.4**).

The ESI charge state distribution of the Cd_iMT ions shows a dependence on the numbers of metal ions (**Figure 4.3B)**, and such changes in charge state distribution could be linked to changes in solution phase conformations that alter the solvent accessible surface area (*vide infra*).[162-163] As the number of metal ions increases, the abundances of low charge state ions (n = 3 and 4) increase whereas the abundances of high charge states ions (n = 5 and 6) decrease.

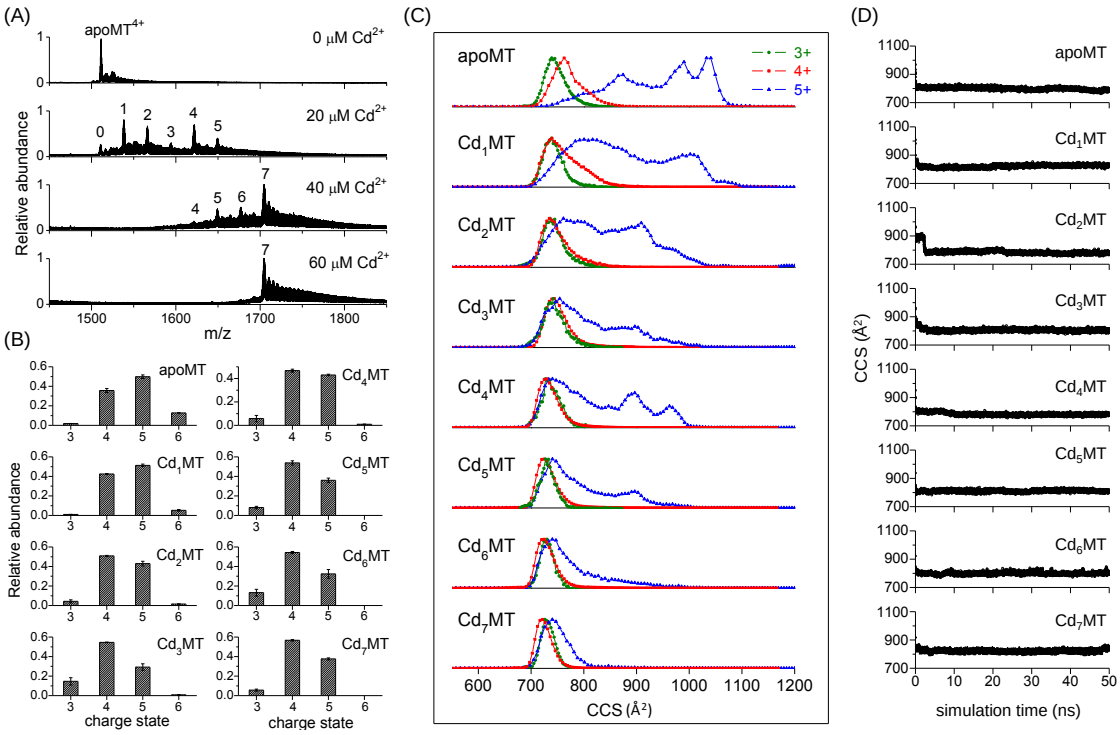

Figure 4.3. (A) ESI-MS spectra of a 7 μM apoMT solution (pH 7.4), and titration of apoMT with 20, 40, and 60 μM Cd^{2+}. Numbers above peaks denote the metal stoichiometry of the Cd_iMT species (i = 0−7). Data is shown for m/z range of 4^+ ions only. Additional peaks at +23 Da (*) and +60 Da ($^{\times}$) correspond to sodium and acetate adducts. (B) Charge state distributions of Cd_iMT (i = 0 – 7). Relative abundances were determined by the areas under the peaks after a baseline correction. (C) Overlay of CCS distributions of Cd_iMT as a function of metal accumulation. Three charge states observed from native electrospray ionization (50 mM ammonium acetate with 1 mM TCEP at pH 7.4) are shown in green (3+), red (4+), and blue (5+). Note all the CCS data were obtained using ion source and ion transfer conditions that minimize collisional heating, which maximizes the preservation of native solution structures. We also note that dimeric forms of fully metalated MT species (Cd_5Zn_2MT, Cd_7MT, and Zn_7MT) have been reported. Although low abundant dimer ions of partially and fully metalated forms (i = 1 – 7) were observed (6^+ dimer ions, see Figure 4.4) under the experimental conditions used for this study, the discussion will be limited to the monomeric species. (D) Representative *in vacuo* MD simulations of Cd_iMT (i = 0 – 7). We have considered all possible metal ion binding configurations (or metal ion distribution) for each of the partially-metalated forms (i = 1 – 6) except the case of i =4. Data presented here represent one particular configuration with consecutively placing the metal ions into the binding pockets using this order: I → V → VII → VI → II → III → IV, the reverse demetalation order proposed by the Stillman group.

IM-MS provides a direct approach for monitoring the products of reaction (speciation) as well as conformational changes that occur upon addition of Cd^{2+} ions. Ion mobility CCS data for the Cd_iMT species are shown in **Figure 4.3C**; ATD data are shown in **Figure 4.4**. The CCS profiles for each of the charge states of apoMT span a wide range, *viz.* the 3^+ and 4^+ ions range from ~ 700 to ~ 800 $Å^2$ and 5^+ ions range from ~ 730 to ~ 1100 $Å^2$ (**Figure 4.3C**, top). We note that the peak widths for apo and partially-metalated MT ions are substantially broad (drift time/peak width (DT/PW) ~ 5.5, 5.2, and 2.7 for $apoMT^{n+}$ (n = 3 – 5), respectively (see **Figure 4.4**). This is indicative of an ion population composed of a high degree of conformational heterogeneity. In general, the CCS profile for each charge state becomes narrower and shifts to lower CCS values as the number of metal ions increases (**Figure 4.3C**), indicating that addition of Cd^{2+} ions yields more compact, ordered conformations. The reduction in conformational diversity and disorder accompanying metal ion addition is most pronounced for the Cd_iMT^{5+} ions. Note that the addition of a single Cd^{2+} ion narrows the peak profile and shifts the CCSs to smaller values, and subsequent addition of Cd^{2+} ions further narrows the CCS profile. The CCS values show consistent decrease except for the case from i = 3 to 4, which will be discussed in the discussion section. In general, for $i \leq 4$, multiple distinct conformations coexist and the population shifts to the compact conformers; however, for $i > 4$, the peak profiles become progressively narrower and primarily populate compact conformations. Collectively, the charge state distributions and CCS data show that metalation promotes a reduction in conformational diversity and yields compact conformations.

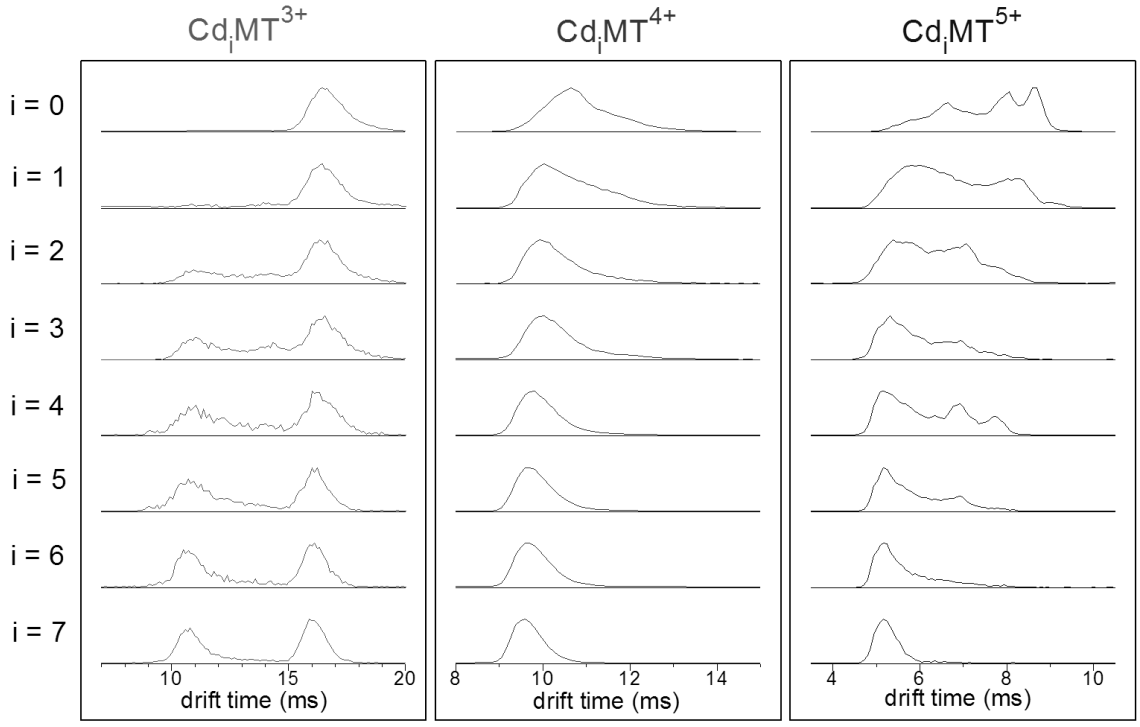

Figure 4.4. ATDs of Cd_iMT^{n+} as a function of the number of metal ion bound (i = 0 – 7) in three charge states (n = 3– 5). The population at drift time 10.7 ms for the 3^+ charge state is assigned as dimer of Cd_iMT as the CCS corresponds to 1155 Å^2, which corresponds to the CCS value of dimer ($2^{2/3}$ times to that of the monomer (730 Å^2)).[45] Although the dimeric forms of fully metalated MT species (Cd_5Zn_2MT, Cd_7MT, and Zn_7MT) have been reported, the additional information revealed in our data is that the formation of dimer ions is initiated upon metal ion addition to MT and the abundance of dimers increases as the number of metal ions bound increases.

In an effort to understand detailed molecular features of the conformers observed in the IM-MS experiments, *in vacuo* MD simulations that yield conformations for solvent-free, gas phase ions were performed. Independent of the number of metal ions added, the simulations of the candidate conformers have a relatively narrow CCS distribution centered at ~ 800 Å^2 (**Figure 4.3D**). Although the simulation data are in good agreement with that of the compact conformations (3^+ and 4^+ ions), the extended

conformations (5^+ ions) observed in the IM-MS experiments clearly show a more complicated metalation pathway (**Figure 4.3C**). Note that the features for these extended conformations remain undetected even when the temperature used for MD simulations is increased to 500 K (see **Figure 4.5**).

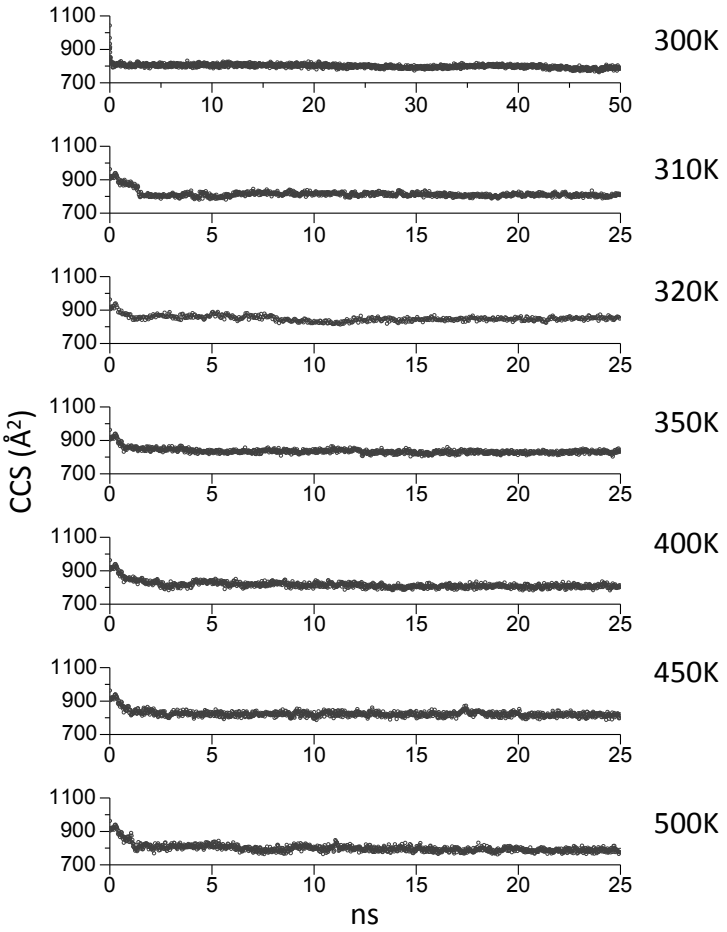

Figure 4.5. *In vacuo* MD simulations of apoMT at 300, 310, 320, 350, 400, 450, and 500 K. The simulations show that, despite the temperature, the conformation equilibrates toward compact conformations in a short time (< 1 ns).

Ion mobility sample ions that have experienced dramatic changes in their local environments, *i.e*. ions in solution, are ejected as micron size droplets which evaporate to yield nanometer size droplets; finally, evaporation of remnant water molecules yields solvent-free gas phase ions.[164] To aid in understanding the effects of desolvation on conformer preferences, simulations were carried out using implicit solvent (water) to yield solution phase conformations. In an effort to mimic the ESI conditions, the water was removed from the MD solution phase conformers followed by energy minimization *in vacuo* to yield what is referred to as "dehydrated" conformers (see **Figure 4.6A**). The differences between gas phase and dehydrated conformations are (1) whether the initial conformation is allowed to evolve in bulk water as opposed to a solvent-free environment, and (2) whether the energy of conformations are being reduced in the simulation process. The comparison of simulation data in *vacuo*, in water, and upon subsequent dehydration for apoMT is presented in **Figure 4.6B**. The *in vacuo* simulation shows that the initial conformer rapidly (within 0.1 ns, trajectory v1) assumes a compact conformation that does not change significantly over the 50 ns sampling time frame (trajectory v2 represents the equilibrated conformation). Conversely, sample ions obtained from implicit water simulations have CCSs that range from 900 – 1500 $Å^2$, suggesting a wide range of conformers and/or a highly disordered ion population. The labels w1 and w2 represent oscillations between extended and compact conformations and w3 represents a conformation having an intermediate size. "Dehydrated" conformations retain the general features of solution phase ions, but the CCS are somewhat smaller indicating that the conformers "shrink" *in vacuo* owing to the loss of

water (800 – 1300 $Å^2$).[59,160] The trajectories d1, d2, and d3 resemble the original solution conformers w1, w2, and w3, respectively, but the overall conformations are refined in vacuum. Skinner *et al*. and Silveira *et al*. recently reported on this phenomenon and showed that the "shrinkage" is the result of intramolecular charge solvation that occurs upon removal of the solvent.[164-165] This explanation is consistent with arguments that have been used previously to rationalize differences in experimental CCS and calculated CCS based on XRD crystal/NMR structures.[59,61] Histograms of the CCSs for the dehydrated conformations of apoMT with formal charges are summarized in **Figure 4.7** (panel A). Good agreement was obtained between the simulated conformational space (MD) and the range of conformer population (IM-MS). We note that effects of charge states for simulations of apoMT are small (data not shown). Simulations with manipulating charge states (protonation at Asp2, Asp11, Glu23, or Asp55) reveal similar structural fluctuation (open-close motions for solution phase and dehydrated structures) and similar conformational space for dehydrated structures (800 – 1300 $Å^2$, data not shown).

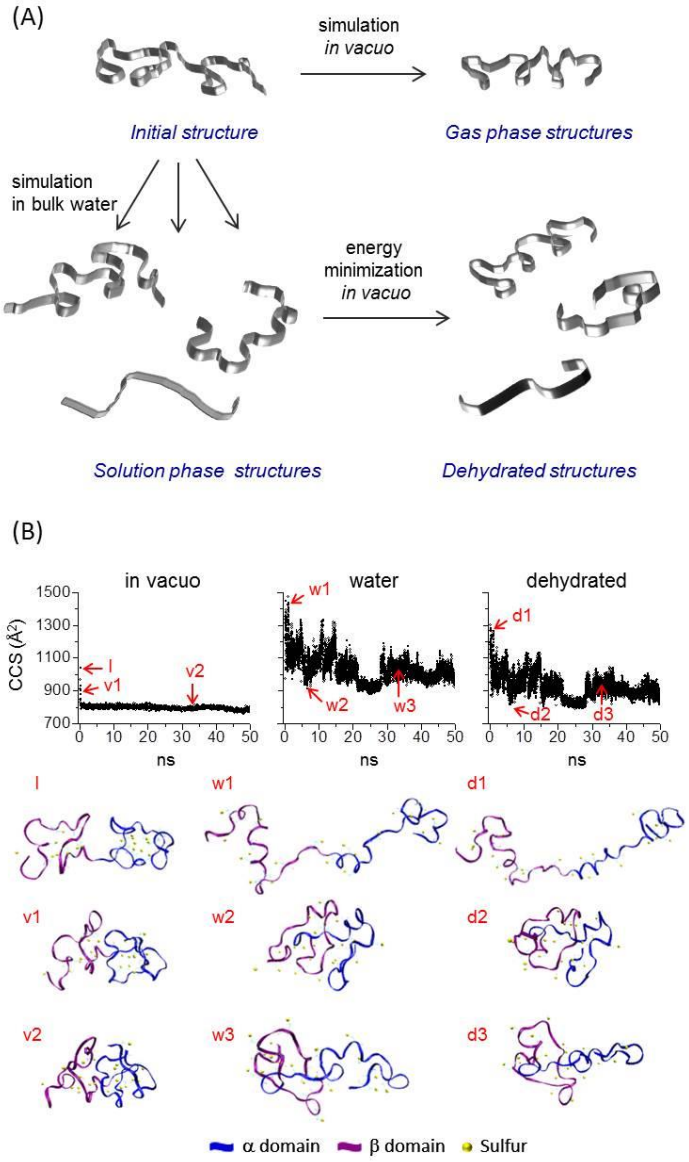

Figure 4.6. (A) Schematic representation of MD simulations in three models: *in vacuo*, implicit solvent (water), dehydration. *In vacuo* simulations generate the gas phase conformations and implicit water simulations were used to generate solution phase conformations. Subsequent dehydration from the solution phase conformations was performed by energy minimization *in vacuo* to generate the dehydrated conformation. (B) MD simulations of apoMT. Structure I corresponds to initial structure of apoMT obtained from NMR structure (Cd_7MT) after removal of all metal ions. Trajectories v1 and v2 are snapshots after simulation *in vacuo* for 0.05 and 33.2 ns, respectively. Trajectories w1, w2, and w3 are time-evolution structures after 1.0, 6.5, and 33.2 ns in water. Trajectories d1, d2, and d3 are dehydrated structures from solution structure w1, w2, and w3, respectively.

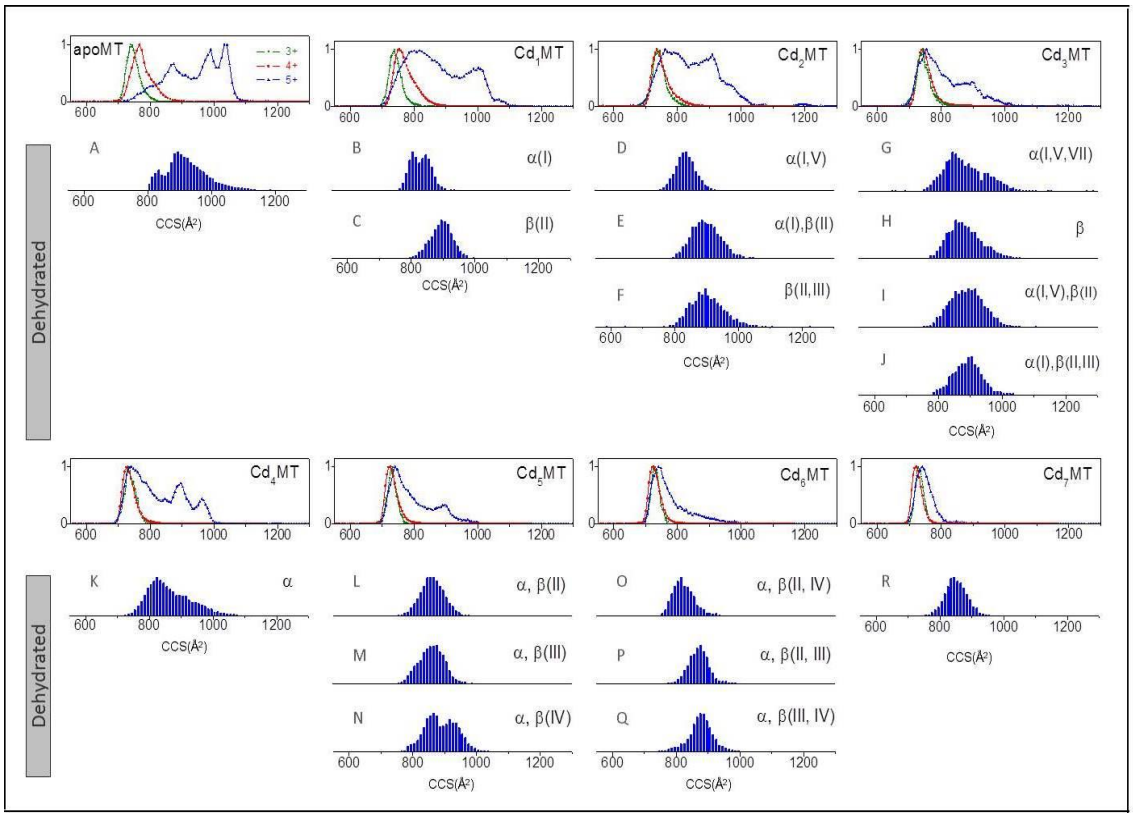

Figure 4.7. Histograms of CCS for simulated dehydrated structures. Time evolution simulation profiles for gas phase, solution phase and dehydrated structures are provided in Figure 4.8. The simulations were performed on eighteen MT conformers (A – R) that includes conformers with different metal ion composition as well as different metal ion binding sites. The domain and specific location of metal ions are indicated on the right of the histograms. ESI-IM-MS data for the three charge states (3+: green, 4+: red, and 5+: blue) are shown above the histograms.

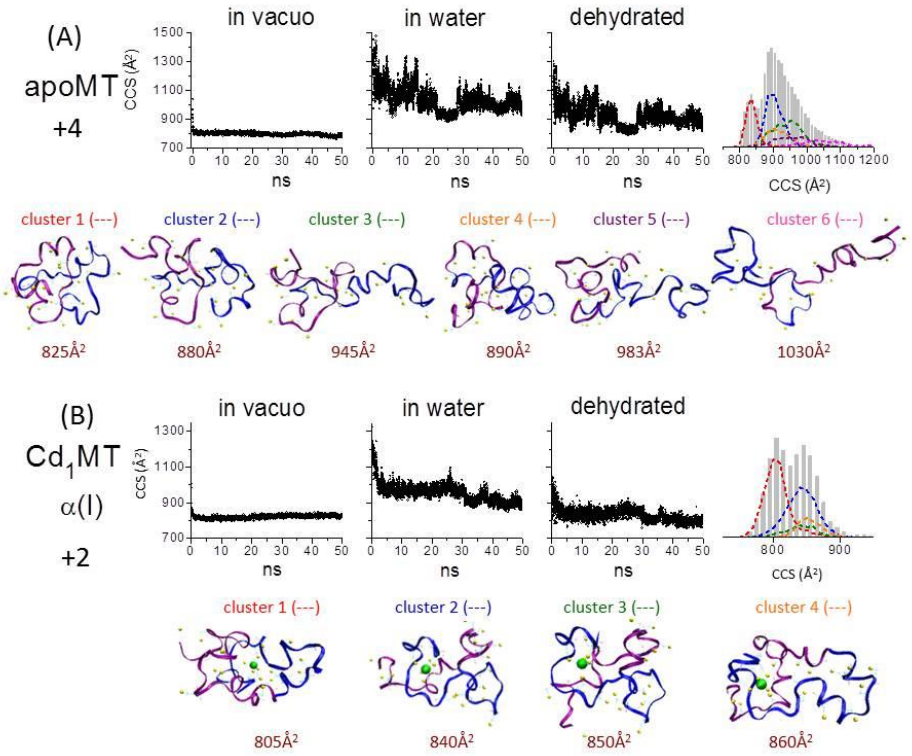

Figure 4.8. MD simulations for Cd_iMT (i = 0 – 7) at 300 K. Eighteen functional forms of MT (conformers A – R) were simulated, ranging from conformers with different metalation composition (i = 0 – 7) to those with different metal ion binding sites. The detailed metal ion configuration for each conformer is listed in each panel, including metal composition, specific binding sites of metal ion(s), domain location of the metal ion(s), and overall charge state). For conformers with the same metal composition but different metalation configuration, one of the conformers was selected for 50-ns MD simulations while others were calculated for 25 ns. The dehydrated structures were further analyzed based on structural similarity by MMTSB clustering toolset. The structure with minimal C_α-RMSD for each cluster is chosen as the representative structure. The data for each conformer contains (1) simulations using three models: *in vacuo*, implicit solvent, and dehydration, (2) overlay of histogram of CCS for the dehydrated structures (gray) and distribution of clusters (colored dashed lines), and (3) representative structures and corresponding CCS for each cluster.

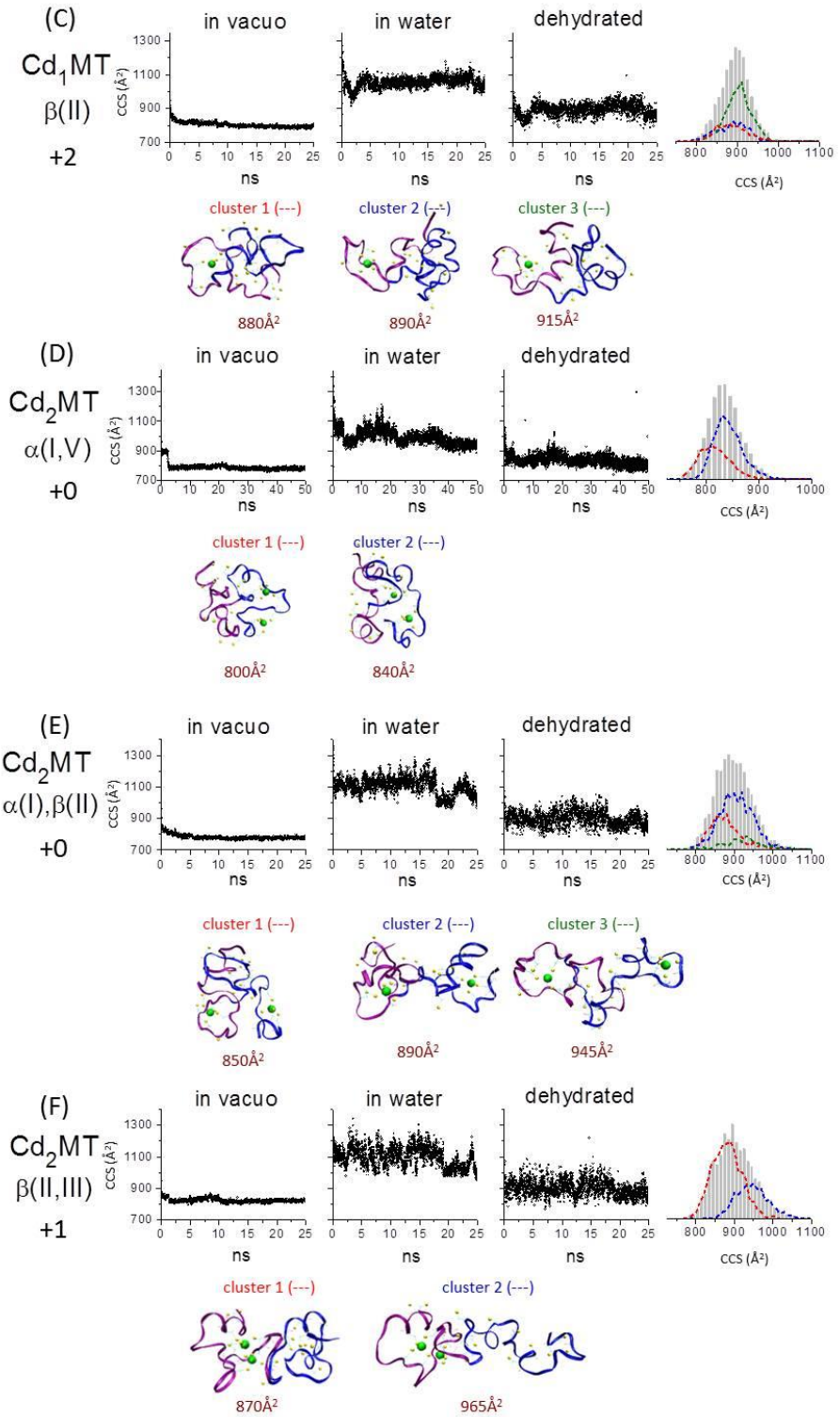

Figure 4.8 (Continued)

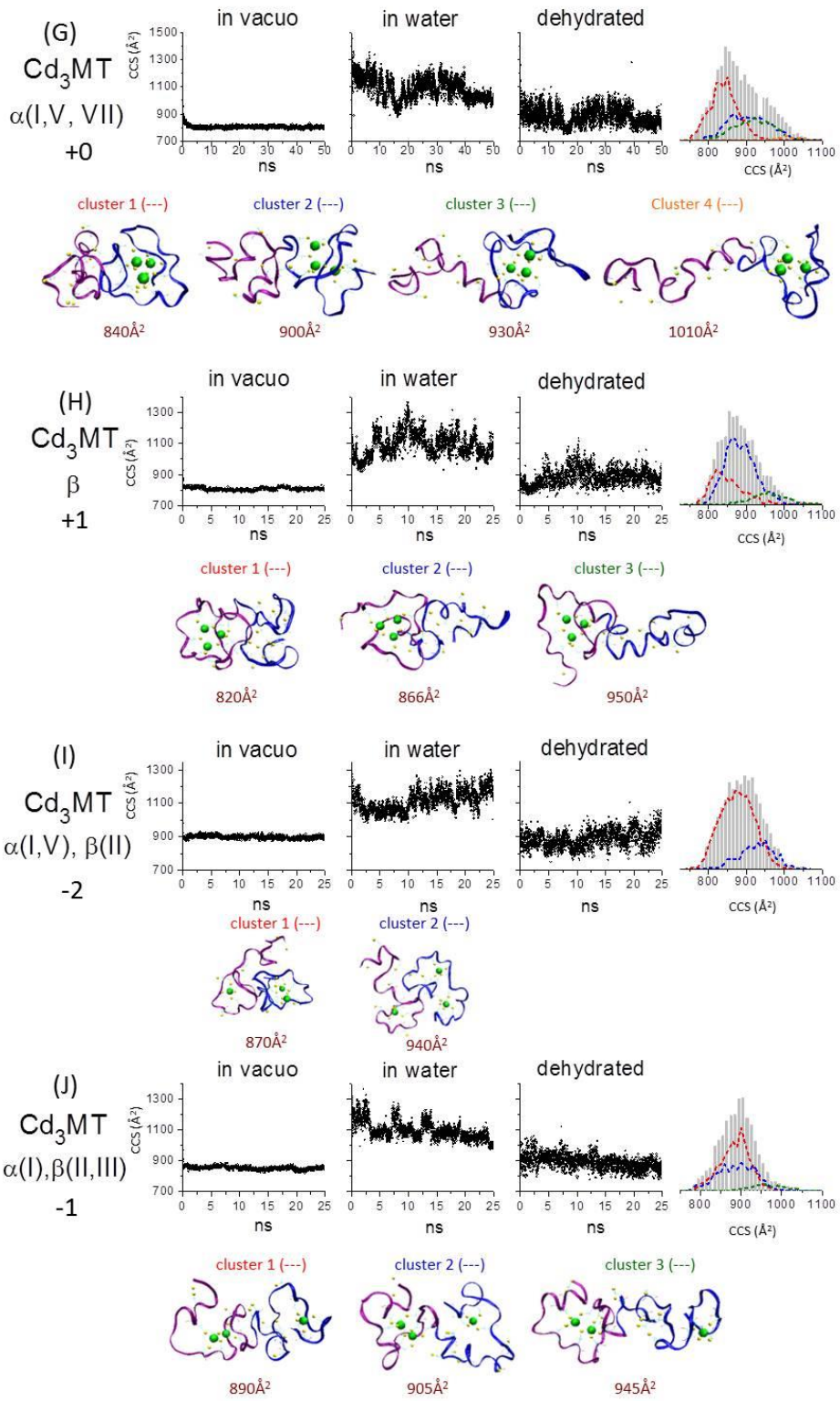

Figure 4.8 (Continued)

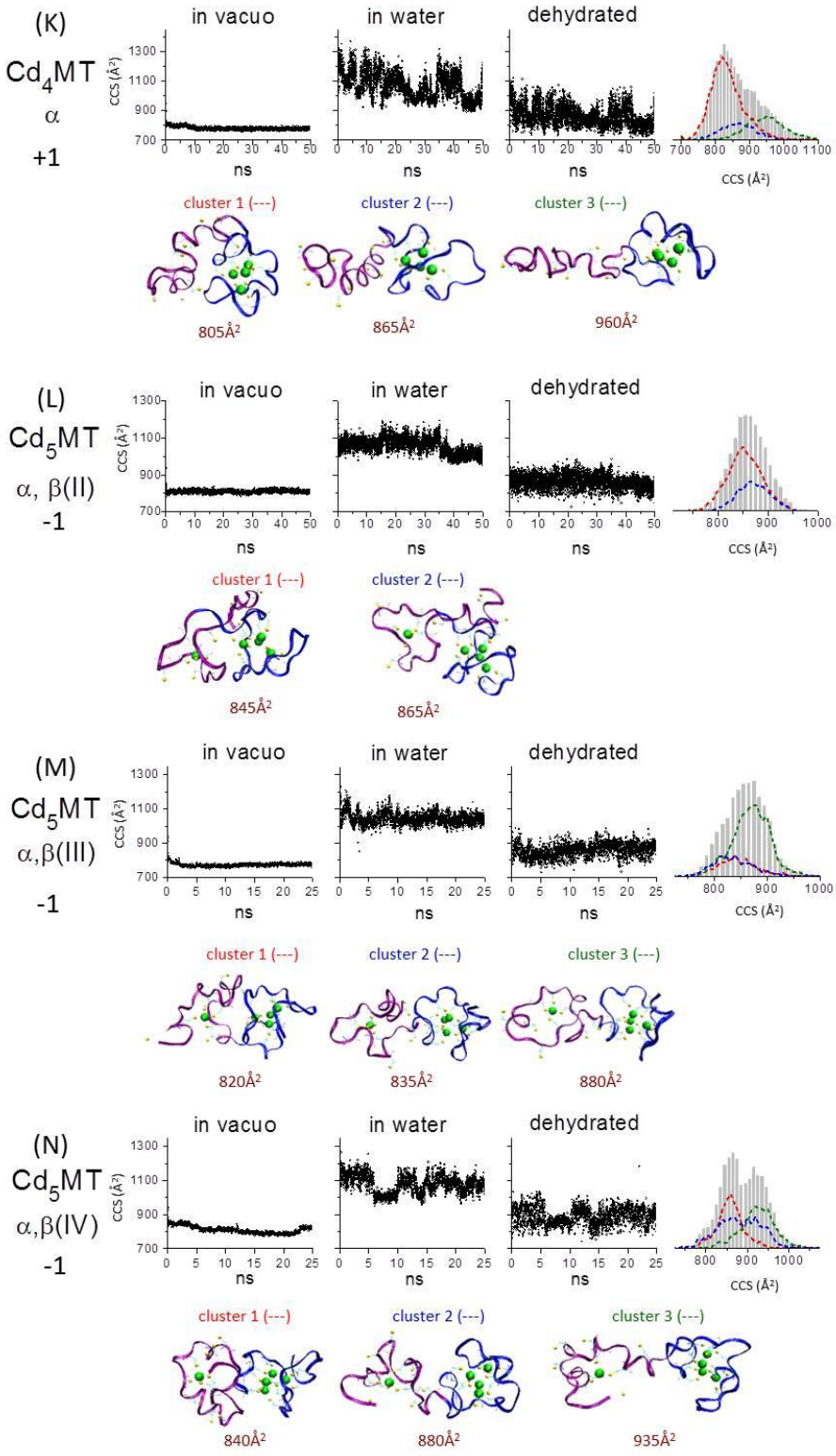

Figure 4.8 (Continued)

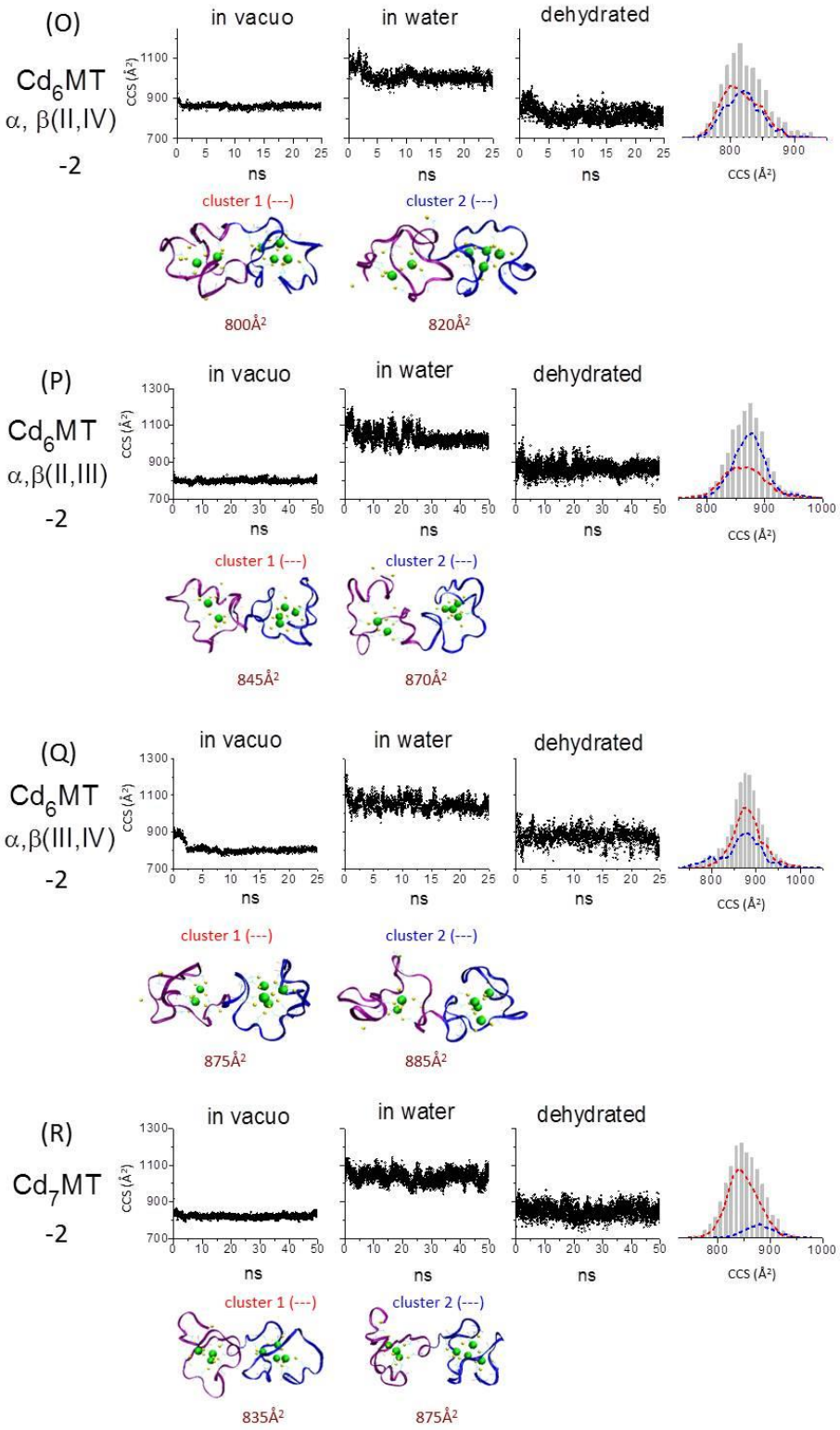

Figure 4.8 (Continued)

MD simulations were used to examine conformational changes that accompany metal ion Cd^{2+} ion binding. The simulations were performed by adding Cd^{2+} ions to specific sites according to the numbering scheme as first proposed by Wüthrich (**Figure 4.2)**.[37] Our previous study clearly showed that Cd_4MT is a stable intermediate and that all four of the metal ions are located in the α-domain;[127] however, the Cd_4MT product represents the stable product of metalation and its formation does not dictate that the initial metal ion addition is limited to the α-domain. Consequently, there remain ambiguities regarding metalation sequence and metal ion binding site(s) in partially metalated species, especially for the Cd_iMT (i = 1 – 3). As the apo- and partially-metalated MTs are proposed to be disordered, it is more likely all the binding sites are exposed and accessible for metal binding. In addition, the broad range of CCS for these partially-metalated forms (**Figure 4.3C**) provide strong evidence for multiple conformers, which most likely differ in terms of metal ion binding sites. Although it is difficult to design experiments that unequivocally resolve such issues, it should be possible to probe this further by using MD simulations to generate candidate conformers for partially-metalated Cd_iMT (i = 1 – 6) and compare predicted and experimentally measured CCS.

Figure 4.7 contains data for conformers generated by simulation that have metal ions located in different domains and different binding sites. The complete set of simulation data are shown in **Figure 4.8**. The CCS distributions for dehydrated conformations span the range of 800 – 1200 $Å^2$ (**Figure 4.7**). These data show that a single metal ion configuration can adopt multiple conformational states. For example,

for i = 1, the conformer with Cd^{2+} ion bound at site I yields two distinct populations of conformers (B; **Figure 4.7**). In addition, the conformers with Cd^{2+} bound in different binding sites can yield different conformational preference; note that for i =1, the B conformers have smaller CCSs than the C conformer (metal bound at site II). The difference in CCS for Cd_iMTs with Cd^{2+} bound to different sites decreases as the number of metal ions increases; presumably the species having a greater number of bound metal ions are folded or partially folded, which limits the numbers of conformer states. That is, for i > 3, the conformers with different metal distribution yield smaller difference in their conformational states, and for i = 7, the CCS narrows to a single population.

The comparison between CCS for MD generated conformers and experimental CCS suggests that the compact conformers observed in IM-MS experiments (Cd_iMT^{3+} and Cd_iMT^{4+} ions) agree quite well with the gas phase conformers (**Figure 4.3D**) and/or the compact states of the dehydrated conformers (**Figure 4.7**), whereas the extended conformers (Cd_iMT^{5+} ions) agree best with the dehydrated conformers. Clearly, the simulations appear to overestimate the CCS for the metalated forms and the deviation increases as the number of the metal ions increases (max error < 13%). Although not fully understood, the reason(s) for this discrepancy could be attributed to error in calibration of traveling-wave CCS,[166] intrinsic errors in MD and MOBCAL calculation,[167] and most likely the parameters of d-block metal ion (Cd^{2+}) used in AMBER force field and trajectory method, which remains an underdeveloped area in MD simulations and CCS calculation.[168-169]

Figure 4.9 contains MD simulation-generated representative conformers for gas phase and dehydrated Cd_iMT species (i = 0 – 7); detailed structural clusters and all representative conformations are provided in **Figure 4.8**. Although the gas phase simulations favor compact conformations for all the Cd_iMT ions, the dehydrated simulations represent a broad range of conformer populations. For example, the simulation for apoMT yields six distinct conformations. The compact conformer (CCS ~ 825 $Å^2$) matches a globular conformation whereas the other conformers in the range of CCSs from 880 – 1030 $Å^2$ display a greater extent of unfolding. Binding of the metal ions promotes protein folding in the region around the metal ions whereas other regions not involved in metal binding remain dynamic. Addition of a single Cd^{2+} ion yields globular-like conformers where the domain involved in metal binding appears to be partially folded while the other domain appears less ordered. Conformers of species with i = 2 – 3 are more ordered but the majority of the protein backbone remains unstructured and dynamic. We noted that the conformers with distinct structures may yield similar CCS. For example, at i = 2, conformers with CCS of 945 and 965 $Å^2$ are clearly different in terms of metal ion configuration and protein structure. At i = 4, three representative conformers contain a fully folded α-domain with structural variation that arises from the extent of unfolding in the β-domains. In the case of i = 5 – 6, the region of inter-domain linker remains disordered and results in several conformers that differ only in the project of the α- and β-domain. At i = 7, the simulation yields a single conformation that corresponds to the well-known dumbbell-shaped structure.

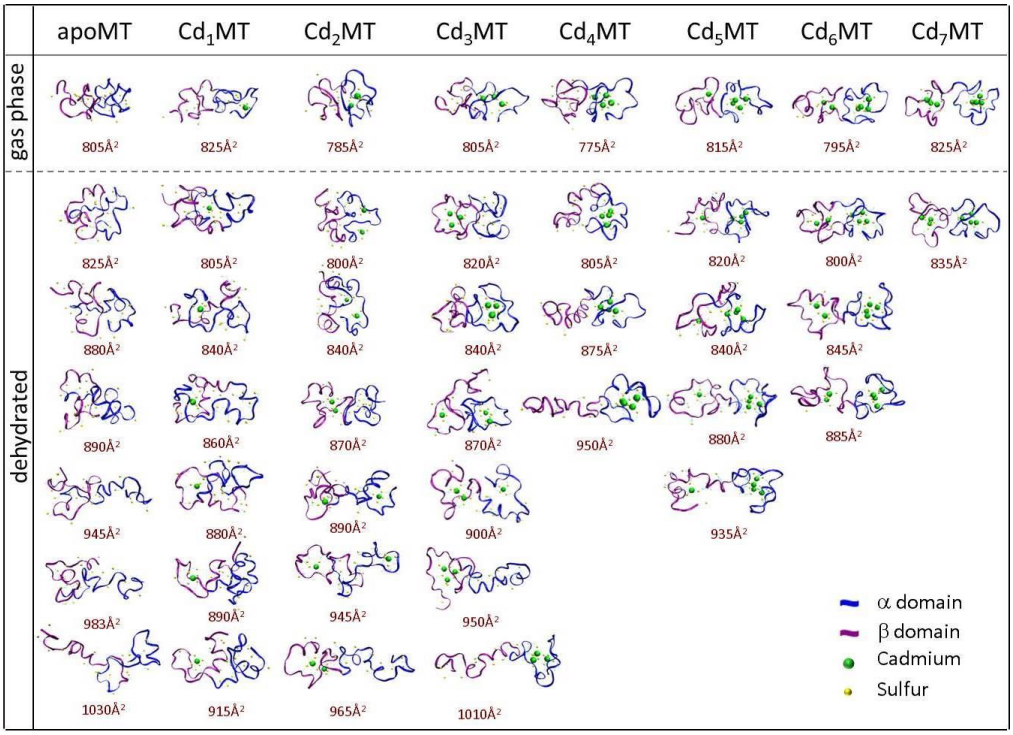

Figure 4.9. Representative structures of Cd_iMT (i = 0 – 7) in (A) gas phase and (B) solution phase. Numbers underneath the conformations correspond to the calculated CCS.

Discussion

IM-MS is now widely used for determination of collision cross sections (CCS) and conformational heterogeneity of peptide/protein ions; however, there are few studies where the ion-neutral CCS of native-like states are correlated to 3-D shapes and conformations generated by MD simulations.[45,61-62,66-67,157,170] An advantage of IM-MS is that it is a 'label-free' methodology that can be used to characterize protein conformations and track conformational changes without need for intrinsic or external spectroscopic probes (fluorophore and secondary structures),[45,171] even proteins with conformational micro-heterogeneities including folding of an intrinsically disordered

protein.[60] Most importantly, conformation information provided by IM-MS is molecule-specific, which permits the characterization of each metalated state in a dynamic, complex system.

The CCS profiles obtained from the centroid of the Cd_iMT^{3+} and Cd_iMT^{4+} ions are significantly smaller than that for the Cd_iMT^{5+}, and there may be multiple reasons for these differences. Although high charge states are subject to coulombic repulsion that could result in increases in protein size and CCS, it is more likely that the CCS for the 5^+ charge state originates from disordered solution phase conformations.[163,172] That is, the solution conformers exhibiting lower solvent-accessible surface area (compact conformers) give rise to the lower charge states and smaller CCS in gas phase, whereas the conformers having higher solvent accessible area (extended conformers) yield higher charge states and larger CCS.

MD simulations suggest that apoMT shifts rapidly between extended and globular-like conformations in solution (**Figure 4.6B**). Further structural analysis on these simulated structures shows that all potential hydrogen bonds appear to be transient with < 30 % frequencies (**Table 4.2**), suggesting that apoMT is highly dynamic and conformationally disordered in the bulk solution. Indeed, examination of the amino acid sequence of MT shows a compositional preference for small and hydrophilic amino acids and a lack of bulky hydrophobic and aromatic residues, which may prevent proteins from adopting a stable globular fold.[9] Complementary ESI techniques reveal similar structural information from hydrogen/deuterium exchange and proteolytic digestion, *i.e.*, apoMT is rapidly digested (trypsin) to peptides within 5 min and nearly

all hydrogens are exchanged instantly (data not shown). However, the above-mentioned methods do not provide information on conformation population. Ion mobility provides a direct measure for the conformational distribution; the IM-MS data suggest that apoMT comprises a highly heterogeneous ensemble that populates between CCS 750 $Å^2$ (globular-like compact conformation) and 1050$Å^2$ (coil-rich extended conformations, **Figure 4.9**). The data are consistent with the proposed disordered character of apoMT in solution, suggesting that the disorder features could be retained even in the absence of bulk water. This shows that IM-MS is capable of probing conformation population even for an "unstructured" protein.[66]

The simulation and experimental data for apoMT agree quite well in terms of the range of conformation population; however, these two sets of data do not show quantitative agreement with the overall CCS profiles *viz.* the abundances of the numerous microstates (**Figure 4.7, panel A**). The discrepancy can be explained as follows. The simulated profiles could be affected by the initial conformations, sampling methods and length of sampling times used to generate solution phase conformers and dehydrated conformations. Consequently, it is important to note that although the MD simulations are very effective for protein conformation searches, they provide largely qualitative data and only serve as predictors for the possible conformations. That is, MD simulations are used to provide candidate conformation for the conformational states observed experimentally. On the other hand, the experimental CCS profiles represent a composite of a number of specific conformations that are formed by the ESI dehydration

process and could also be complicated by some degree of collisional ion activation even though great care was taken to sample the ions as gently as possible.

H-bond: X-H---Y

DONOR			ACCEPTOR				Frequency (%)	Distance (Å)
Residue	amino acid	Y*	Residue	amino acid	H*	X*		
2	Asp	OD1	4	Asn	HD22	ND2	27.21	2.801
2	Asp	OD2	4	Asn	HD22	ND2	17.50	2.803
23	Glu	OE2	20	Lys	HZ1	NZ	10.45	2.783
2	Asp	OD2	20	Lys	HZ3	NZ	9.24	2.819
23	Glu	OE1	20	Lys	HZ1	NZ	8.55	2.783
2	Asp	OD1	20	Lys	HZ3	NZ	8.46	2.820
23	Glu	OE1	20	Lys	HZ3	NZ	8.02	2.786
28	Ser	OG	20	Lys	HZ2	NZ	7.26	2.877
10	Gly	O	14	Thr	HG1	OG1	7.19	2.811
2	Asp	OD2	20	Lys	HZ2	NZ	7.01	2.813
11	Asp	OD1	31	Lys	HZ2	NZ	6.90	2.816
11	Asp	OD1	31	Lys	HZ1	NZ	6.90	2.811
17	Gly	O	46	Gln	HE21	NE2	6.55	2.855
11	Asp	OD1	31	Lys	HZ3	NZ	6.24	2.811
55	Asp	OD2	56	Lys	HZ1	NZ	6.23	2.819
11	Asp	OD2	31	Lys	HZ3	NZ	5.87	2.816
55	Asp	OD2	56	Lys	HZ3	NZ	5.57	2.822
11	Asp	OD2	31	Lys	HZ2	NZ	5.48	2.814
55	Asp	OD1	56	Lys	HZ2	NZ	5.44	2.816
55	Asp	OD1	56	Lys	HZ3	NZ	5.34	2.817
55	Asp	OD2	56	Lys	HZ2	NZ	5.24	2.817
55	Asp	OD1	56	Lys	HZ1	NZ	5.11	2.810
23	Glu	OE2	20	Lys	HZ2	NZ	5.06	2.791

* H, X, Y atom names follow standard amino acids in AMBER

Table 4.2. Hydrogen bond analysis of trajectories of apoMT obtained from 50-ns MD simulation in implicit water model. The data suggest all potential hydrogen bonds appear to be transient.

ESI charge-state distributions have been directly linked to solution phase conformations because there is a strong correlation between observed charge states and

solvent accessible surface area.[162-163] Shifts in the charge state distribution upon addition of Cd^{2+} ions to MT (**Figure 4.3B**) could be viewed as evidence that coordination of Cd^{2+} to MT induces conformational changes; however, IM-MS CCS and MD simulations provide even stronger evidence of the metal-induced conformational changes. The CCS profiles (**Figure 4.3C**) show a marked shift to smaller values and reduction in peak width as the number of metal ions increases, implying that metalation favors more compact, ordered conformations. Although apoMT shows a wide range of conformational states, binding of a single Cd^{2+} ion induces reduction in accessible surface area as evidenced by changes in the charge state distribution and protein ion size (decreased CCS). Subsequent addition of Cd^{2+} ions promotes further changes in charge state distributions and reduction in protein ion size; however, the regions of the protein backbone that are not directly involved in metal binding remain disordered as indicated by the peak tailing to higher CCS profiles.

It is somewhat surprising that the marked changes in CCS profiles are observed upon addition of a single Cd^{2+} ion (**Figure 4.3C**). Shifts in the CCS profiles for the stepwise addition of 1, 2 and 3 Cd^{2+} ions are indicative of formation of more compact conformers and an ion population that is composed of multiple conformational states. The comparison between experimental and theoretical CCSs (**Figure 4.7**) suggests that the broad ion populations for Cd_iMT ($i = 1 - 3$) are likely attributed not only to multiple conformational preferences of a single metal ion configuration but also to multiple conformers with different binding sites of metal ions. Our earlier study showed clear evidence that the metal ions of Cd_4MT are exclusively located in the α domain.[127]

Therefore, it is highly probable that Cd^{2+} ions are initially bound to a number of sites and then shuttled to more thermodynamically stable sites. In addition, the CCS for the entire ion population shows consistent decrease as the number of metal ions bound increases except for the case from i = 3 to 4 (**Figure 4.3C**; abundances of conformers at CCS 850 – 1000 $Å^2$ increase), which provides evidence for a distinct transition of conformation. Although the reason(s) is not fully identified, the data could possibly be correlated to metal swapping to the α domain (Cd_4MT) from conformations in which metal ions are present in both domains (Cd_3MT). This model suggests that the metalation mechanism of Cd^{2+} is probably similar to that of Co^{2+} proposed by Vasak and Petering.[33,173] We note that the proposed metalation model is derived from thermodynamic partially-metalated products under equilibrated conditions, which might be different from that based on the kinetic products.

In the case of i = 4, the α domain is fully folded,[127] thus the empty β-domain is most likely highly disordered. Indeed, the MD simulation suggests that the distinct conformations for Cd_4MT can be attributed to a different orientation of the β-domain (**Figure 4.9**). As Cd^{2+} ions bind to the β-domain, *i.e.*, i = 5 – 6, the conformational heterogeneity decreases (CCS profiles become more narrow) indicative of formation of compact conformers. That is, the population(s) corresponding to conformers that have elongated inter-domain linkers (CCS 800 – 950 $Å^2$) decreases as the number of Cd^{2+} increases. At i = 7, both CCSs obtained from the IM-MS and MD narrow to a single population that is consistent with the previously suggested dumbbell-shaped structure.[37] Collectively, the data show that metal-induced folding of MT occurs through multiple

pathways and involves transitions from disordered-to-ordered, extended-to-compact conformational transition.

In addition to the conformation information provided by IMS/MD data, *t*he ESI MS provides valuable information for relative stabilities for each metalated form.[127] We have previously reported the ratio of apparent binding constants for the stepwise metal-binding, K_1:K_2:K_3:K_4:K_5:K_6:K_7 = 15:3.0:1.0:16:3.2:1.0:3.9 for human MT-2A[127] that indicates Cd_4MT is a relatively stable intermediate. The relative distribution of the Cd_iMT observed in these experiments is different from what was reported in Stillman's work that proposed a noncooperative manner of binding between Cd^{2+} and human MT-1A.[120,174] Although the reason(s) for this discrepancy are not fully identified, it could be attributed to slightly different sample preparation and ESI conditions used. In Stillman's work, samples were incubated under argon and capillary voltage used was 3 – 4.2 kV ESI; in our study, samples were in the presence of TCEP and ~ 1 – 1.5 kV capillary voltage was used to minimize the possibility of ESI-induced oxidation. The discrepancy could also be due to different isoforms analyzed, as there is increasing awareness that the metal-binding properties of one isoform can not be directly applied to that of other isoforms.[175] The IM-MS and MD simulations provide new information for understanding the metalation mechanism of MT-2A. The large value for K_1 is attributed to the disordered apoMT that presents solvent-exposed cysteinyl sulfur groups thereby accelerating reactivity to metal ion(s). The decrease in values from $K_1 - K_3$ and $K_4 - K_6$ are consistent with conformational changes that occur as the number of bound metal increases, in line with a model proposed by Stillman.[49] Specifically, the binding of

metal ions induces protein folding and inverts the active cysteinyl sites from the protein surface to the protein interior.[49] These structural changes potentially relocate the remaining active cysteinyl sulfur groups thereby decreasing their accessibility/reactivity toward incoming metal ions.[176-177] The sharp increase in K_4 is linked to a large-scale conformational change that accompanies metal ion rearrangement (swapping) that shifts the equilibrium from a less stable Cd_4MT (metal ions located in both domains) to a more stable conformation that has all four metal ions located in the α-domain.

Conclusion

Here, the first experimental data describing the effect of stepwise metalation on the conformation of human MT-2A is reported. The changes in ESI charge state distribution for metal-free partially metalated to fully metalated states are attributed to successive decreases in the solvent accessible surface area. IM-MS and MD data clearly show that the metal-free protein is conformationally disordered and metalation yields compact and ordered conformations. The partially-metalated forms populate multiple conformational states that reflect conformational multiplicity of the protein backbone that do not involve metal binding. It appears that initial metal-ion binding occurs in both the α- and β- domains, but metal swapping between the α- and β-domains ultimately yields the Cd_4MT product ions where the metal ions are isolated to the α-domain.[127] MD simulations are consistent with metalation occurring along multi-trajectory pathways, with the final products corresponding to compact conformations; however, the partially-metalated intermediates populate multiple conformational states. Both experimental and

theoretical data support a metalation model where metal binding induces transitions from disordered-to-ordered and extended-to-compact conformations. This study provides, for the first time, experimental data and possible descriptions of conformations for the partially-metalated MTs that could have significant impact on the unknown conformational space in the protein folding landscape of MTs and serve as a model for other metalloproteins.

This study underscores the importance of IM-MS for mapping conformational changes of biologically important proteins that are not amenable to study by traditional structural techniques. An additional key component of this study is the importance of MD simulations for establishing the chemical/biological relevance of the experimental data. Most importantly, NMR and X-ray diffraction provide detailed structural information for a single metalated (fully-metalated) Cd_7MT form, whereas the IM-MS/MD approach provides a global and dynamic view that shows stepwise metal-induced conformational transition of an ensemble in terms of their 3° and 4° structure. It is anticipated that this approach could be applied to other complex systems that are highly dynamic and/or heterogeneous *viz.* comprising multiple species and multiple conformations in solution.

CHAPTER V

CORRELATING ION-NEUTRAL COLLISION CROSS SECTIONS TO PROTEIN NATIVE CONFORMATION AND ENERGY FOLDING LANDSCAPE

Introduction

The function and activity of cellular proteins is determined by their three-dimensional (3-D) structure, but correlating function and structure is immensely challenging owing to the fact that the native-state(s) of many proteins related to human diseases are disordered.[178-180] A high percentage (~ 40%) of all human proteins are partially or completely disordered,[181] and many intrinsically disordered proteins (IDP) play important roles in disease mechanisms,[182-183] including p53 regulation in cancer pathways, amyloid beta (Aβ) and tau protein aggregation in Alzeheimer's disease, α-synuclein in Parkinson's disease, and it is proposed that ~80% of cancer-associated and ~65% of cell-signaling proteins are IDPs.[184] It is thought that structural flexibility and plasticity (disorder) provide functional advantage,[179-180] which enhances a wide range of physiological pathways involving a disorder-to-order structural transition.[185] Characterization of IDP is challenging because they are inherently difficult to crystallize,[186] and conformational diversity (disorder) complicates NMR approaches.[187] Consequently, there is increasing interest in developing mass spectrometry-based approaches for characterizing IDPs. Proteomic mass spectrometry (MS) approaches combined with hydrogen-deuterium exchange (HDX)[188] and chemical derivatization[123-124,189] provide high throughput, high sensitivity, and versatile strategies for protein

identification.[52,190] These approaches are complemented by combining "native-ESI" and ion mobility-mass spectrometry (IM-MS) by providing ion collision cross section (CCS), a direct measure of the physical size and shape of the ions, for studies of conformational heterogeneity,[55] elucidation of protein and protein complex conformations,[56-57] and characterization of IDPs.[58-65] While there is mounting evidence that gas-phase ions formed by ESI retain elements of solution-phase structure(s),[170,191] the extent to which gas-phase ion structures correlate to solution-phase structures is largely unknown.

ESI is an excellent choice for studies of biomolecules because ions are generated directly from solution and the initially generated ions have low internal energies. Beauchamp *et al.* proposed that the ESI produces ions by a "freeze-dried" mechanism, *i.e.*, in the final stages of ion formation the ions are cooled by solvent evaporation to temperatures of 130-150 K.[192] It is important to recognize, however, that these ions are subsequently warmed by collisions in heated capillaries and/or by collisions with background gas as they traverse the IM and MS analyzers.

Here, we show that the correlation of gas- and solution-phase structures has a significant dependence on changes in the ion's internal energy or "effective ion temperature" (T_{eff}) that occur following ion formation. Ubiquitin is an excellent model for investigating the effects of T_{eff} on ion mobility CCS because it has been extensively studied, both in solution and gas phase as well as by explicit-solvent MD simulations.[193] Clemmer *et al*. noted that ubq^{6+} and ubq^{7+} ions have CCS that are similar to the native fold,[194] and collisional heating of the ions promotes unfolding.[195] Bowers also showed that ubiquitin ions formed by ESI from solutions that stabilize the native state yield

tightly folded solvent-free ions that have CCS that match the sizes of the native state.[196] The extensive database of the conformer preference of solution-phase ubiquitin and the prior folding/unfolding studies of gas-phase ions provide the foundations for our discussion of the dependence of the experimental CCS on T_{eff}. In addition to an ordered protein, an intrinsically disordered and less studied protein, human apo-metallothionein-2A (MT),[9,37] was selected for this investigation. ApoMT, a small metal-binding protein that is similar in size to ubiquitin,[37] does not exhibit specific secondary/tertiary structural features, but the metalated form assumes increased order as the numbers of metal ions increase.[2,9,11]

IM-MS and molecular dynamics (MD) simulations are employed to address the question --- *how closely related are the structures of ions sampled by IM-MS to the "native-conformation" of the solution-phase protein ions?* The experiments reveal specific effects of various instrumental parameters on CCS. Although this study is limited to the TW IM-MS instrument (Synapt G2 HDMS),[197] the results are applicable to all IM-MS instruments. The results clearly show that unintended collisional heating alters the T_{eff}, and that such changes in T_{eff} have strong effects on the conformational diversity as evidenced by changes in the IM CCS; however, careful attention to instrument tuning minimizes these effects and "native-like" conformers can be retained. The experimental data are compared with data obtained by MD simulation at different temperatures, which provides insights into the extent of retention of solution phase structures by IM-MS.

Experimental

Sample preparation

Bovine ubiquitin (Sigma-Aldrich, St. Louis, MO) was reconstituted to 10 μM in 50 mM ammonium acetate (pH 7.4). ApoMT sample (Bestenbalt LLC, Tallinn, Estonia) was reconstituted to 7 μM using 50 mM ammonium acetate (pH 7.4) solution containing 1 mM Tris(2-carboxyethyl)phosphine hydrochloride (TCEP-HCl; Thermo Fisher Scientific, Rockford, IL).[65,127] Metalated Cd_iMT (i = 1 – 7) were obtained by sequential addition of 1, 2, 3, 4, 5, 6, and 7 μL of 1 mM of Cd^{2+} to 100 μL of a 7 μM apoMT solution. Care was taken in all ESI-IM-MS experiments reported here to exclude ESI-induced protein oxidation and non-specific metal binding as previously described.[65,127]

Ion mobility-mass spectrometry

The ESI IM-MS experiments were performed on a Waters Synapt G2 HDMS instrument (Manchester, UK). "Native state" ESI conditions (H_2O, buffered at pH ~ 7.4 by using 50 mM ammonium acetate) were used for the studies described below, and the solutions containing the proteins were directly infused into the mass spectrometer at a 0.5 μL/min flow rate. ESI-MS spectra were acquired in the positive ion mode with a capillary voltage of 1.0 – 1.5 kV. The effects of the changes to voltages applied to the sampling cone (SC), extraction cone (EC), and trap bias (TB), as well as gas flow rate to the He cell and TW analyzer (N_2) on the CCS profiles (see **Figure 5.1** for schematic of the Synapt G2 HDMS instrument) were investigated. A TW velocity of 550 m/s and TW height of 25 V was used for the ubiquitin experiments and 300 m/s and 20 V for MT experiments. All mass spectra were calibrated externally using a solution of sodium

iodide. CCS were calibrated using solutions of myoglobin, cytochrome C, and ubiquitin as previously described.[128]

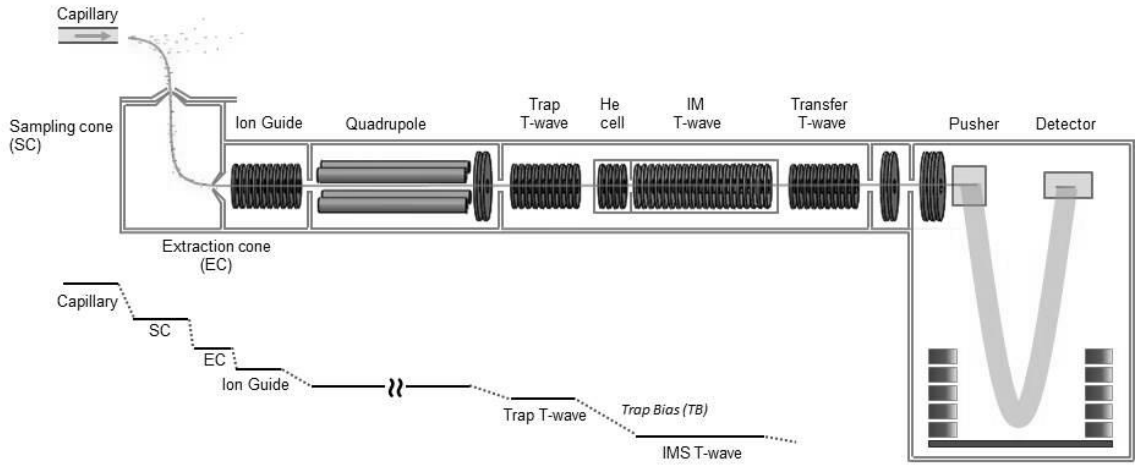

Figure 5.1. Schematic of the Synapt G2 TW-IMS instrument. CCS profiles shown in Figure 5.2 were acquired by varying helium flow rate to the He chamber positioned at the entrance to TW mobility separator, the voltages applied to the individual ion focusing elements (SC, EC, and TB) that are used to guide the ions from the ESI emitter tip to the entrance of the TW mobility separator; SC refers to the ESI skimmer cone, EC denotes the extraction cone and TB denotes the trap bias lense. N_2 gas flow rate to the TW mobility separator was also varied, and the range of flow rates is noted across the top of Figure 5.2.

MD simulations

The NMR structure of ubiquitin (PDB: 1D3Z) and that of separate α and β domains of human MT-2A (1MHU and 2MHU)[37] were used as starting structures for MD simulations. A complete description for MD simulations and parameters for Cd^{2+} ion were described previously.[65] The initial structures were energy-minimized, followed by simulations *in vacuo* or by implicit solvent model. To mimic the inherent dehydration

in the ESI process, the solution phase structures were subsequently energy minimized *in vacuo* to generate "dehydrated structures".[45,59,66,160] To evaluate the protein conformational change caused by ion heating by the IM-MS spectrometer, simulations with increasing temperature were performed. A complete description for MD simulations and data analysis is provided in Appendix. The simulated structures were clustered using a Cα root mean square deviations (RMSD)-based clustering algorithm in MMTSB tool set.[161] Representative structures, determined as those closest to the centroid of each cluster, were used to represent the candidate experimental structures.

Temperature map

The temperature map (**Figure 5.2**) for ubq^{6+} ions was estimated from the range of experimental CCS that were decomposed into multiple conformational families (compact: C; intermediate: I; and extended: E) using Origin v8 (OriginLab Corp. Northampton, MA). The best fit to the experimental peak profiles was obtained using six peaks (see **Figure 5.3**). The abundances of individual conformations were determined by calculating the area under the peaks. Changes in the abundances of each conformer clearly evident on T_{eff} were then compared to temperature-dependent MD simulations. A strong correlation was obtained between temperature and the value of CCS for the simulated trajectories, *i.e.*, conformers C, I and E are produced at different temperatures (see Results section). Therefore, the T_{eff} for each experimental condition was estimated using "abundance-weighted" CCS that are calculated on the basis of the relative population of the C, I, E conformers.

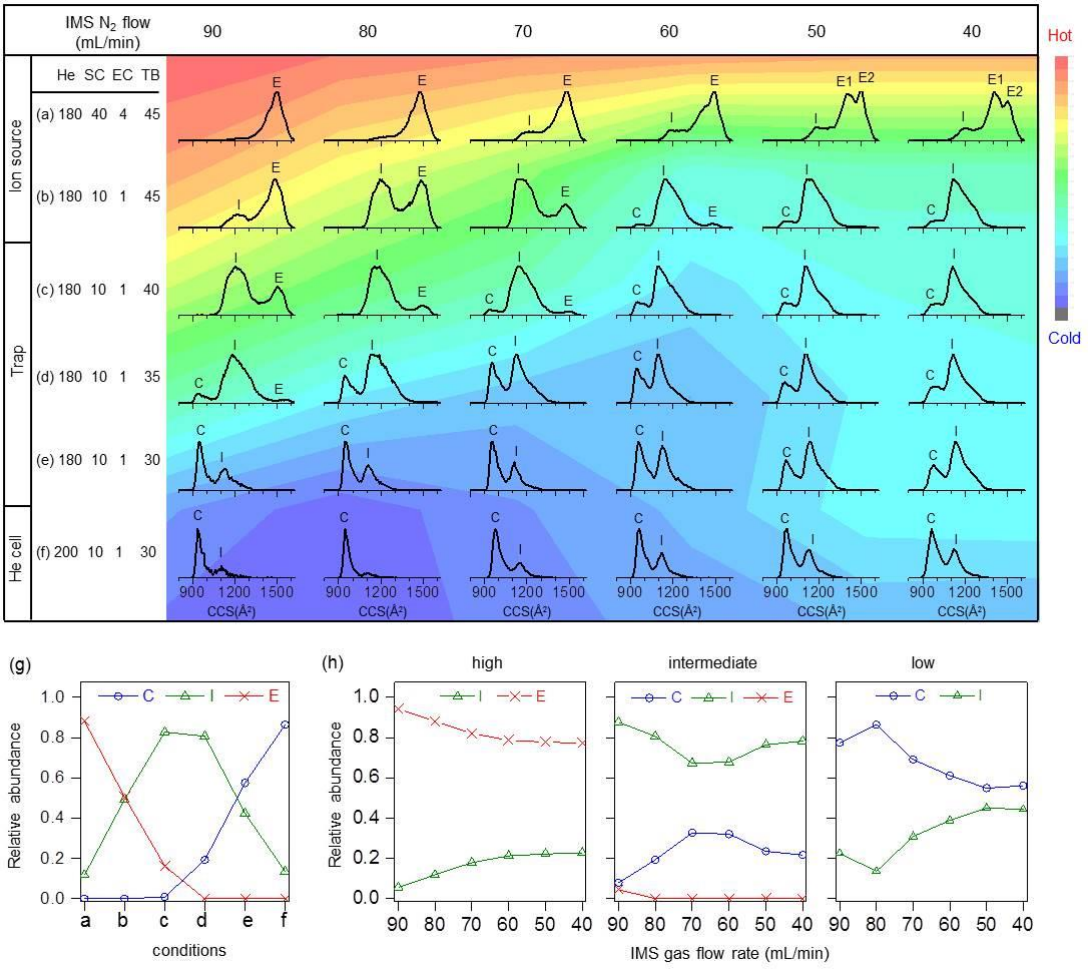

Figure 5.2. CCS profiles for ubq^{6+} ions acquired using a range instrumental tuning condition. The values listed as rows a − f are parameters that are applied prior to the TW-IMS N_2 analyzer and columns 1 − 6 display the effects of N_2 flow within the IMS cell (90 − 40 mL/min). The specific regions of the instrument and the notation used in (a) − (f) are illustrated in Figure 5.1. The color shading of the CCS profiles are intended to show the transition in T_{eff} sampled by the specified instrument tuning conditions, where T_{eff} decreases on going from red to blue. The changes in the relative abundance of the conformational states (compact (C), intermediate (I) and extended (E)) of ubq^{6+} are plotted in (g) for a constant TW N_2 flow rate (80 mL/min) and similar plots shown in (h) were obtained by at parameters (a), (d) and (f) while varying the N_2 flow rate to the TW analyzer. The temperature map was generated to illustrate the extent of ion heating for each experimental condition.

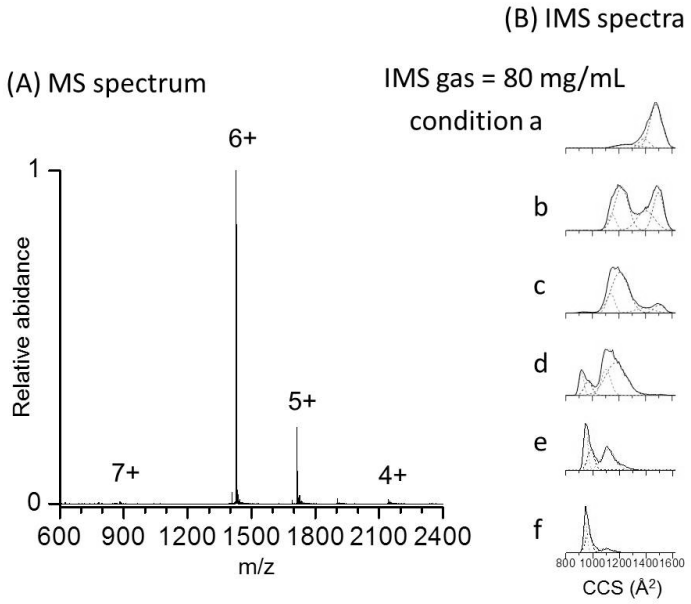

Figure 5.3. (A) Representative ESI MS spectrum of ubiquitin in 50 mM ammonium acetate (pH 7.4). We note that the charge state distribution (CSD) shown here is very similar to that reported by Williams and coworkers who also used Synapt G2,[198] *viz.* the 6+ is the most dominate species. However, the MS spectra for ubiquitin under pure water reported by Clemmer[199] and Bowers[196] using home-built instruments are shifted to higher CSD where the 7+ is the most dominant peak. In current study, our data show CSDs are similar when different instrumental conditions are used; however, the CCS profiles differ significantly. For example, (B) are IMS spectra that are collected using parameters (**a**) – (**f**) with IMS N_2 flow rate of 80 mg/mL (see Results section, main text). The CCS profiles are decomposed into multiple Gaussian peaks (dotted lines) using Origin 8.0. Best fit was obtained with the use of 6 peaks. Two peaks fall within the range of the experimental compact conformer **C** (CCS ~ 880 – ~1000 $Å^2$), another two correspond to **I** (~ 1050 – ~1350 $Å^2$), and the other two are **E** (~1400 – ~1600 $Å^2$).

Results

IM-MS of ubiquitin (ubq^{6+}) ions

"Native state" ESI of ubiquitin yields predominately the $[ubq + 6H]^{6+}$ (ubq^{6+}) ion (relative abundance > 75 % abundance; **Figure 5.3**). CCS profiles for ubq^{6+} ions obtained using a range of instrument parameters (see **Figure 5.1**) are shown in **Figure**

5.2. Although the following discussion is limited to ubq^{6+}, data for ubq^{7+} ions are very similar to that for ubq^{6+} ions (see **Figure 5.4**). Note that most of the CCS profiles are broad and composed of multiple unresolved signals indicative of an ion population that is composed of multiple conformers. Changes in *the CCS profiles as a function of instrument tuning clearly show that conformational changes are occurring post-ESI, but the conformational changes are not reflected in the ESI charge state distribution*. For convenience the CCS profiles are divided into three conformer families: compact (**C**: CCS ~ 880 – ~1000 $Å^2$), intermediate (**I**: ~1050 – ~1350 $Å^2$), and extended state (**E**: ~1400 – ~1600 $Å^2$), but it should be noted that each family is composed of overlapping/unresolved peaks indicating the presence of multiple similar conformers. For example, two distinct E conformations (CCS ~ 1400 $Å^2$ (E1) and ~ 1500 $Å^2$ (E2)) were observed for N_2 flow rates of < 50 mL/min of the condition (**a**) (**Figure 5.2a**).

The CCS profile shown in row (**a**) of column 1 (**Figure 5.2**) was acquired using the manufacturer's default parameter, which affords the highest ion transmission and detection sensitivity, and it is clear that this condition yields the highest abundances of ions corresponding to the **E** state. The CCS profiles in each column reveal a significant dependence on the electric field and He flow. For example, high SC and EC favor the extended conformer **E**, and reducing these potentials yields appreciable abundances of **I** (see (**a**) – (**b**)). The effect of TB is illustrated by comparing the data contained in (**c**) – (**e**), where the most abundant conformers shift from **I** to **C** as TB is varied from 45 – 30 V. The effects of changing the flow rate of He to the He cell is illustrated in (**f**). For

example, using the same conditions as in (**e**) but increasing the He flow to the maximum (200 mL/min) yields predominately **C**.

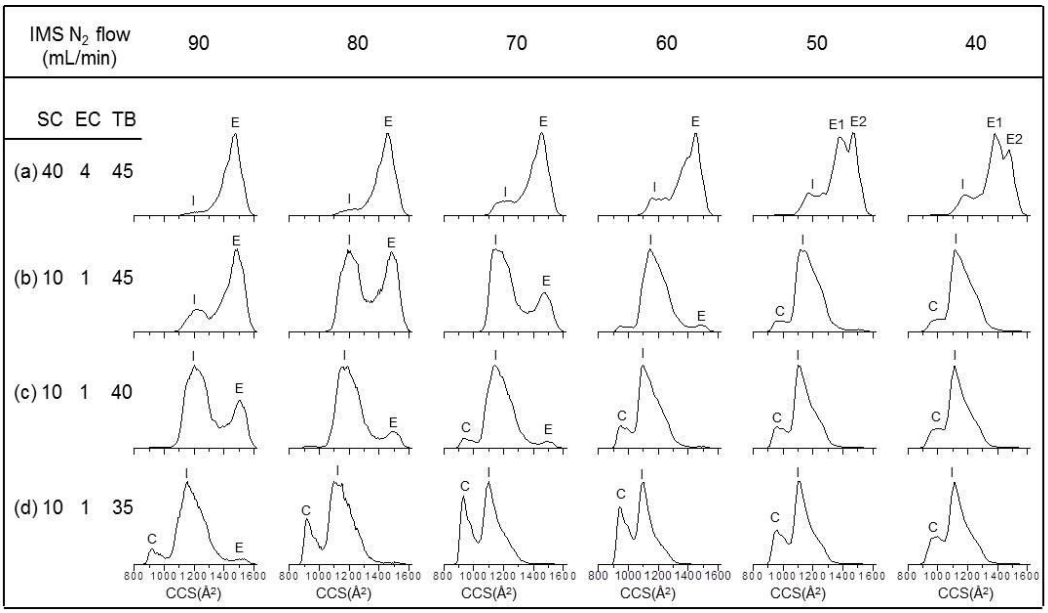

Figure 5.4. Ion mobility CCS for ubq^{7+} ions electrosprayed from an acidic condition (50%:50%:1% MeOH:H_2O:Acetic Acid). The CCS data collected using various instrumental parameters are shown in a two dimensional matrix. The CCS profiles vary significantly. Values of the parameters for the gas flow of He cell (He) and the voltages of sampling cone (SC), extraction cone (EC), and trap bias (TB) for the conditions a – f are listed in left column of figure: (a) 180 mL/min, 40V, 4V, 45 V; (b) 180 mL/min, 10V, 1V, 45 V; (c) 180 mL/min, 10V, 1V, 40 V; (d) 180 mL/min, 10V, 1V, 35 V; (e) 180 mL/min, 10V, 1V, 30 V; (f) 200 mL/min, 10V, 1V, 30 V, respectively. Columns 1 − 6 show the effects of N_2 flow within the IMS cell on CCS, operated with a constant rate of 90 (left) through 40 mL/min (right).

A quantitative plot that illustrates the effects of the electric fields and the gas (He) flow rate to the He cell is represented in **Figure 5.2(g)**, which shows the abundances for the three conformer families (**E**, **I** and **C**) at a fixed IMS gas (N_2) flow

rate (80 ml/min) as a function of parameters for (**a**) − (**f**). Note that these parameters result in changes in T_{eff} prior to the ions entering the TW IMS analyzer. The results show that the sequential decrease of electric field and an increase in He flow (**a**) – (**f**) favors more compact conformers.

The CCS profiles also show a significant dependence on the N_2 gas flow rate, which can be seen by comparing the profiles in each row as the N_2 flow rate to the TW analyzer is reduced from 90 to 40 mL/min. For example, as the N_2 flow rate is reduced from 90 to 40 mL/min the profiles in row (**a**) shift to smaller CCS, transitioning from **E1** to **E2** and finally to **I**. The quantitative data showing changes in the CCS profiles as a function N_2 flow rate to the TW separator are shown in **Figure 5.2(h).** Here, the abundances of **C**, **I** and **E** are plotted for various N_2 flow rates obtained using instrument tuning parameters that favor high, intermediate and low electric fields, conditions (**a**), (**d**) and (**f**) in **Figure 5.2**, respectively. As noted above, conformer(s) **E** dominates the CCS profiles taken using high electric fields (left panel, **Figure 5.2(g)**) and decreasing the N_2 flow rate causes a reduction in **E** with a concomitant increase in the abundance of **I.** The data obtained using intermediate electric fields, *i.e.*, those used for **Figure 5.2(d),** are dominated by **I** and the abundances of **C** and **E** are lower at N_2 flow rates of 90 ml/min, and changing the flow rate (80 – 70 ml/min) results in an increase in **C** and decreases in both **I** and **E** (medium panel, **Figure 5.2(g)**). The abundances of **C** and **I** do not change significantly for N_2 flow rates of 70 – 60 ml/min, and further decrease in the flow rate (< 60 ml/min) results in an increase in **I** and concomitant decrease in **C**. Lastly,

the data collected at low electric fields (row **f**) show that **C** is favored at N_2 flow rates of 90 − 80 mL/min but the ion population is shifted to **I** at low gas flow rates.

IM-MS of human MT-2A

CCS profiles for apoMT, and the partially- and fully-metalated states (Cd_iMT^{5+} i = 0 – 7) are shown in **Figure 5.5.** We previously showed that addition of Cd^{2+} to MT promotes folding as evidenced by increase in the abundances of compact conformers as the number of bound metal ions increases.[65] In that paper we only reported CCS data for the Cd_iMT ions (i = 0 – 7) that were obtained using instrument parameters that correspond to a low T_{eff} condition.[65] The data shown in **Figure 5.5** span the same range of instrument tuning parameters as discussed above for ubq^{6+} ions. The effects of T_{eff} can be seen by comparing the CCS profiles in rows (**a**) – (**e**) in **Figure 5.5**. That is, (**a**) reports CCS data for ions having high T_{eff} and high ion transfer efficiencies and (**e**) corresponds the condition where lowest T_{eff} is achieved. As expected the condition (**a**) favors an ion population composed exclusively of extended conformers; however, CCS profiles collected at progressively lower T_{eff} (going down each column) contain partially resolved conformers or conformer families that are relatively compact. It is interesting to note that the CCS profile for apoMT remains highly heterogeneous at the lowest T_{eff}, which is further evidence that the protein is indeed best described as an IDP. Similar broad, multi-component CCS profiles are observed for the partially metalated ions, especially for i = 1 – 5. We note that the CCS transition collected using the lowest T_{eff} (row (**e**)) corresponds to a transition from disordered to ordered conformation, which is consistent with solution studies.[2,9,11] That is, as the number of Cd^{2+} ions increases there

are significant changes in the CCS profiles owing to diminution in the conformer population as well as shift to small values in their respective CCS. On the other hand, the effect of binding of metal ions on changes in T_{eff} can be seen by comparing the CCS transition between each column, *viz.* as i increases, greater T_{eff} (greater energy input) is required to unfold Cd_iMT.

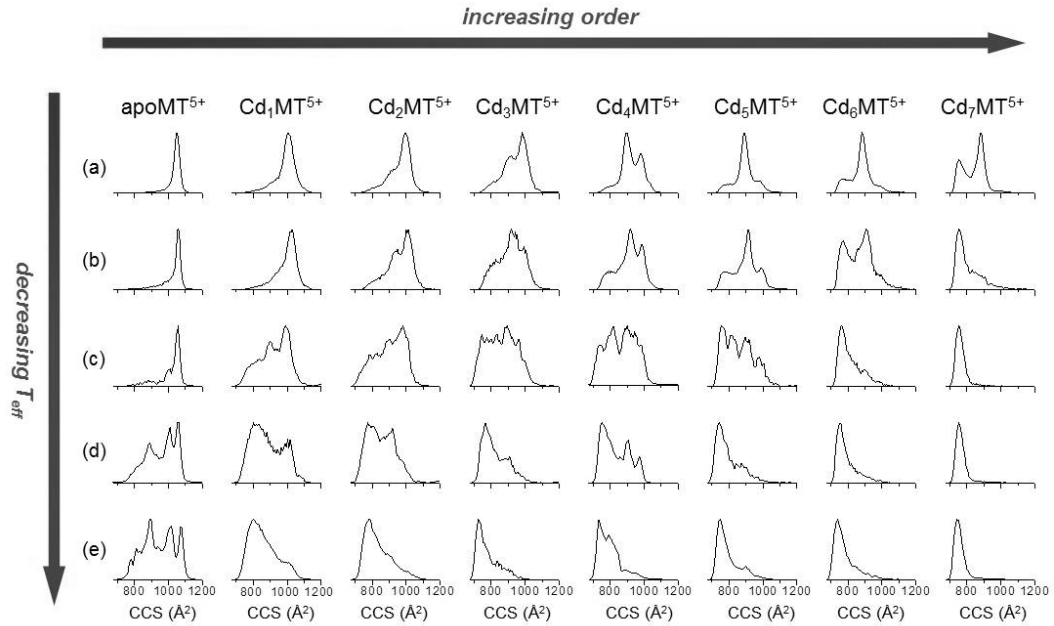

Figure 5.5. Ion mobility profiles of Cd_iMT (i = 0 − 7) acquired under various instrument conditions. The voltages of sampling cone (SC), extraction cone (EC), trap bias (TB), and flow of He and IMS cell were: (a) 60V, 4V, 45V, 180 and 90 mL/min, (b) 10V, 1V, 45V, 180 and 90 mL/min, (c) 10V, 1V, 35V, 180 and 90 mL/min, (d) 10V, 1V, 35V, 180 and 70 mL/min, and (e) 10V, 1V, 35V, 200 and 70 mL/min, respectively.

MD simulation of ubiquitin and Cd_iMT (i = 0 – 7)

Implicit water and *in vacuo* MD simulations were used to generate candidate conformations of ubq^{6+} and apo-, partially- and fully-metalated MT ions. Solution-phase structures are then subjected to *in vacuo* energy minimization to generate dehydrated structures.[45,58,66,160] Simulations for 300 K gas phase and dehydrated ubq^{6+} ions over a 10-ns window yield globular conformations (**Figure 5.6**). The dehydrated ions retain solution-phase secondary structure elements, whereas the secondary structure elements of the gas phase ions are disrupted. That is, a higher degree of helix and β-sheet structure is retained in the dehydrated conformers than is observed for the gas-phase ions (see **Figure 5.6**). Regardless, the average CCS of the gas- and solution-phase conformers are quite similar, 921.7 ± 6.1 $Å^2$ and 934.0 ± 10.1 $Å^2$, respectively, and both are in reasonable agreement with the experimental value for the compact **C** conformers.

Temperature-dependent conformations for solution and *in vacuo* simulations of ubq^{6+} ions are shown in **Figure 5.7(a)** and **(b)**, respectively. The solution simulations were designed to mimic heating that occurs during the droplet evaporation accompanying ESI (**Figure 5.7(a)**), *viz.* the solution transitions from ~ 300 K to a temperature of ~ 425 K; however, the simulations do not account for the evaporative cooling that may accompany droplet evaporation.[192] The calculated CCS for the dehydrated structures over the range of temperatures from 300 K to ~ 375 K fall within the range of the compact conformer **C** (~ 950 $Å^2$), and as the temperature is increased the CCS transition through **I** (~ 1200 $Å^2$) and eventually to **E** (~ 1500 $Å^2$).

Figure 5.7(b) contains similar data for gas phase unfolding in a solvent-free environment, *viz.* representative of ion heating in late stages of ESI as well as any changes in T_{eff} as the ions traverse the regions of the instrument that guide the ions to the TW analyzer. Note that ions from gas phase unfolding have a very different dependence on T_{eff} than do the solution phase ions. As temperature increases from ~300 K to 500 K, the protein undergoes some compaction with a small loss of 2^o structure elements, but the changes in CCS are small, ~ 3%. Further increase in T_{eff} (> 600 K) results in complete loss of 2^o structure elements resulting in formation of largely disordered conformations. Specifically, the T_{eff} range for unfolding gas phase ions is much larger than that for solution phase ions, and the range of CCS is also much larger for gas phase ions.

The gas phase, hydrated, and dehydrated candidate structures for the various Cd_iMT species were generated as described above for ubiquitin.[65] Unlike ubiquitin, MT is disordered in solution thus the structural evolution at fixed temperatures was evaluated. **Figure 5.8** shows the time-dependent CCS and representative conformations for dehydrated Cd_iMTs at temperatures 300, 350, and 400 K. The simulation data show a good agreement with the experimental CCS and both of them suggest that (i) at 300 K the protein disorder decreases as the numbers of Cd^{2+} ions bound increases, (ii) the protein unfolds as temperature increases independent of the numbers of Cd^{2+} ions bound, and (iii) the transition in CCS for apoMT (disordered protein) is much more sensitive to temperature compared to that of Cd_7MT (ordered protein). For example, at 300 − 350 K a sharp transition from the compact conformer (CCS ~ 890 $Å^2$) to a partially-unfolded

conformer (CCS ~ 1100 − 1200 $Å^2$) is evident for i = 0 – 2, but similar transitions are less apparent for the i = 3 – 7 ions; however, there is an overall increase in CCS as temperature increases. Simulation data for the gas phase Cd_iMT are provided in **Figure 5.9**, and these data clearly show similar unfolding transition as the temperature increases.

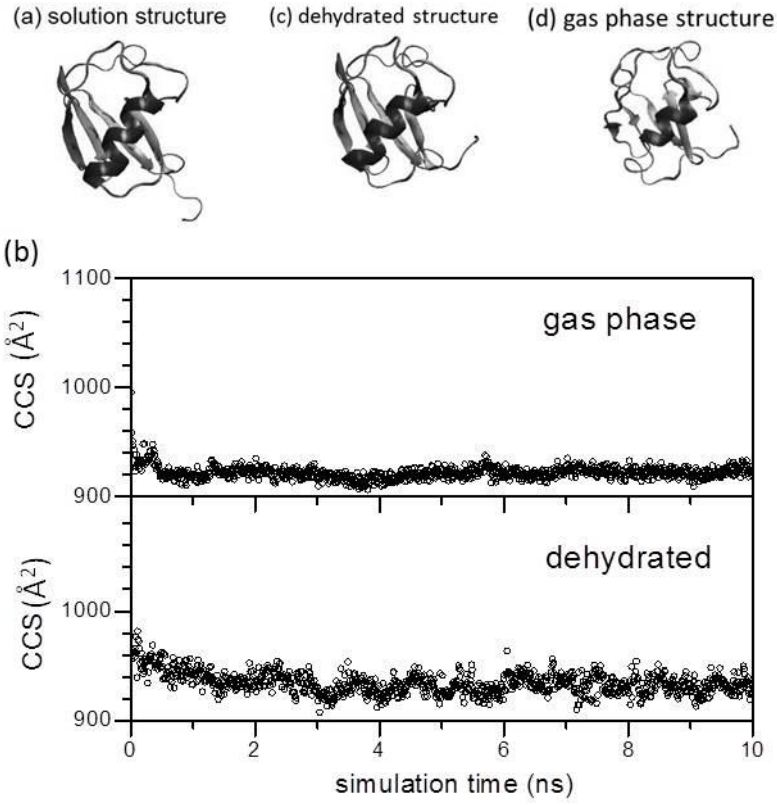

Figure 5.6. MD simulation of ubiquitin at 300 K. (a) NMR solution structure (1D3Z) was used as initial structure for simulation. (b) 10ns-MD simulations of dehydrated (blue) and gas phase (black) ubiquitin. The data show that for both cases, the simulation assumes compact conformations with an average CCS of 934 ± 10.1 and 922 ± 6.1 $Å^2$ for dehydrated and gas phase structures, respectively. The representative dehydrated and gas phase structures derived from the simulations are shown in (c) and (d), respectively.

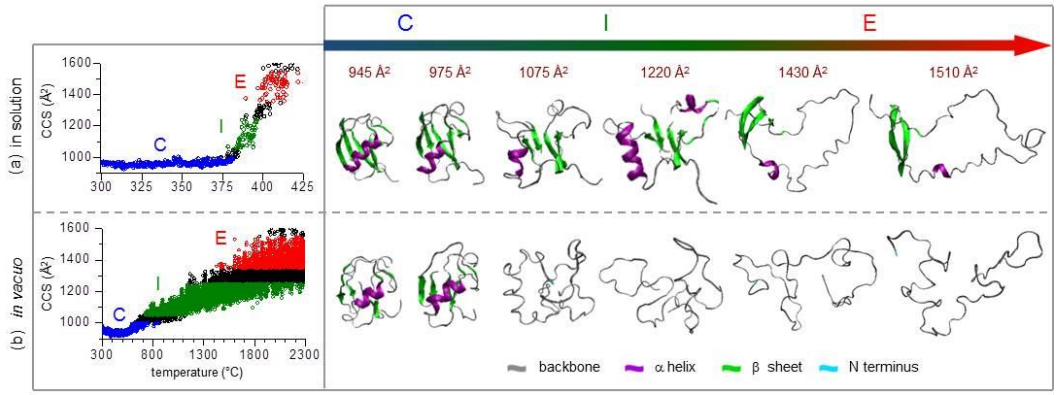

Figure 5.7. Simulations of effect of temperature on (a) dehydrated and (b) gas phase ubiquitin structure. Dehydrated structures are generated by *in vacuo* minimization of solution structures that underwent thermal unfolding in the presence of water; gas phase structures are simulated in the absence of water.

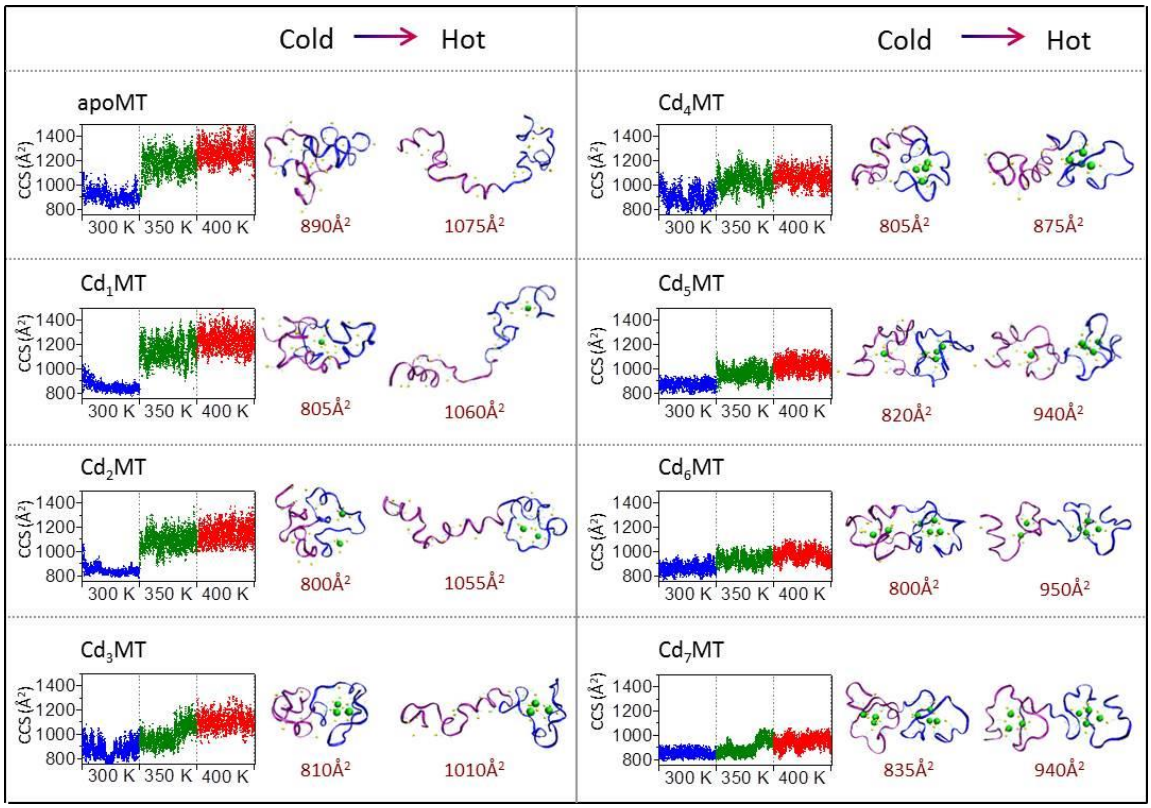

Figure 5.8. MD simulations of dehydrated Cd_iMT (i = 0 – 7) at temperatures of 300, 350, and 400 K. The time window for each temperature is 5 ns.

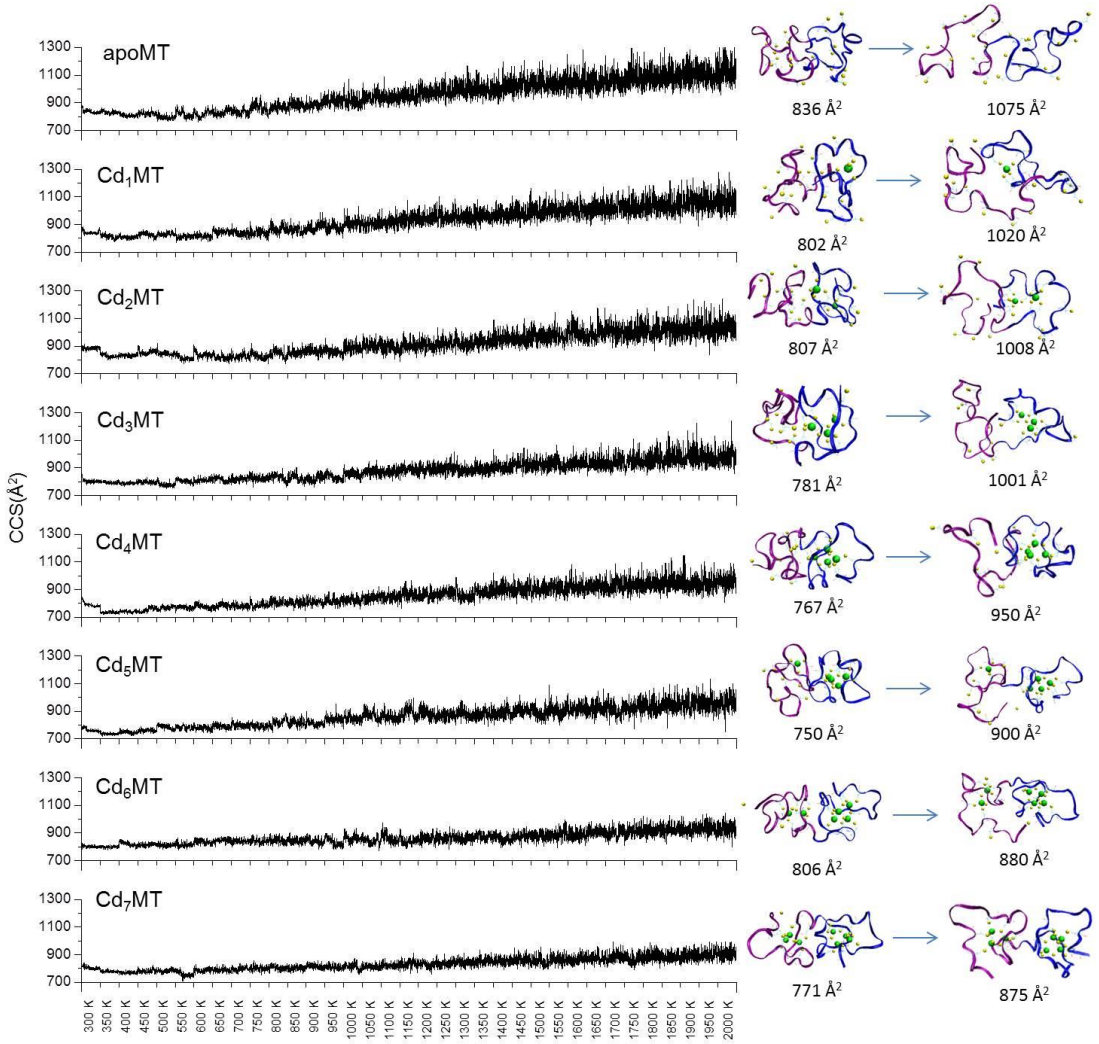

Figure 5.9. MD simulations for the effect of temperature on gas phase Cd_iMT structures. The simulation data show that irrespective of the number of metal ions bound, the protein unfolds as temperature increases; however, the unfolding proceeds much slower as the number of metal ions increase, consistent with the experimental data.

Discussion

Heck defines "native-state ESI" as the ability to retain quaternary structure of the biomolecule complex,[52] and Ruotolo's studies on the collision-induced unfolding (CIU)

of small molecules bound to proteins and protein complexes provide additional support for Heck's definition.[200] That is, at low T_{eff} the complexes have smaller CCSs than do complexes that have been subjected to CIU. Similarly, the experimental CCS profiles for ubq^{6+} and Cd_iMT^{5+} (i = 0 − 7) ions produced by using native-ESI conditions and then examined at the lowest possible T_{eff} by IM-MS have CCSs that agree with those for solution-phase structures. When these same ions are sampled using conditions corresponding to increased T_{eff}, which promote unfolding of the gas-phase ions, their CCSs are in excellent agreement with CCSs for candidate structures obtained from the temperature-ramped MD simulations.

The data for ubq^{6+} and Cd_iMT^{5+} clearly show changes in the conformer distributions as the solvent-free ions traverse the instrument between the ESI source and the TW analyzer. Although it is possible that the conformational dynamics are the result of slow gas phase refolding processes,[152,201] the CCS profiles for ions that have the lowest T_{eff} (**Figure 5.2**, columns 1 and 2, row (f)) clearly show that these ions have CCSs that resemble to the native fold, suggesting that they do not unfold between ion formation and sampling by the TW analyzer. The CCS profile for these lowest T_{eff} ions is good evidence that the ESI conditions used for this study produce an ion population that is primarily "native". Note the CCS for **C** is in excellent agreement with that of the "native-state" CCS for the NMR structure (see **Figure 5.6**) and that reported by both Clemmer and Bowers.[194,196] Thus, changes in the conformer distribution that are reflected by changes in the CCS profiles must be related to changes in T_{eff} that occur post-ESI, *viz.* energetic ion-neutral collisions as the ions are guided by focusing devices

from the ion source to the TW analyzer. Previous studies by Williams and DePauw clearly show that the T_{eff} of small thermometer ions are sensitive to the TW velocity and amplitude;[202-204] however, the CCS profiles for the protein ions studied here do not show significant dependence on the tuning of the TW analyzer (see **Figure 5.10**). The differences between small and large molecule ions may be attributed to the number of degrees-of-freedom into which energy can be channeled,[205] thus, the effects of changes in T_{eff} are expected to be much less for large molecule ions. Although our data clearly show that SC, EC, TB and He and N_2 flow rates have marked effects on T_{eff} for protein ions, we do not find any evidence that ion source temperature or tuning of the TW Trap ion guide (flow rate of Ar and wave height and velocity) have any significant effects on T_{eff}.

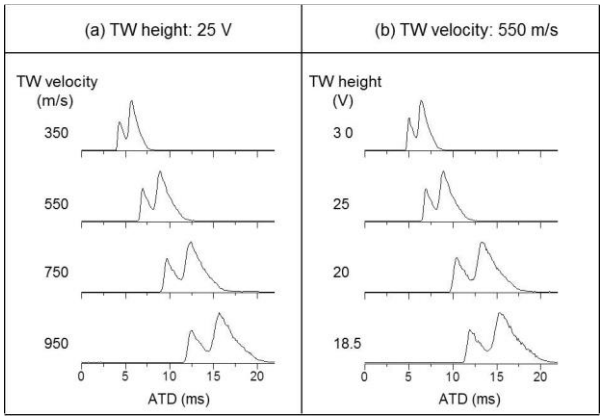

Figure 5.10. Ion mobility data for ubq^{6+} recorded under various TW conditions: (a) TW height is fixed at 25 V when TW velocity varies from 350 – 950 m/s; (b) TW velocity is fixed at 550 m/s when TW height varies from 30 – 18.5 V. Other instrumental parameters were maintained as follows: sampling cone (SC) 10 V, extraction cone (EC) 1V, trap bias (TB) 35 V, He gas flow 180 mL/min and IMS gas flow 70 mL/min. The data suggest that varying the TW height and velocity do not cause observable protein conformational change.

The temperature map that is superimposed on the ubq^{6+} ion CCS profiles clearly shows that changes in SC, EC, TB, and He flow shift the conformer preferences from **E** → **I** → **C** as ions having lower T_{eff} are sampled. Note that the decrease in these potentials and increase in the flow rate of He significantly reduce the kinetic energy of ions before they enter the IMS (N_2) cell thereby resulting in decreases in T_{eff}. The overall trends in the data indicate that the *ion population generated by "native-state ESI" can be preserved under conditions of low* T_{eff}. The temperature map also illustrates a complex interplay between T_{eff} and the N_2 gas flow rate within the TW analyzer, *viz.* the distribution of conformers can be altered by energetic collisions that occur within the TW analyzer. *The CCS profiles in the first column of the temperature map (**Figure 5.2**) are a direct measure of the conformer distribution as it enters the TW analyzer, and any changes in the conformer distribution that arise as the* N_2 *gas flow rate is decreased is a result of cooling/heating by collisions in the TW analyzer.* For example, row (**a**) shows the results of cooling the ion population introduced to the TW analyzer by using the manufacturer's "default" settings for SC, EC and TB. Reducing the N_2 flow rate is accompanied by a decrease in the relative abundance of **E** and a corresponding increase in **I** owing to a reduction in T_{eff}. At the other extreme, row (**f**), the initial ion population is composed primarily of "native" state ubq^{6+} ions, and decrease in the N_2 flow rate results in an increased abundance of higher energy conformers owing to increased T_{eff} relative to the initial T_{eff} for the ions that enter the TW analyzer. In summary, ions entering the TW analyzer with high T_{eff} are cooled as the ratio of N_2 is reduced, whereas ions entering the TW with low T_{eff} are heated under these same conditions. The data in

rows (**b**) − (**e**) show that under these conditions T_{eff} initially decreases and then increases. Note that the CCS profiles along the diagonal from *bottom-left* to *top-right appear to correspond to tuning conditions that favor the lowest T_{eff} for each row (**Figure 5.2**).* This observation raises important questions---*why does the flow rate of N_2 have such a dramatic effect on conformer distribution--- how do decreases of N_2 flow achieve opposite effects (cooling or heating) that are dependent on initial conditions?* First, using high flow rates of N_2 the He leak rate (into N_2 TW cell) will be small, but it will increase as the N_2 flow rate is reduced. Under the conditions the flow of N_2 is reduced, the ratio of He/N_2 in the TW analyzer increases, and the increased partial pressure of the lighter collision partner (He) reduces energy transfer by the ion-neutral collisions.[205] Second, the mean-free-path of ions within the IMS cell increases as the flow of N_2 is reduced, thus increasing the kinetic energy gained by each collision event. Note that the combination of these two effects determines the T_{eff} of the ions. In our experiments, using strong ion focusing conditions (row (**a**)) ions acquire substantial kinetic energy prior entering to the IMS cell and this large kinetic energy is converted into internal vibrational energy or T_{eff} by energetic collisions at the entrance of the IMS cell and dominates the overall T_{eff} of the ions; however, the ions are cooled as the ratio of He/N_2 increases (N_2 is varied from 90 – 40 mg/mL). In cases of low electric fields (row (**f**)) where ions do not acquire appreciable amounts of kinetic energy prior to entering the IMS cell, the increase in T_{eff} at the entrance of the TW analyzer is expected relatively small, thus the overall T_{eff} is dominated by the slow heating *within* the IMS cell. Lastly,

the changes of T_{eff} at the intermediate electric fields (row (**d**)) are governed by both factors.

Unlike ubiquitin, apoMT is disordered in solution, but the effects of changes in T_{eff} are quite similar. That is, the CCS profiles for $apoMT^{5+}$ (first column of **Figure 5.5**) clearly show that an extended conformation is favored at the highest T_{eff}; however, decreasing T_{eff} (top-to-bottom, first column) shifts the CCS profile and produces partially resolved peaks, indicative of an ion population that is composed of multiple conformer families. In addition, the CCS profiles for the partially- and fully-metalated Cd_iMT ions are shifted owing to a higher degree of order as metal ions are added. The increased conformational order is a direct result of strong metal-thiolate binding that stabilizes the protein structure. For example, the CCS profile for the highly ordered Cd_7MT^{5+} ion is multi-component even at high T_{eff}, but it eventually converges to a single compact conformer (bottom row of column 8). Similar trends are also observed for all the apo- and partially-metalated forms.

Although all of the Cd_iMT^{5+} ions unfold as T_{eff} is increased, their T_{eff}-dependent unfolding is quite different. For example, Cd_7MT^{5+} maintains the native-like fold at medium T_{eff} (condition c) but under the same conditions the $apoMT^{5+}$ is significantly activated and composed of a single elongated conformation (**Figure 5.5**). This differential T_{eff}-dependent unfolding observed for $apoMT^{5+}$ and Cd_iMT^{5+} ions is attributed to differing degrees of stabilization by intramolecular interaction, *i.e.*, the presence of strong metal-thiolate interaction introduced by the binding of metal ion makes protein ions more resistant to ion heating.

There are two potential approaches that can be used to probe folding/unfolding pathways of gas phase ions as a function of T_{eff} and or time: (i) IM-MS[195,206-207] and (ii) electron-capture dissociation (ECD) combined with hydrogen/deuterium exchange (HDX).[165,201,208] Here, MD simulations are used to generate T_{eff}-dependent conformer preferences.[209-210] The data contained in **Figure 5.7** illustrate that ion heating in water and in the gas phase gradually depletes the protein 2° and 3° structures, and these processes form multiple intermediates that involve formation of the elongated conformers. However, the unfolding pathways are distinct between the two models: (i) the partially unfolded **I** conformers differ significantly, *viz.* the dehydrated structures retain the 2° structures of the native fold for a longer period of time, whereas these interactions are disrupted very quickly for the gas-phase ions; (ii) the unfolding in gas phase ions proceeds much more slowly and results in a much broader dispersion in CCS, probably owing to the strong intramolecular electrostatic interaction (charge solvation) in the absence of water.

The simulated T_{eff}-dependent conformer preferences are consistent with the experimental data. That is, a structural transition from compact to extended conformations is observed for both ubq^{6+} and Cd_iMT^{5+} ions; however, it should be noted that the simulation data presented here only represent possible unfolding pathways and there are many possible parallel pathways to the energetically accessible unfolded states.[165,208]

The T_{eff}-dependent conformational changes provide important insights into the protein energy folding landscape. To date, very little is known about the effects of

metalation on folding/unfolding of metalloproteins.[9] The solution phase-like conformational landscape is best represented by the CCS data collected with minimal energy perturbation. For example, the CCS data for apoMT is consistent with that of an intrinsically disordered protein (IDP), *i.e.,* an energy folding landscape composed of multiple energy minima. Addition of metal ions converge the distinct conformation to a narrow CCS profile that can be correlated to changes in the folding landscape, *i.e.*, metal binding induces new structural domains thereby reducing the flexibility of specific domains of the molecule. Such changes result in narrowing of the conformational space and deepening of the funnel-shaped landscape. As the number of metal ions bound increases, the depth of the funnel increases, in line with the T_{eff} data shown in **Figure 5.5**. For example, the CCS profile for Cd_7MT^{5+} appears to be unchanged over the range of conditions used to acquire (c) − (e); however, that of $apoMT^{5+}$ has changed dramatically when the same range of conditions is used. Similarly, the T_{eff} data for the partially metalated ions, Cd_iMT^{5+} i = 1 – 6, that are "trapped" in local minima, *i.e.*, initially sampled at either low or high T_{eff}, corresponding to (a) or (e), respectively, can sample the landscape provided sufficient energy, thus changes in T_{eff} coupled with IMS can be used to map the energy folding landscape as a function of degree of metalation.

Conclusion

"Native mass spectrometry" is emerging as a powerful technology in structural biology and experimental parameters that most strongly affect "Native ESI" are now quite well defined;[52] however, the question how "native" are ions sampled by the IMS

experiment remains elusive. That is, there is considerable time lag (10-100 μs) between ion formation and ions entering the IMS analyzer, and the ions can unfold/refold on this time scale.[152] Also, collisional activation can occur as ions are guided/focused by electrostatic lens and ion-neutral collision as they travel from the ions source to the IMS analyzer, and T_{eff} can also be increased by black-body irradiation from their surroundings.[211] Clearly, increases in T_{eff} influences protein conformation, thus *to what extent does the journey from source to IMS analyzer influence conformer preferences of large molecule ions, how do these effects influence IMS data, and most importantly, can we correlate "native" and "non-native" states sampled by IM-MS to solution "native" conformation*?

Here, we clearly show that IMS CCS profiles do not always retain the structural feature for the "native" structure when the ions are formed using "native-ESI" conditions. In cases of large proteins or protein complexes, the available experimental data support the claims that solution phase structural features are retained; however, TW IMS studies for ubq^{6+} ions and drift tube IMS for $apoMT^{5+}$ [154] show that they adopt extended conformations[204] that differ significantly from the native-like state; however, data shown in the current study clearly show that under conditions that minimize T_{eff}, CCS profiles are consistent with the results reported by solution studies, for both ordered (ubiquitin, Cd_7MT) and disordered (apoMT) proteins.

This study serves as a cautionary note for interpreting structural information and careful evaluation of the experimental IM-MS parameters prior to assignments of ion conformation. In these studies the conformational changes associated with 2^o and 3^o

structure that are occurring as the ions traverse the instrument are derived from cumulative effects of individual ion focusing optics. On the other hand, the data suggest that careful tuning of instrumental parameters allows preservation of native-like conformation. This study also helps to define specific tuning guidelines that achieve low T_{eff} for the most widely used IM-MS instrument for protein structure and structural biology.

CHAPTER VI

CONCLUSIONS

Summary

Since the discovery of MT in 1957, MTs have been received consistent attention in all aspects. Up to now, > 10,000 research articles have been retrieved from Pubmed on MT research. Although extensively studied, the fundamental understanding about chemistry of MT-metal ion interaction has not been fully established and there remain many unanswered questions.

ESI-MS has been used in previous studies of MTs, but the experimental approaches used in this work reveal new insights regarding metalated/demetalated intermediates and reaction mechanism. Direct sequencing of the partially-metalated intermediates in the metalation/demetalation reactions provides unambiguous identification of the site-specific information regarding the mechanism of metalation/demetalation, demonstrating that the binding of metal ion is domain-specific, *ie.* the α domain is formed before the β domain. The relative metal ion-binding affinity for individual partially-metalated intermediates provides direct evidence that the Cd^{2+} ion binding to MT is cooperative. That is, an increased metal ion affinity was observed to saturation of the α-domain and that of both (α- and β-) domains. The reverse reactions, demetalation by EDTA or metal-ion displacement by NEM, are also cooperative. The stable intermediates contain Cd_4α-domain in both metalation and

demetalation reactions, indicative of a greater thermodynamic and kinetic stability for the α domain than that the β domain.

The competition of cysteine binding sites between NEM and Cd^{2+} ions provides information about kinetically labile Cd^{2+}-S bonds. The stable partially-alkylated metal-remaining intermediate contains the alkylation of the nine cysteines in the β domain as well as Cys33 reveals a weakly-coordinated site in the α-domain. Although the biological role of Cys33 has not been identified, the data provide a direct evidence for a existence of a weakly binding site in the α domain and suggest that the contribution of an individual cysteine to the structure and function of MT is not equal.

Ion mobility data and MD simulations provide information regarding the conformational population and protein folding energy landscape for apo-, partially-, and fully-metalated MTs. The data for the Cd_iMT (i = 0 – 7) ions reveal a diverse population of ion conformations. In case of apoMT, the data is consistent with is consistent with kinetic trapping of an ion population composed of a wide range of conformers, *i.e.*, an energy folding landscape composed of multiple energy minima. Upon metal-ion binding, the conformational diversity for apoMT and partially-metalated ions converge toward ordered, compact conformations as the number of bound Cd^{2+} ions increase. The data is viewed as an evidence for a disordered-to-ordered conformational transition upon binding of metal ions.

To our best knowledge, our study is the first report identifying metal-binding sites of intact partially-metalated intermediate MT directly. The relative binding affinity between each metalated form was also resolved for the first time. We also showed the

first experimental data for conformational population of each of the metalated forms, which provides a global and dynamic view that shows stepwise metal-induced conformational transition of an ensemble in terms of their 3° and 4° structure. The knowledge provided here provides new insights related to the metalation/demetalation of MT, leading to a better understanding of structure-function relationships.

Future Directions

The work presented here provides a better understanding of the underlying metal-binding mechanism and structure-function relationship of MTs. On the other hand, it also raises as many questions as it has answered. For example, the distinct properties between α and β domain presented here imply the different biological function of the two domains: one is regulatory domain and the other one is detoxification domain. The domains seem to act independently, then why does MT evolve to a two-domain structure? Is there a domain-domain interaction? Does the intra-domain linker (K31-K32) play a role in intra-domain interaction? A follow-up study on individual domains will be needed to answer these questions. Besides, metalated MT is a fairly small protein held by two tight metal-thiolate clusters. Is there any critical cysteine that can alter the functions and structure of MT dramatically? The reaction with NEM suggests that Cys33 is less involved in the metal-thiolate cluster. What is the possible role of Cys33? A series of mutants with single cysteine replacements and integrated mass spectrometry-based approaches will find answers to these questions.

REFERENCES

1. Margoshes, M.; Vallee, B. L. A cadmium protein from equine kidney cortex. *J. Am. Chem. Soc.* **1957**, *79*, 4813-4814.
2. Romero-Isart, N.; Vasak, M. Advances in the structure and chemistry of metallothioneins. *J. Inorg. Biochem.* **2002**, *88*, 388-396.
3. Henkel, G.; Krebs, B. Metallothioneins: Zinc, cadmium, mercury, and copper thiolates and selenolates mimicking protein active site features--structural aspects and biological implications. *Chem. Rev.* **2004**, *104*, 801-824.
4. Coyle, P.; Philcox, J. C.; Carey, L. C.; Rofe, A. M. Metallothionein: The multipurpose protein. *Cell. Mol. Life Sci.* **2002**, *59*, 627-647.
5. Kagi, J. H.; Vallee, B. L. Metallothionein: A cadmium and zinc-containign protein from equine renal cortex. II. Physico-chemical properties. *J. Biol. Chem.* **1961**, *236*, 2435-2442.
6. *Metal ions in life sciences: Metallothioneins and related chelators*; Sigel, A.; Sigel, H.; Sigel, R. K. O., Eds.; Royal Society of Chemistry: Cambridge, UK, 2009.
7. *Metallothionein IV*; Klaassen, C., Ed.; Birkhäuser Verlag: Basel, Switzerland, 1999.
8. Klaassen, C. D.; Liu, J.; Choudhuri, S. Metallothionein: An intracellular protein to protect against cadmium toxicity. *Annu. Rev. Pharmacol. Toxicol.* **1999**, *39*, 267-294.

9. Blindauer, C. A.; Leszczyszyn, O. I. Metallothioneins: Unparalleled diversity in structures and functions for metal ion homeostasis and more. *Nat. Prod. Rep.* **2010**, *27*, 720-741.

10. de Bie, P.; Muller, P.; Wijmenga, C.; Klomp, L. W. Molecular pathogenesis of Wilson and Menkes disease: Correlation of mutations with molecular defects and disease phenotypes. *J. Med. Genet.* **2007**, *44*, 673-688.

11. Maret, W. Redox biochemistry of mammalian metallothioneins. *J. Biol. Inorg. Chem.* **2011**, *16*, 1079-1086.

12. Namdarghanbari, M.; Wobig, W.; Krezoski, S.; Tabatabai, N. M.; Petering, D. H. Mammalian metallothionein in toxicology, cancer, and cancer chemotherapy. *J. Biol. Inorg. Chem.* **2011**, *16*, 1087-1101.

13. Maret, W.; Vallee, B. L. Thiolate ligands in metallothionein confer redox activity on zinc clusters. *Proc. Natl. Acad. Sc.i USA* **1998**, *95*, 3478-3482.

14. Meloni, G.; Faller, P.; Vasak, M. Redox silencing of copper in metal-linked neurodegenerative disorders: Reaction of Zn_7metallothionein-3 with Cu^{2+} ions. *J. Biol. Chem.* **2007**, *282*, 16068-16078.

15. Meloni, G.; Sonois, V.; Delaine, T.; Guilloreau, L.; Gillet, A.; Teissie, J.; Faller, P.; Vasak, M. Metal swap between Zn_7-metallothionein-3 and amyloid-beta-Cu protects against amyloid-beta toxicity. *Nat. Chem. Biol.* **2008**, *4*, 366-372.

16. Howells, C.; West, A. K.; Chung, R. S. Neuronal growth-inhibitory factor (metallothionein-3): Evaluation of the biological function of growth-inhibitory factor in the injured and neurodegenerative brain. *FEBS J.* **2010**, *277*, 2931-2939.

17. Chung, R. S.; Howells, C.; Eaton, E. D.; Shabala, L.; Zovo, K.; Palumaa, P.; Sillard, R.; Woodhouse, A.; Bennett, W. R.; Ray, S.; Vickers, J. C.; West, A. K. The native copper- and zinc-binding protein metallothionein blocks copper-mediated Abeta aggregation and toxicity in rat cortical neurons. *PloS one* **2010**, *5*, e12030.

18. Frederickson, C. J.; Koh, J. Y.; Bush, A. I. The neurobiology of zinc in health and disease. *Nat. Rev. Neurosci.* **2005**, *6*, 449-462.

19. Barnham, K. J.; Bush, A. I. Metals in Alzheimer's and Parkinson's diseases. *Curr. Opin. Chem. Biol.* **2008**, *12*, 222-228.

20. Sensi, S. L.; Paoletti, P.; Bush, A. I.; Sekler, I. Zinc in the physiology and pathology of the CNS. *Nat. Rev. Neurosci.* **2009**, *10*, 780-791.

21. Eckschlager, T.; Adam, V.; Hrabeta, J.; Figova, K.; Kizek, R. Metallothioneins and cancer. *Curr. Protein Pept. Sci.* **2009**, *10*, 360-375.

22. Jin, R.; Chow, V. T.; Tan, P. H.; Dheen, S. T.; Duan, W.; Bay, B. H. Metallothionein 2A expression is associated with cell proliferation in breast cancer. *Carcinogenesis* **2002**, *23*, 81-86.

23. Pattanaik, A.; Shaw, C. F., 3rd; Petering, D. H.; Garvey, J.; Kraker, A. J. Basal metallothionein in tumors: Widespread presence of apoprotein. *J. Inorg. Biochem.* **1994**, *54*, 91-105.

24. Yang, Y.; Maret, W.; Vallee, B. L. Differential fluorescence labeling of cysteinyl clusters uncovers high tissue levels of thionein. *Proc. Natl. Acad. Sci. USA* **2001**, *98*, 5556-5559.

25. Petering, D. H.; Zhu, J.; Krezoski, S.; Meeusen, J.; Kiekenbush, C.; Krull, S.; Specher, T.; Dughish, M. Apo-metallothionein emerging as a major player in the cellular activities of metallothionein. *Exp. Biol. Med.* **2006**, *231*, 1528-1534.

26. Jacob, C.; Maret, W.; Vallee, B. L. Control of zinc transfer between thionein, metallothionein, and zinc proteins. *Proc. Natl. Acad. Sc.i USA* **1998**, *95*, 3489-3494.

27. Maret, W.; Jacob, C.; Vallee, B. L.; Fischer, E. H. Inhibitory sites in enzymes: Zinc removal and reactivation by thionein. *Proc. Natl. Acad. Sci. USA* **1999**, *96*, 1936-1940.

28. Andrews, G. K. Regulation of metallothionein gene expression by oxidative stress and metal ions. *Biochem. Pharmacol.* **2000**, *59*, 95-104.

29. Kelley, S. L.; Basu, A.; Teicher, B. A.; Hacker, M. P.; Hamer, D. H.; Lazo, J. S. Overexpression of metallothionein confers resistance to anticancer drugs. *Science* **1988**, *241*, 1813-1815.

30. Naganuma, A.; Satoh, M.; Imura, N. Prevention of lethal and renal toxicity of cis-diamminedichloroplatinum(II) by induction of metallothionein synthesis without compromising its antitumor activity in mice. *Cancer Res.* **1987**, *47*, 983-987.

31. Vasak, M.; Kagi, J. H.; Hill, H. A. Zinc(II), cadmium(II), and mercury(II) thiolate transitions in metallothionein. *Biochemistry* **1981**, *20*, 2852-2856.

32. Rupp, H.; Weser, U. Circular dichroism of metallothioneins: A structural approach. *Biochim. Biophys. Acta* **1978**, *533*, 209-226.

33. Ejnik, J.; Robinson, J.; Zhu, J.; Forsterling, H.; Shaw, C. F.; Petering, D. H. Folding pathway of apo-metallothionein induced by Zn^{2+}, Cd^{2+} and Co^{2+}. *J. Inorg. Biochem.* **2002**, *88*, 144-152.

34. Robbins, A. H.; McRee, D. E.; Williamson, M.; Collett, S. A.; Xuong, N. H.; Furey, W. F.; Wang, B. C.; Stout, C. D. Refined crystal structure of Cd, Zn metallothionein at 2.0 A resolution. *J. Mol. Biol.* **1991**, *221*, 1269-1293.

35. Schultze, P.; Worgotter, E.; Braun, W.; Wagner, G.; Vasak, M.; Kagi, J. H.; Wuthrich, K. Conformation of [Cd_7]-metallothionein-2 from rat liver in aqueous solution determined by nuclear magnetic resonance spectroscopy. *J. Mol. Biol.* **1988**, *203*, 251-268.

36. Arseniev, A.; Schultze, P.; Worgotter, E.; Braun, W.; Wagner, G.; Vasak, M.; Kagi, J. H.; Wuthrich, K. Three-dimensional structure of rabbit liver [Cd_7]metallothionein-2a in aqueous solution determined by nuclear magnetic resonance. *J. Mol. Biol.* **1988**, *201*, 637-657.

37. Messerle, B. A.; Schaffer, A.; Vasak, M.; Kagi, J. H.; Wuthrich, K. Three-dimensional structure of human [$^{113}Cd_7$]metallothionein-2 in solution determined by nuclear magnetic resonance spectroscopy. *J. Mol. Biol.* **1990**, *214*, 765-779.

38. Chait, B. T. Mass spectrometry: Bottom-up or top-down? *Science* **2006**, *314*, 65-66.

39. Bogdanov, B.; Smith, R. D. Proteomics by FTICR mass spectrometry: Top down and bottom up. *Mass Spectrom. Rev.* **2005**, *24*, 168-200.

40. Deng, L.; Sun, N.; Kitova, E. N.; Klassen, J. S. Direct quantification of protein-metal ion affinities by electrospray ionization mass spectrometry. *Anal. Chem.* **2010**, *82*, 2170-2174.

41. Loo, J. A. Studying noncovalent protein complexes by electrospray ionization mass spectrometry. *Mass Spectrom. Rev.* **1997**, *16*, 1-23.

42. Ruotolo, B. T.; Giles, K.; Campuzano, I.; Sandercock, A. M.; Bateman, R. H.; Robinson, C. V. Evidence for macromolecular protein rings in the absence of bulk water. *Science* **2005**, *310*, 1658-1661.

43. McKay, A. R.; Ruotolo, B. T.; Ilag, L. L.; Robinson, C. V. Mass measurements of increased accuracy resolve heterogeneous populations of intact ribosomes. *J. Am. Chem. Soc.* **2006**, *128*, 11433-11442.

44. Bleiholder, C.; Dupuis, N. F.; Wyttenbach, T.; Bowers, M. T. Ion mobility-mass spectrometry reveals a conformational conversion from random assembly to beta-sheet in amyloid fibril formation. *Nat. Chem.* **2011**, *3*, 172-177.

45. Dupuis, N. F.; Wu, C.; Shea, J. E.; Bowers, M. T. The amyloid formation mechanism in human IAPP: Dimers have beta-strand monomer-monomer interfaces. *J. Am. Chem. Soc.* **2011**, *133*, 7240-7243.

46. Yu, X.; Wojciechowski, M.; Fenselau, C. Assessment of metals in reconstituted metallothioneins by electrospray mass spectrometry. *Anal. Chem.* **1993**, *65*, 1355-1359.

47. Zaia, J.; Fabris, D.; Wei, D.; Karpel, R. L.; Fenselau, C. Monitoring metal ion flux in reactions of metallothionein and drug-modified metallothionein by electrospray mass spectrometry. *Protein Sci.* **1998**, *7*, 2398-2404.

48. Ngu, T. T.; Stillman, M. J. Arsenic binding to human metallothionein. *J. Am. Chem. Soc.* **2006**, *128*, 12473-12483.

49. Ngu, T. T.; Easton, A.; Stillman, M. J. Kinetic analysis of arsenic-metalation of human metallothionein: Significance of the two-domain structure. *J. Am. Chem. Soc.* **2008**, *130*, 17016-17028.

50. Polec Pawlak, K.; Palacios, O.; Capdevila, M.; Gonzalez-Duarte, P.; Lobinski, R. Monitoring of the metal displacement from the recombinant mouse liver metallothionein Zn_7-complex by capillary zone electrophoresis with electrospray MS detection. *Talanta* **2002**, *57*, 1011-1017.

51. Kaluarachchi, H.; Sutherland, D. E.; Young, A.; Pickering, I. J.; Stillman, M. J.; Zamble, D. B. The Ni(II)-binding properties of the metallochaperone SlyD. *J. Am. Chem. Soc.* **2009**, *131*, 18489-18500.

52. Heck, A. J. Native mass spectrometry: A bridge between interactomics and structural biology. *Nat. Methods* **2008**, *5*, 927-933.

53. Wales, T. E.; Engen, J. R. Hydrogen exchange mass spectrometry for the analysis of protein dynamics. *Mass Spectrom. Rev.* **2006**, *25*, 158-170.

54. D'Agostino, P. A.; Chenier, C. L. Desorption electrospray ionization mass spectrometric analysis of organophosphorus chemical warfare agents using ion

mobility and tandem mass spectrometry. *Rapid Commun. Mass Spectrom.* **2010**, *24*, 1617-1624.

55. Lanucara, F.; Holman, S. W.; Gray, C. J.; Eyers, C. E. The power of ion mobility-mass spectrometry for structural characterization and the study of conformational dynamics. *Nat. Chem.* **2014**, *6*, 281-294.

56. Clemmer, D. E.; Hudgins, R. R.; Jarrold, M. F. Naked protein conformations: Cytochrome c in the gas phase. *J. Am. Chem. Soc.* **1995**, *117*, 10141-10142.

57. Bernstein, S. L.; Dupuis, N. F.; Lazo, N. D.; Wyttenbach, T.; Condron, M. M.; Bitan, G.; Teplow, D. B.; Shea, J. E.; Ruotolo, B. T.; Robinson, C. V.; Bowers, M. T. Amyloid-beta protein oligomerization and the importance of tetramers and dodecamers in the aetiology of Alzheimer's disease. *Nat. Chem.* **2009**, *1*, 326-331.

58. Bernstein, S. L.; Liu, D.; Wyttenbach, T.; Bowers, M. T.; Lee, J. C.; Gray, H. B.; Winkler, J. R. Alpha-synuclein: Stable compact and extended monomeric structures and pH dependence of dimer formation. *J. Am. Soc. Mass Spectrom.* **2004**, *15*, 1435-1443.

59. Bernstein, S. L.; Wyttenbach, T.; Baumketner, A.; Shea, J. E.; Bitan, G.; Teplow, D. B.; Bowers, M. T. Amyloid beta-protein: Monomer structure and early aggregation states of Abeta42 and its Pro19 alloform. *J. Am. Chem. Soc.* **2005**, *127*, 2075-2084.

60. Canon, F.; Ballivian, R.; Chirot, F.; Antoine, R.; Sarni-Manchado, P.; Lemoine, J.; Dugourd, P. Folding of a salivary intrinsically disordered protein upon binding to tannins. *J. Am. Chem. Soc.* **2011**, *133*, 7847-7852.

61. Pagel, K.; Natan, E.; Hall, Z.; Fersht, A. R.; Robinson, C. V. Intrinsically disordered p53 and its complexes populate compact conformations in the gas phase. *Angew. Chem. Int. Ed. Engl.* **2013**, *52*, 361-365.

62. Jurneczko, E.; Cruickshank, F.; Porrini, M.; Clarke, D. J.; Campuzano, I. D.; Morris, M.; Nikolova, P. V.; Barran, P. E. Probing the conformational diversity of cancer-associated mutations in p53 with ion-mobility mass spectrometry. *Angew. Chem. Int. Ed. Engl.* **2013**, *52*, 4370-4374.

63. Saikusa, K.; Fuchigami, S.; Takahashi, K.; Asano, Y.; Nagadoi, A.; Tachiwana, H.; Kurumizaka, H.; Ikeguchi, M.; Nishimura, Y.; Akashi, S. Gas-phase structure of the histone multimers characterized by ion mobility mass spectrometry and molecular dynamics simulation. *Anal. Chem.* **2013**, *85*, 4165-4171.

64. Jurneczko, E.; Cruickshank, F.; Porrini, M.; Nikolova, P.; Campuzano, I. D.; Morris, M.; Barran, P. E. Intrinsic disorder in proteins: A challenge for (un)structural biology met by ion mobility-mass spectrometry. *Biochem. Soc. Trans.* **2012**, *40*, 1021-1026.

65. Chen, S.-H.; Chen, L.; Russell, D. H. Metal-induced conformational changes of human metallothionein-2A: A combined theoretical and experimental study of metal-free and partially metalated intermediates. *J. Am. Chem. Soc.* **2014**, *136*, 9499-9508.

66. Pierson, N. A.; Chen, L.; Valentine, S. J.; Russell, D. H.; Clemmer, D. E. Number of solution states of bradykinin from ion mobility and mass spectrometry measurements. *J. Am. Chem. Soc.* **2011**, *133*, 13810-13813.

67. Chen, L.; Chen, S.-H.; Russell, D. H. An experimental study of the solvent-dependent self-assembly/disassembly and conformer preferences of gramicidin A. *Anal. Chem.* **2013**, *85*, 7826-7833.

68. Nawrot, T.; Plusquin, M.; Hogervorst, J.; Roels, H. A.; Celis, H.; Thijs, L.; Vangronsveld, J.; Van Hecke, E.; Staessen, J. A. Environmental exposure to cadmium and risk of cancer: A prospective population-based study. *Lancet Oncol.* **2006**, *7*, 119-126.

69. Johnson, M. D.; Kenney, N.; Stoica, A.; Hilakivi-Clarke, L.; Singh, B.; Chepko, G.; Clarke, R.; Sholler, P. F.; Lirio, A. A.; Foss, C.; Reiter, R.; Trock, B.; Paik, S.; Martin, M. B. Cadmium mimics the *in vivo* effects of estrogen in the uterus and mammary gland. *Nat. Med.* **2003**, *9*, 1081-1084.

70. McMurray, C. T.; Tainer, J. A. Cancer, cadmium and genome integrity. *Nat. Genet.* **2003**, *34*, 239-241.

71. Hengstler, J. G.; Bolm-Audorff, U.; Faldum, A.; Janssen, K.; Reifenrath, M.; Gotte, W.; Jung, D.; Mayer-Popken, O.; Fuchs, J.; Gebhard, S.; Bienfait, H. G.; Schlink, K.; Dietrich, C.; Faust, D.; Epe, B.; Oesch, F. Occupational exposure to heavy metals: DNA damage induction and DNA repair inhibition prove co-exposures to cadmium, cobalt and lead as more dangerous than hitherto expected. *Carcinogenesis* **2003**, *24*, 63-73.

72. Vallee, B. L.; Ulmer, D. D. Biochemical effects of mercury, cadmium, and lead. *Annu. Rev. Biochem.* **1972**, *41*, 91-128.

73. Chan, J.; Huang, Z.; Merrifield, M. E.; Salgado, M. T.; Stillman, M. J. Studies of metal binding reactions in metallothioneins by spectroscopic, molecular biology, and molecular modeling techniques. *Coord. Chem. Rev.* **2002**, *233–234*, 319-339.

74. Stillman, M. J. Metallothioneins. *Coord. Chem. Rev.* **1995**, *144*, 461-511.

75. Li, Y.; Maret, W. Human metallothionein metallomics. *J. Anal. At. Spectrom.* **2008**, *23*, 1055-1062.

76. Jiang, D. T.; Heald, S. M.; Sham, T. K.; Stillman, M. J. Structures of the cadmium, mercury, and zinc thiolate clusters in metallothionein: XAFS study of Zn_7-MT, Cd_7-MT, Hg_7-MT, and Hg_{18}-MT formed from rabbit liver metallothionein 2. *J. Am. Chem. Soc.* **1994**, *116*, 11004-11013.

77. Zhang, Z.; Lindale, M. G.; Liebeskind, L. S. Mobilizing Cu(I) for carbon-carbon bond forming catalysis in the presence of thiolate. Chemical mimicking of metallothioneins. *J. Am. Chem. Soc.* **2011**, *133*, 6403-6410.

78. Krezel, A.; Maret, W. Dual nanomolar and picomolar Zn(II) binding properties of metallothionein. *J. Am. Chem. Soc.* **2007**, *129*, 10911-10921.

79. Lu, W.; Stillman, M. J. Mercury-thiolate clusters in metallothionein. Analysis of circular dichroism spectra of complexes formed between .alpha.-metallothionein, apometallothionein, zinc metallothionein, and cadmium metallothionein and mercury(2+). *J. Am. Chem. Soc.* **1993**, *115*, 3291-3299.

80. Li, T. Y.; Kraker, A. J.; Shaw, C. F., 3rd; Petering, D. H. Ligand substitution reactions of metallothioneins with EDTA and apo-carbonic anhydrase. *Proc. Natl. Acad. Sci. USA* **1980**, *77*, 6334-6338.

81. Gan, T.; Munoz, A.; Shaw, C. F., 3rd; Petering, D. H. Reaction of $^{111}Cd_7$-metallothionein with EDTA. A reappraisal. *J. Biol. Chem.* **1995**, *270*, 5339-5345.

82. Shaw Iii, C. F.; He, L.; Muñoz, A.; Savas, M. M.; Chi, S.; Fink, C. L.; Gan, T.; Petering, D. H. Kinetics of reversible N-ethylmaleimide alkylation of metallothionein and the subsequent metal release. *J. Biol. Inorg. Chem.* **1997**, *2*, 65-73.

83. Sutherland, D. E.; Willans, M. J.; Stillman, M. J. Single domain metallothioneins: Supermetalation of human MT 1a. *J. Am. Chem. Soc.* **2012**, *134*, 3290-3299.

84. Jensen, L. T.; Peltier, J. M.; Winge, D. R. Identification of a four copper folding intermediate in mammalian copper metallothionein by electrospray ionization mass spectrometry. *J. Biol. Inorg. Chem.* **1998**, *3*, 627-631.

85. Kagi, J. H.; Valee, B. L. Metallothionein: A cadmium- and zinc-containing protein from equine renal cortex. *J. Biol. Chem.* **1960**, *235*, 3460-3465.

86. Vasak, M.; Kagi, J. H. R. Spectroscopic properties of metallothionein. In *Met. Ions Biol. Syst.* ; Sigel, H., Ed.; Marcel Dekker: New York, Basel, 1983; Vol. 15, pp 213-273.

87. Wang, Y.; Mackay, E. A.; Kurasaki, M.; Kagi, J. H. Purification and characterisation of recombinant sea urchin metallothionein expressed in Escherichia coli. *Eur. J. Biochem.* **1994**, *225*, 449-457.

88. Konermann, L.; Simmons, D. A. Protein-folding kinetics and mechanisms studied by pulse-labeling and mass spectrometry. *Mass Spectrom. Rev.* **2003**, *22*, 1-26.

89. Norris, A. J.; Whitelegge, J. P.; Faull, K. F.; Toyokuni, T. Analysis of enzyme kinetics using electrospray ionization mass spectrometry and multiple reaction monitoring: Fucosyltransferase V. *Biochemistry* **2001**, *40*, 3774-3779.

90. Pacholarz, K. J.; Garlish, R. A.; Taylor, R. J.; Barran, P. E. Mass spectrometry based tools to investigate protein-ligand interactions for drug discovery. *Chem. Soc. Rev.* **2012**, *41*, 4335-4355.

91. Hathout, Y.; Fabris, D.; Fenselau, C. Stoichiometry in zinc ion transfer from metallothionein to zinc finger peptides. *Int. J. Mass Spectrom.* **2001**, *204*, 1-6.

92. Fabris, D.; Zaia, J.; Hathout, Y.; Fenselau, C. Retention of thiol protons in two classes of protein zinc ion coordination centers. *J. Am. Chem. Soc.* **1996**, *118*, 12242-12243.

93. Yu, X.; Wu, Z.; Fenselau, C. Covalent sequestration of melphalan by metallothionein and selective alkylation of cysteines. *Biochemistry* **1995**, *34*, 3377-3385.

94. Zaia, J.; Jiang, L.; Han, M. S.; Tabb, J. R.; Wu, Z.; Fabris, D.; Fenselau, C. A binding site for chlorambucil on metallothionein. *Biochemistry* **1996**, *35*, 2830-2835.

95. Wei, D.; Fabris, D.; Fenselau, C. Covalent sequestration of phosphoramide mustard by metallothionein--an *in vitro* study. *Drug Metab. Dispos.* **1999**, *27*, 786-791.

96. Shirran, S. L.; Barran, P. E. The use of ESI-MS to probe the binding of divalent cations to calmodulin. *J. Am. Soc. Mass. Spectrom.* **2009**, *20*, 1159-1171.

97. Mounicou, S.; Ouerdane, L.; L'Azou, B.; Passagne, I.; Ohayon-Courtes, C.; Szpunar, J.; Lobinski, R. Identification of metallothionein subisoforms in HPLC using accurate mass and online sequencing by electrospray hybrid linear ion trap-orbital ion trap mass spectrometry. *Anal. Chem.* **2010**, *82*, 6947-6957.

98. Pedrero, Z.; Ouerdane, L.; Mounicou, S.; Lobinski, R.; Monperrus, M.; Amouroux, D. Identification of mercury and other metals complexes with metallothioneins in dolphin liver by hydrophilic interaction liquid chromatography with the parallel detection by ICP MS and electrospray hybrid linear/orbital trap MS/MS. *Metallomics* **2012**, *4*, 473-479.

99. Blindauer, C. A.; Polfer, N. C.; Keiper, S. E.; Harrison, M. D.; Robinson, N. J.; Langridge-Smith, P. R.; Sadler, P. J. Inert site in a protein zinc cluster: Isotope exchange by high resolution mass spectrometry. *J. Am. Chem. Soc.* **2003**, *125*, 3226-3227.

100. Chan, J.; Huang, Z.; Watt, I.; Kille, P.; Stillman, M. Metallobiological necklaces: Mass spectrometric and molecular modeling study of metallation in concatenated domains of metallothionein. *Chem. Eur. J.* **2008**, *14*, 7579-7593.

101. Chan, J.; Huang, Z.; Watt, I.; Kille, P.; Stillman, M. J. Characterization of the conformational changes in recombinant human metallothioneins using ESI-MS and molecular modeling. *Can. J. Chem.* **2007**, *85*, 898-912.

102. Pearson, R. G. Hard and soft acids and bases. *J. Am. Chem. Soc.* **1963**, *85*, 3533-3539.

103. Palacios, O.; Atrian, S.; Capdevila, M. Zn- and Cu-thioneins: A functional classification for metallothioneins? *J. Biol. Inorg. Chem.* **2011**, *16*, 991-1009.

104. Rulisek, L.; Vondrasek, J. Coordination geometries of selected transition metal ions (Co^{2+}, Ni^{2+}, Cu^{2+}, Zn^{2+}, Cd^{2+}, and Hg^{2+}) in metalloproteins. *J. Inorg. Biochem.* **1998**, *71*, 115-127.

105. Messerle, B. A.; Schaffer, A.; Vasak, M.; Kagi, J. H.; Wuthrich, K. Comparison of the solution conformations of human [Zn_7]-metallothionein-2 and [Cd_7]-metallothionein-2 using nuclear magnetic resonance spectroscopy. *J. Mol. Biol.* **1992**, *225*, 433-443.

106. Lobinski, R.; Chassaigne, H.; Szpunar, J. Analysis for metallothioneins using coupled techniques. *Talanta* **1998**, *46*, 271-289.

107. Gehrig, P. M.; You, C.; Dallinger, R.; Gruber, C.; Brouwer, M.; Kagi, J. H.; Hunziker, P. E. Electrospray ionization mass spectrometry of zinc, cadmium, and

copper metallothioneins: Evidence for metal-binding cooperativity. *Protein Sci.* **2000**, *9*, 395-402.

108. Boys, B. L.; Kuprowski, M. C.; Noel, J. J.; Konermann, L. Protein oxidative modifications during electrospray ionization: Solution phase electrochemistry or corona discharge-induced radical attack? *Anal. Chem.* **2009**, *81*, 4027-4034.

109. Chen, M.; Cook, K. D. Oxidation artifacts in the electrospray mass spectrometry of Abeta Peptide. *Anal. Chem.* **2007**, *79*, 2031-2036.

110. Zinnel, N. F.; Pai, P.-J.; Russell, D. H. Ion mobility-mass spectrometry (IM-MS) for top-down proteomics: Increased dynamic range affords increased sequence coverage. *Anal. Chem.* **2012**, *84*, 3390-3397.

111. Roepstorff, P.; Fohlman, J. Letter to the editors. *Biol. Mass Spectrom.* **1984**, *11*, 601-601.

112. Biemann, K. Appendix 5. Nomenclature for peptide fragment ions (positive ions). In *Methods in Enzymology*; McCloskey, J. A., Ed.; Academic Press: San Diego, 1990; Vol. 193, pp 886-887.

113. Valentine, S. J.; Counterman, A. E.; Hoaglund, C. S.; Reilly, J. P.; Clemmer, D. E. Gas-phase separations of protease digests. *J. Am. Soc. Mass Spectrom.* **1998**, *9*, 1213-1216.

114. De Vriendt, K.; Van Driessche, G.; Devreese, B.; Bebrone, C.; Anne, C.; Frere, J. M.; Galleni, M.; Van Beeumen, J. Monitoring the zinc affinity of the metallo-beta-lactamase CphA by automated nanoESI-MS. *J. Am. Soc. Mass. Spectrom.* **2006**, *17*, 180-188.

115. Sun, J.; Kitova, E. N.; Wang, W.; Klassen, J. S. Method for distinguishing specific from nonspecific protein-ligand complexes in nanoelectrospray ionization mass spectrometry. *Anal. Chem.* **2006**, *78*, 3010-3018.

116. Pan, J.; Xu, K.; Yang, X.; Choy, W. Y.; Konermann, L. Solution-phase chelators for suppressing nonspecific protein-metal interactions in electrospray mass spectrometry. *Anal. Chem.* **2009**, *81*, 5008-5015.

117. Muñoz, A.; Rodriguez, A. R. Electrochemical behavior of metallothioneins and related molecules. Part II: Lys–Cys–Thr–Cys–Cys–Ala thionein fragment [56–61] MT I in the presence of cadmium and/or zinc. *Electroanalysis* **1995**, *7*, 670-673.

118. Erk, M.; Raspor, B. Evaluation of cadmium–metallothionein stability constants based on voltammetric measurements. *Anal. Chim. Acta* **1998**, *360*, 189-194.

119. Perez-Rafael, S.; Atrian, S.; Capdevila, M.; Palacios, O. Differential ESI-MS behaviour of highly similar metallothioneins. *Talanta* **2011**, *83*, 1057-1061.

120. Sutherland, D. E.; Stillman, M. J. Noncooperative cadmium(II) binding to human metallothionein 1a. *Biochem. Biophys. Res. Commun.* **2008**, *372*, 840-844.

121. Sutherland, D. E.; Summers, K. L.; Stillman, M. J. Noncooperative metalation of metallothionein 1a and its isolated domains with zinc. *Biochemistry* **2012**, *51*, 6690-7000.

122. Palumaa, P.; Eriste, E.; Njunkova, O.; Pokras, L.; Jornvall, H.; Sillard, R. Brain-specific metallothionein-3 has higher metal-binding capacity than ubiquitous

metallothioneins and binds metals noncooperatively. *Biochemistry* **2002**, *41*, 6158-6163.

123. Apuy, J. L.; Busenlehner, L. S.; Russell, D. H.; Giedroc, D. P. Ratiometric pulsed alkylation mass spectrometry as a probe of thiolate reactivity in different metalloderivatives of Staphylococcus aureus pI258 CadC. *Biochemistry* **2004**, *43*, 3824-3834.

124. Apuy, J. L.; Chen, X.; Russell, D. H.; Baldwin, T. O.; Giedroc, D. P. Ratiometric pulsed alkylation/mass spectrometry of the cysteine pairs in individual zinc fingers of MRE-binding transcription factor-1 (MTF-1) as a probe of zinc chelate stability. *Biochemistry* **2001**, *40*, 15164-15175.

125. Krezel, A.; Maret, W. Different redox states of metallothionein/thionein in biological tissue. *Biochem. J.* **2007**, *402*, 551-558.

126. Nielson, K. B.; Winge, D. R. Order of metal binding in metallothionein. *J. Biol. Chem.* **1983**, *258*, 13063-13069.

127. Chen, S.-H.; Russell, W. K.; Russell, D. H. Combining chemical labeling, bottom-up and top-down ion-mobility mass spectrometry to identify metal-binding sites of partially metalated metallothionein. *Anal. Chem.* **2013**, *85*, 3229-3237.

128. Ruotolo, B. T.; Benesch, J. L.; Sandercock, A. M.; Hyung, S. J.; Robinson, C. V. Ion mobility-mass spectrometry analysis of large protein complexes. *Nat. Protoc.* **2008**, *3*, 1139-1152.

129. Case, D. A.; Darden, T. A.; Cheatham III, T. E.; Simmerling, C. L.; Wang, J.; Duke, R. E.; Luo, R.; Merz, K. M.; Pearlman, D. A.; Crowley, M.; Walker, R. C.; Zhang, W.; Wang, B.; Hayik, S.; Roitberg, A.; Seabra, G.; Wong, K. F.; Paesani, F.; Wu, X.; Brozell, S.; Tsui, V.; Gohlke, H.; Yang, L.; Tan, C.; Mongan, J.; Hornak, V.; Cui, G.; Beroza, P.; Mathews, D. H.; Schafmeister, C.; Ross, W. S.; Kollman, P. A. *AMBER 9*, University of California, San Francisco: San Francisco, 2006.

130. Dupradeau, F.-Y.; Pigache, A.; Zaffran, T.; Savineau, C.; Lelong, R.; Grivel, N.; Lelong, D.; Rosanski, W.; Cieplak, P. The R.E.D. tools: Advances in RESP and ESP charge derivation and force field library building. *Phys. Chem. Chem. Phys.* **2010**, *12*, 7821-7839.

131. Mesleh, M. F.; Hunter, J. M.; Shvartsburg, A. A.; Schatz, G. C.; Jarrold, M. F. Structural information from ion mobility measurements: Effects of the long-range potential. *J. Phys. Chem.* **1996**, *100*, 16082-16086.

132. Lemkuil, D. C.; Nettesheim, D.; Shaw, C. F., 3rd; Petering, D. H. Reaction of Cd7-metallothionein with cis-dichlorodiammine platinum (II). *J. Biol. Chem.* **1994**, *269*, 24792-24797.

133. Bernhard, W. R.; Vasak, M.; Kagi, J. H. R. Cadmium binding and metal cluster formation in metallothionein: A differential modification study. In *Metallothionein II* Bernhard, W. R., Ed.; Birkhauser, Basel: 1987; Vol. 52 Experientia Supplementum, pp 243-246.

134. Meloni, G.; Zovo, K.; Kazantseva, J.; Palumaa, P.; Vasak, M. Organization and assembly of metal-thiolate clusters in epithelium-specific metallothionein-4. *J. Biol. Chem.* **2006**, *281*, 14588-14595.

135. Yu, W. H.; Cai, B.; Gao, Y.; Xie, Y.; Huang, Z. X. Expression, characterization, and reaction of recombinant monkey metallothionein-1 and its C33M mutant. *J. Protein Chem.* **2002**, *21*, 177-185.

136. Waldron, K. J.; Rutherford, J. C.; Ford, D.; Robinson, N. J. Metalloproteins and metal sensing. *Nature* **2009**, *460*, 823-830.

137. Leal, S. S.; Botelho, H. M.; Gomes, C. M. Metal ions as modulators of protein conformation and misfolding in neurodegeneration. *Coord. Chem. Rev.* **2012**, *256*, 2253-2270.

138. Zou, J.; Kajita, K.; Sugimoto, N. Cu^{2+} inhibits the aggregation of amyloid beta-peptide(1-42) *in vitro Angew. Chem. Int. Ed. Engl.* **2001**, *40*, 2274-2277.

139. Yoshiike, Y.; Tanemura, K.; Murayama, O.; Akagi, T.; Murayama, M.; Sato, S.; Sun, X.; Tanaka, N.; Takashima, A. New insights on how metals disrupt amyloid beta-aggregation and their effects on amyloid-beta cytotoxicity. *J. Biol. Chem.* **2001**, *276*, 32293-32299.

140. Uversky, V. N.; Li, J.; Fink, A. L. Metal-triggered structural transformations, aggregation, and fibrillation of human alpha-synuclein: A possible molecular NK between Parkinson's disease and heavy metal exposure. *J. Biol. Chem.* **2001**, *276*, 44284-44296.

141. Bocharova, O. V.; Breydo, L.; Salnikov, V. V.; Baskakov, I. V. Copper(II) inhibits *in vitro* conversion of prion protein into amyloid fibrils. *Biochemistry* **2005**, *44*, 6776-6787.

142. Golts, N.; Snyder, H.; Frasier, M.; Theisler, C.; Choi, P.; Wolozin, B. Magnesium inhibits spontaneous and iron-induced aggregation of alpha-synuclein. *J. Biol. Chem.* **2002**, *277*, 16116-16123.

143. Cuajungco, M. P.; Goldstein, L. E.; Nunomura, A.; Smith, M. A.; Lim, J. T.; Atwood, C. S.; Huang, X.; Farrag, Y. W.; Perry, G.; Bush, A. I. Evidence that the beta-amyloid plaques of Alzheimer's disease represent the redox-silencing and entombment of abeta by zinc. *J. Biol. Chem.* **2000**, *275*, 19439-19442.

144. Blindauer, C. A. Lessons on the critical interplay between zinc binding and protein structure and dynamics. *J. Inorg. Biochem.* **2013**, *121*, 145-155.

145. Gong, Y. H.; Elliott, J. L. Metallothionein expression is altered in a transgenic murine model of familial amyotrophic lateral sclerosis. *Exp. Neurol.* **2000**, *162*, 27-36.

146. Namdarghanbari, M. A.; Bertling, J.; Krezoski, S.; Petering, D. H. Toxic metal proteomics: Reaction of the mammalian zinc proteome with Cd^{2+}. *J. Inorg. Biochem.* **2014**, In press.

147. Braun, W.; Vasak, M.; Robbins, A. H.; Stout, C. D.; Wagner, G.; Kagi, J. H.; Wuthrich, K. Comparison of the NMR solution structure and the x-ray crystal structure of rat metallothionein-2. *Proc. Natl. Acad. Sci. USA* **1992**, *89*, 10124-10128.

148. Pearce, L. L.; Gandley, R. E.; Han, W.; Wasserloos, K.; Stitt, M.; Kanai, A. J.; McLaughlin, M. K.; Pitt, B. R.; Levitan, E. S. Role of metallothionein in nitric oxide signaling as revealed by a green fluorescent fusion protein. *Proc. Natl. Acad. Sci. USA* **2000**, *97*, 477-482.

149. Hong, S. H.; Maret, W. A fluorescence resonance energy transfer sensor for the beta-domain of metallothionein. *Proc. Natl. Acad. Sci. USA* **2003**, *100*, 2255-2260.

150. Hong, S. H.; Hao, Q.; Maret, W. Domain-specific fluorescence resonance energy transfer (FRET) sensors of metallothionein/thionein. *Protein Eng. Des. Sel.* **2005**, *18*, 255-263.

151. Liu, Y. L.; Lee, H. T.; Chang, C. C.; Kan, L. S. Reversible folding of cysteine-rich metallothionein by an overcritical reaction path. *Biochem. Biophys. Res. Commun.* **2003**, *306*, 59-63.

152. Breuker, K.; McLafferty, F. W. Stepwise evolution of protein native structure with electrospray into the gas phase, 10^{-12} to 10^{2} s. *Proc. Natl. Acad. Sci. USA* **2008**, *105*, 18145-18152.

153. Vahidi, S.; Stocks, B. B.; Konermann, L. Partially disordered proteins studied by ion mobility-mass spectrometry: Implications for the preservation of solution phase structure in the gas phase. *Anal. Chem.* **2013**, *85*, 10471-10478.

154. Guo, Y.; Ling, Y.; Thomson, B. A.; Siu, K. W. Combined ion-mobility and mass-spectrometry investigations of metallothionein complexes using a tandem

mass spectrometer with a segmented second quadrupole. *J. Am. Soc. Mass Spectrom.* **2005**, *16*, 1787-1794.

155. Morsa, D.; Gabelica, V.; De Pauw, E. Effective temperature of ions in traveling wave ion mobility spectrometry. *Anal. Chem.* **2011**, *83*, 5775-5782.

156. Rand, K. D.; Pringle, S. D.; Morris, M.; Engen, J. R.; Brown, J. M. ETD in a traveling wave ion guide at tuned Z-spray ion source conditions allows for site-specific hydrogen/deuterium exchange measurements. *J. Am. Soc. Mass Spectrom.* **2011**, *22*, 1784-1793.

157. Arcella, A.; Portella, G.; Ruiz, M. L.; Eritja, R.; Vilaseca, M.; Gabelica, V.; Orozco, M. Structure of triplex DNA in the gas phase. *J. Am. Chem. Soc.* **2012**, *134*, 6596-6606.

158. Ni, F. Y.; Cai, B.; Ding, Z. C.; Zheng, F.; Zhang, M. J.; Wu, H. M.; Sun, H. Z.; Huang, Z. X. Structural prediction of the beta-domain of metallothionein-3 by molecular dynamics simulation. *Proteins* **2007**, *68*, 255-266.

159. Onufriev, A.; Bashford, D.; Case, D. A. Exploring protein native states and large-scale conformational changes with a modified generalized born model. *Proteins* **2004**, *55*, 383-394.

160. Baumketner, A.; Bernstein, S. L.; Wyttenbach, T.; Bitan, G.; Teplow, D. B.; Bowers, M. T.; Shea, J. E. Amyloid beta-protein monomer structure: A computational and experimental study. *Protein Sci.* **2006**, *15*, 420-408.

161. Feig, M.; Karanicolas, J.; Brooks, C. L., 3rd MMTSB Tool Set: Enhanced sampling and multiscale modeling methods for applications in structural biology. *J. Mol. Graph. Model.* **2004**, *22*, 377-395.

162. Kaltashov, I. A.; Mohimen, A. Estimates of protein surface areas in solution by electrospray ionization mass spectrometry. *Anal. Chem.* **2005**, *77*, 5370-5379.

163. Testa, L.; Brocca, S.; Grandori, R. Charge-surface correlation in electrospray ionization of folded and unfolded proteins. *Anal. Chem.* **2011**, *83*, 6459-6463.

164. Silveira, J. A.; Fort, K. L.; Kim, D.; Servage, K. A.; Pierson, N. A.; Clemmer, D. E.; Russell, D. H. From solution to the gas phase: Stepwise dehydration and kinetic trapping of substance P reveals the origin of peptide conformations. *J. Am. Chem. Soc.* **2013**, *135*, 19147-19153.

165. Skinner, O. S.; McLafferty, F. W.; Breuker, K. How ubiquitin unfolds after transfer into the gas phase. *J. Am. Soc. Mass Spectrom.* **2012**, *23*, 1011-1014.

166. Bush, M. F.; Hall, Z.; Giles, K.; Hoyes, J.; Robinson, C. V.; Ruotolo, B. T. Collision cross sections of proteins and their complexes: A calibration framework and database for gas-phase structural biology. *Anal. Chem.* **2010**, *82*, 9557-9565.

167. Campuzano, I.; Bush, M. F.; Robinson, C. V.; Beaumont, C.; Richardson, K.; Kim, H.; Kim, H. I. Structural characterization of drug-like compounds by ion mobility mass spectrometry: Comparison of theoretical and experimentally derived nitrogen collision cross sections. *Anal. Chem.* **2012**, *84*, 1026-1033.

168. Hu, L.; Ryde, U. Comparison of methods to obtain force-field parameters for metal sites. *J. Chem. Theory Comput.* **2011**, *7*, 2452-2463.

169. Sakharov, D. V.; Lim, C. Force fields including charge transfer and local polarization effects: Application to proteins containing multi/heavy metal ions. *J. Comput. Chem.* **2009**, *30*, 191-202.

170. Ruotolo, B. T.; Giles, K.; Campuzano, I.; Sandercock, A. M.; Bateman, R. H.; Robinson, C. V. Evidence for macromolecular protein rings in the absence of bulk water. *Science* **2005**, *310*, 1658-1661.

171. Chen, L.; Gao, Y. Q.; Russell, D. H. How alkali metal ion binding alters the conformation preferences of gramicidin A: A molecular dynamics and ion mobility study. *J. Phys. Chem. A* **2012**, *116*, 689-696.

172. Grabenauer, M.; Wyttenbach, T.; Sanghera, N.; Slade, S. E.; Pinheiro, T. J.; Scrivens, J. H.; Bowers, M. T. Conformational stability of Syrian hamster prion protein PrP(90-231). *J. Am. Chem. Soc.* **2010**, *132*, 8816-8818.

173. Bertini, I.; Luchinat, C.; Messori, L.; Vasak, M. Proton NMR studies of the cobalt(II)-metallothionein system. *J. Am. Chem. Soc.* **1989**, *111*, 7296-7300.

174. Sutherland, D. E.; Summers, K. L.; Stillman, M. J. Modeling the Zn^{2+} and Cd^{2+} metalation mechanism in mammalian metallothionein 1a. *Biochem. Biophys. Res. Commun.* **2012**, *426*, 601-607.

175. Palumaa, P.; Tammiste, I.; Kruusel, K.; Kangur, L.; Jornvall, H.; Sillard, R. Metal binding of metallothionein-3 versus metallothionein-2: Lower affinity and higher plasticity. *Biochim. Biophys. Acta* **2005**, *1747*, 205-211.

176. Rigby Duncan, K. E.; Stillman, M. J. Metal-dependent protein folding: Metallation of metallothionein. *J. Inorg. Biochem.* **2006**, *100*, 2101-2107.

177. Rigby, K. E.; Chan, J.; Mackie, J.; Stillman, M. J. Molecular dynamics study on the folding and metallation of the individual domains of metallothionein. *Proteins* **2006**, *62*, 159-172.

178. Chiti, F.; Dobson, C. M. Protein misfolding, functional amyloid, and human disease. *Annu. Rev. Biochem.* **2006**, *75*, 333-366.

179. Wright, P. E.; Dyson, H. J. Intrinsically unstructured proteins: Re-assessing the protein structure-function paradigm. *J. Mol. Biol.* **1999**, *293*, 321-331.

180. Dunker, A. K.; Lawson, J. D.; Brown, C. J.; Williams, R. M.; Romero, P.; Oh, J. S.; Oldfield, C. J.; Campen, A. M.; Ratliff, C. M.; Hipps, K. W.; Ausio, J.; Nissen, M. S.; Reeves, R.; Kang, C.; Kissinger, C. R.; Bailey, R. W.; Griswold, M. D.; Chiu, W.; Garner, E. C.; Obradovic, Z. Intrinsically disordered protein. *J. Mol. Graph. Model.* **2001**, *19*, 26-59.

181. Chouard, T. Structural biology: Breaking the protein rules. *Nature* **2011**, *471*, 151-153.

182. Uversky, V. N.; Dave, V.; Iakoucheva, L. M.; Malaney, P.; Metallo, S. J.; Pathak, R. R.; Joerger, A. C. Pathological unfoldomics of uncontrolled chaos: Intrinsically disordered proteins and human diseases. *Chem. Rev.* **2014**, *114*, 6844-6879.

183. Uversky, V. N.; Oldfield, C. J.; Dunker, A. K. Intrinsically disordered proteins in human diseases: Introducing the D2 concept. *Annu. Rev. Biophys.* **2008**, *37*, 215-246.

184. Iakoucheva, L. M.; Brown, C. J.; Lawson, J. D.; Obradovic, Z.; Dunker, A. K. Intrinsic disorder in cell-signaling and cancer-associated proteins. *J. Mol. Biol.* **2002**, *323*, 573-584.

185. Dyson, H. J.; Wright, P. E. Intrinsically unstructured proteins and their functions. *Nat. Rev. Mol. Cell Biol.* **2005**, *6*, 197-208.

186. Dyson, H. J.; Wright, P. E. Elucidation of the protein folding landscape by NMR. *Methods Enzymol.* **2005**, *394*, 299-321.

187. Kwan, A. H.; Mobli, M.; Gooley, P. R.; King, G. F.; Mackay, J. P. Macromolecular NMR spectroscopy for the non-spectroscopist. *FEBS J.* **2011**, *278*, 687-703.

188. Konermann, L.; Pan, J.; Liu, Y. H. Hydrogen exchange mass spectrometry for studying protein structure and dynamics. *Chem. Soc. Rev.* **2011**, *40*, 1224-1234.

189. Gau, B. C.; Sharp, J. S.; Rempel, D. L.; Gross, M. L. Fast photochemical oxidation of protein footprints faster than protein unfolding. *Anal. Chem.* **2009**, *81*, 6563-6571.

190. Hernandez, H.; Robinson, C. V. Determining the stoichiometry and interactions of macromolecular assemblies from mass spectrometry. *Nat. Protoc.* **2007**, *2*, 715-726.

191. Uetrecht, C.; Rose, R. J.; van Duijn, E.; Lorenzen, K.; Heck, A. J. Ion mobility mass spectrometry of proteins and protein assemblies. *Chem. Soc. Rev.* **2010**, *39*, 1633-1655.

192. Lee, S.-W.; Freivogel, P.; Schindler, T.; Beauchamp, J. L. Freeze-dried biomolecules: FT-ICR studies of the specific solvation of functional groups and clathrate formation observed by the slow evaporation of water from hydrated peptides and model compounds in the gas phase. *J. Am. Chem. Soc.* **1998**, *120*, 11758-11765.

193. Kony, D. B.; Hunenberger, P. H.; van Gunsteren, W. F. Molecular dynamics simulations of the native and partially folded states of ubiquitin: Influence of methanol cosolvent, pH, and temperature on the protein structure and dynamics. *Protein Sci.* **2007**, *16*, 1101-1118.

194. Koeniger, S. L.; Clemmer, D. E. Resolution and structural transitions of elongated states of ubiquitin. *J. Am. Soc. Mass Spectrom.* **2007**, *18*, 322-331.

195. Shi, H.; Atlasevich, N.; Merenbloom, S. I.; Clemmer, D. E. Solution dependence of the collisional activation of ubiquitin $[M + 7H]^{7+}$ ions. *J. Am. Soc. Mass Spectrom.* **2014**, *25*, 2000-2008.

196. Wyttenbach, T.; Bowers, M. T. Structural stability from solution to the gas phase: Native solution structure of ubiquitin survives analysis in a solvent-free ion mobility-mass spectrometry environment. *J. Phys. Chem. B* **2011**, *115*, 12266-12275.

197. Pringle, S. D.; Giles, K.; Wildgoose, J. L.; Williams, J. P.; Slade, S. E.; Thalassinos, K.; Bateman, R. H.; Bowers, M. T.; Scrivens, J. H. An investigation of the mobility separation of some peptide and protein ions using a new hybrid quadrupole/travelling wave IMS/oa-ToF instrument. *Int. J. Mass Spectrom.* **2007**, *261*, 1-12.

198. Susa, A. C.; Mortensen, D. N.; Williams, E. R. Effects of cations on protein and peptide charging in electrospray ionization from aqueous solutions. *J. Am. Soc. Mass Spectrom.* **2014**, *25*, 918-927.

199. Shi, H.; Clemmer, D. E. Evidence for two new solution states of ubiquitin by IMS-MS analysis. *J. Phys. Chem. B* **2014**, *118*, 3498-3506.

200. Hyung, S. J.; Robinson, C. V.; Ruotolo, B. T. Gas-phase unfolding and disassembly reveals stability differences in ligand-bound multiprotein complexes. *Chem. Biol.* **2009**, *16*, 382-390.

201. Schennach, M.; Breuker, K. Proteins with highly similar native folds can show vastly dissimilar folding behavior when desolvated. *Angew. Chem. Int. Ed. Engl.* **2014**, *53*, 164-168.

202. Gabelica, V.; De Pauw, E. Internal energy and fragmentation of ions produced in electrospray sources. *Mass Spectrom. Rev.* **2005**, *24*, 566-587.

203. Morsa, D.; Gabelica, V.; De Pauw, E. Fragmentation and isomerization due to field heating in traveling wave ion mobility spectrometry. *J. Am. Soc. Mass Spectrom.* **2014**, *25*, 1384-1393.

204. Merenbloom, S. I.; Flick, T. G.; Williams, E. R. How hot are your ions in TWAVE ion mobility spectrometry? *J. Am. Soc. Mass Spectrom.* **2012**, *23*, 553-562.

205. Wells, J. M.; McLuckey, S. A. Collision-induced dissociation (CID) of peptides and proteins. *Methods Enzymol.* **2005**, *402*, 148-185.

206. Myung, S.; Badman, E. R.; Lee, Y. J.; Clemmer, D. E. Structural transitions of electrosprayed ubiquitin ions stored in an ion trap over ~10 ms to 30 s. *J. Phys. Chem. A* **2002**, *106*, 9976-9982.

207. Badman, E. R.; Myung, S.; Clemmer, D. E. Evidence for unfolding and refolding of gas-phase cytochrome C ions in a Paul trap. *J. Am. Soc. Mass Spectrom.* **2005**, *16*, 1493-1497.

208. Breuker, K.; Oh, H.; Horn, D. M.; Cerda, B. A.; McLafferty, F. W. Detailed unfolding and folding of gaseous ubiquitin ions characterized by electron capture dissociation. *J. Am. Chem. Soc.* **2002**, *124*, 6407-6420.

209. Hall, Z.; Politis, A.; Bush, M. F.; Smith, L. J.; Robinson, C. V. Charge-state dependent compaction and dissociation of protein complexes: Insights from ion mobility and molecular dynamics. *J. Am. Chem. Soc.* **2012**, *134*, 3429-3438.

210. Segev, E.; Wyttenbach, T.; Bowers, M. T.; Gerber, R. B. Conformational evolution of ubiquitin ions in electrospray mass spectrometry: Molecular dynamics simulations at gradually increasing temperatures. *Phys. Chem. Chem. Phys.* **2008**, *10*, 3077-3082.

211. Price, W. D.; Schnier, P. D.; Williams, E. R. Tandem mass spectrometry of large biomolecule ions by blackbody infrared radiative dissociation. *Anal. Chem.* **1996**, *68*, 859-866.

APPENDIX

DETAILED PROCEDURES FOR MD SIMULATIONS

All-atom MD simulations were performed using Amber 9.0 FF99SB force field, which is extended to include parameters for Cd^{2+} ions (See **Table 4.1**). The initial structure of Cd_7MT was constructed by connecting $Cd_4\alpha$ and $Cd_3\beta$ domains (PDB: 1MHU and 2MHU) using a trans configuration (backbone dihedral angle $\omega \sim 180°$) between the two connecting lysines (Lys30-Lys31). In case of ubiquitin, solution NMR structure (1D3Z) was used as starting structure. Initial structures of partially-metalated and metal-free MTs were obtained by removal of Cd^{2+} and the corresponding Cd^{2+}-S connectivities (See **Figure 4.2**). We note that there may be other possible Cd^{2+} configurations in the partially metallated forms. For example, Cd^{2+} may bind cysteines that are different from those designated in **Figure 4.2** and the coordination number may not equal to four. Nevertheless, the first attempt for our simulations is limited to the known Cd^{2+}-S bonding configurations in human Cd_7MT. Initial structures of ubiquitin and Cd_iMTs ($i = 0 - 7$) were minimized 5000 steps with infinite cutoff, followed by fifty- (or twenty five-) nanosecond production simulations *in vacuo* or implicit solvent at a constant temperature 300 K. The nonbound interaction for production MD simulations was set as 12 Å. For every 5 ps, the simulated structures were saved into trajectory coordinates for CCS calculation. For dehydration, the solution phase structures (every 5 ps) were treated as the initial structures for *in vacuo* energy minimization for 100000 steps.

Transition metal ions constitute a major problem in MD simulations because force field parameters for these ions are generally not available. The specific challenges for modeling transition metal ions are: (1) the interaction between metal ion and ligand(s) is intermediate between that of non-covalent and covalent bonds; (2) the metal ion can have many different types of ligands and number of coordination bonds; and (3) quantum mechanical ligand-field, spin-state, Jahn-Teller distortion, and trans effect also need to be addressed. For these reasons, the development of force field parameters for transition metal ions has been relatively limited, making MD simulations of metalloproteins greatly difficult. On the other hand, methods for modeling of metalloproteins are also underdeveloped. Current approaches usually involve (1) defining a covalent bond and a set of interactions between metal ion and ligand atom(s) (bonded method) or (2) using nonbonded electrostatic and van der Waals forces (nonbonded method), with either formal or partial charge of metal ions and ligands.

In our study, four candidate cadmium parameters obtained from previous studies were evaluated (**Table 4.1**). These four Cd^{2+} parameters were examined using MD simulations of Cd_7MT in the implicit water model, and choosing the parameter that agrees best with experimental data (NMR-determined structure) for production simulations. Our emulation suggests that the B2 parameter (bonded method with formal charge of cadmium ion) yielded trajectories closest to the ones for the NMR-determined structure.

We next incorporated Cd^{2+} into trajectory method in MOBCAL using Cu^{2+} atomic energy and van der Waals distance for Cd^{2+} (atomic mass = 112.41 Da, atomic energy = 1.35 meV, van der Waals distance = 3.5 Å). Our data show that the range of CCS for the simulated structures is ~ 1150 – 1300 $Å^2$ with an average value 1205 ± 34 $Å^2$, however, this value is 163 $Å^2$ larger than that for the NMR-determined structure (1042 $Å^2$) (data not shown). The data suggest that our simulation parameters are biased and the CCS derived from MD simulation requires correction.

The reason(s) that the calculations overestimate the CCS (16 %) is not fully understood. The error may arise from several factors, including errors associated with the calibration for traveling-wave CCS, limitations of structure sampling for classical MD, intrinsic errors of MD simulations and trajectory method, capability of classical MD algorithms in treating interaction potentials of transition metal ions, and more likely, the cadmium parameters in force field and trajectory method since these parameters/methods for transition metals have not been thoroughly examined. We note that the simulation data for apoMT show good agreement to the experimental IM-MS data (see Chapter IV), suggesting that the errors are most likely associated with the parameters for Cd^{2+} ions. In case of MT, the error may be more pronounced because there are seven Cd^{2+} ions on such a small protein. However, developing new parameters for Cd^{2+} is beyond the scope of our study. Nevertheless, our first attempt to adjust the bias (16 %) is to scale CCS values of Cd_iMT by the number of Cd^{2+} and good agreement was found between the scaled CCSs and the experimental CCS:

$$CCS_{cal} = CCS_{MD}(1-\frac{\text{number of } Cd^{2+}}{7}\times 16\%)$$

In addition to simulation at 300K, we also simulated the effect of temperature on protein conformation (see Chapter V). To mimic the effect of temperature on protein conformation, the ubiquitin simulations were run over a linear temperature gradient using a rate of 20 K/ns. Two scenarios, ion heating in either the presence or absence of water, were considered to reflect a different stage in ESI droplet/ion evolution. In the case of the ion heating in the presence of water, subsequent dehydration was performed by *in vacuo* minimization for 10000 steps to generate dehydrated structures. The CCS for the simulated ubiquitin was calculated using projection approximation (PA) method as the trajectory method fails in calculating CCS values for many of the extended ubiquitin structures. However, the PA typically underestimate by 15%. We used an empirically determined scaling factor determined by Robison *et al*. to correct all CCS value obtained by PA method. The corrected CCSs show a great agreement to our experimental CCS data. In case of MTs, 5 ns-simulation was performed at a fixed temperature to evaluate the conformational evolution at various temperatures. The effect of temperature on Cd_iMTs (i = 0 – 7) was simulated from 300 to 2000 K with 50 K increments. For dehydration, the solution phase structures (every 10 ps) were treated as the initial structures for *in vacuo* energy minimization for 10000 steps. Trajectory method (TM) implanted in MOBCAL is used for CCS calculation for Cd_iMT.